博士論文

Application of Meta-Modeling to Bridge Structure for Consistent Seismic Response Analysis

(整合する地震応答解析を行うためのメタモデリングの橋梁構造への適用)

A DISSERTATION
SUBMITTED TO THE DEPARTMENT OF CIVIL ENGINEERING
OF THE GRADUATE SCHOOL OF ENGINEERING,
UNIVERSITY OF TOKYO
IN PARTIAL FULFILLMENT OF THE REQUIREMENTS
FOR THE DEGREE OF
DOCTOR OF PHILOSOPHY

Jayasinghe Arachchilage Supun Chamara Jayasinghe
(ジャヤシンヘ　アラチラゲ　スプン　チャマラ　ジャヤシンヘ)

September 2015

Acknowledgement

First of all, I would like to express my heartfelt gratitude to Professor Muneo Hori for being my advisor for this research. His enthusiastic guidance, constructive criticism and friendly discussions were really useful for the completion of this research work. My honest acknowledgments also go to Professor Lalith Wijerathne, Professor Tsuyoshi Ichimura, and Professor Seizo Tanaka for their guidance, teaching and help throughout my studies. I would also like to express my sincere gratitude to my doctorate committee members Professor Muneo Hori, Professor Lalith Wijerathne, Professor Tsuyoshi Ichimura, Professor Tomonori Nagayama and Professor Koichi Kusunoki, whose brilliant comments, suggestions and criticism provided guidance and challenges to this research.

Secondly, I would like to express my sincere gratitude to Professor Yozo Fujino for his continuous support during this research, by providing necessary information and data. Without his support, it would have been impossible to get the required data.

I acknowledge the Ministry of Education, Culture, Sports, Science and Technology of Japan (MEXT) for awarding me full financial support to study at the Earthquake Research Institute (ERI), the University of Tokyo.

I would like to thank my fellow lab members and friends whose support enabled me to keep my research moving forward. I extend my gratitude especially to Muhammad Rizwan Riaz, Leonel Aguilar, Ryoichiro Agata and Mahendra Kumar Pal.

Special thanks to my wife Manoja Abesinghe and my parents; their example, sacrifice and support allowed me to reach this point. My sincere gratitude is also extended to my brother Neranjan Jayasinghe for his support and encouragement throughout this research.

Abstract

For earthquake disaster estimation of an urban area, numerical simulation of the seismic response for various structures is an alternative of the current estimation that uses empirical relations of structural damage probability for an estimated ground motion index. We need to focus on developing a more rational damage estimation method and the use of numerical simulation is a candidate. Since a variety of numerical methods of the seismic response analysis is available, construction of a suitable analysis model is a bottleneck to realize an estimation method based on simulating the seismic response for various structures.

In view of quality and quantity of data which are available in a target urban area, this study is proposing a systematic methodology of automated model construction, based on a meta-modeling theory that produces a set of analysis models consistent with a continuum mechanics model or a solid element finite element model. This theory regards an analysis model as a genuinely mathematical approximation of a continuum mechanics model.

Using a bridge structure as an example, this study is aimed at developing the following three: 1) consistent data conversion from a solid element solution to a beam element solution or vice versa; 2) construction of a simple consistent analysis model which shares the fundamental dynamic properties with a continuum mechanics model; and 3) development of a module that automatically de-codes and interprets a set of digital data of a structure and constructs consistent models for it.

The consistent data conversion is done by converting displacement and stress functions of a target structure. The use of stress function is a key in order to make a beam element model (which does not need Poisson's ratio) consistent with a solid element model (which needs Poisson's ration). This conversion method contributes in promoting a solid element analysis since 1) cross sectional force or moment of a beam element model is more accurately computed for a given solid element solution, compared to an ordinary method which approximately computes surface integration of stress, and 2) a beam element solution could be used as a smart initial guess of a solid element solution for a conjugate gradient method (CG method) when it solves a large scale solid element model.

According to the meta-modeling theory, a simple consistent model, such as a single mass spring model or a multi-mass spring model, is constructed for a bridge structure. Indeed, a consistent mass spring model (CMSM) or a consistent lumped mass model (CLMM) shares the same natural frequency and mode with a continuum mechanics model; the CLMM is the simplest as it has single mass and spring, which the CMSM has more than one mass and spring. It is found that a CMSM of two masses need to have an extra spring which an ordinary mass spring model does not have, so that the first and second natural frequencies and modes of the CMSM coincide with those of the solid element model.

A prototype of an automated model construction module is developed. This prototype is able to use two sets of digital data (Auto CAD and GIS) of a bridge structure, and to generate a solid element model, a beam element model, a CMSM or a CLMM. The quality of these models of distinct fidelity is assured by comparing the fundamental properties and the synthesized response. Six different geometric types of simple bridge structures are used to check the performance of the module. The prototype is used to construct solid and beam element models for a part of freeway road network in Tokyo Metropolitan.

Table of Contents

List of Figures

List of Tables

Chapter 1

Introduction

1.1 Background

A methodology of a more reliable estimation of possible damage induced by an earthquake is to improve the accuracy of seismic response analysis using a model of higher fidelity; with the progress of computers, large scale computation that is needed for the analysis of a high fidelity model can be conducted [1, 2]. In civil engineering, however, the use of a structural element, such as a truss, beam, plate or shell, is standard [3, 4, 5, 6] and it is rare that solid element analysis is made even for a structure of complicated configuration [7, 8]. While there are several reasons for such a rare use of solid element analysis, a major reason is that it is believed the structural element analysis which is tuned with experimental results could produce a more accurate solution than the solid element analysis.

On the other hand, it is a common practice to develop a set of different fidelity models at the beginning of an analysis of a complex structure [9, 10]. If a numerical model of desired fidelity could be constructed, we can choose a suitable analysis method for it. A model of higher fidelity is able to make a more accurate analysis of complicated response. However, it is not an easy task to construct a higher fidelity model for an actual structure using data and information of limited quality and quantity.

In this study, we mainly force the following two issues related to the above mentioned facts: 1) the promotion of solid element analysis in civil engineering and 2) the development of consistent low fidelity models to assess the solid element analysis. A meta-modeling theory [11, 12, 13, 14, 15] is being proposed to fulfill these two points. The essence of this theory is that there are structural mechanics modelings which are consistent with continuum mechanics modeling. A structure element analysis that stems from consistent structure mechanics modeling is a mathematical approximation of a solid element analysis that corresponds to continuum mechanics modeling.

There holds a trade-off relation between the computational cost and the accuracy [12]. According to the meta-modeling, a solid element analysis that uses a model of high fidelity is an extreme case of high accuracy but high cost. A structure element analysis ends up with much less computational cost but with some loss of the accuracy. A key issue here is that the same physical problem is solved; due to difference in mathematical approximation, the physical problem is converted to different mathematical problems. The meta-model theory clarifies this point, and it is the choice of a user whether he employs a solid or structure element analysis considering the trade-off relation between the computational cost and the accuracy for solving the same physical problem.

There is another difficulty in large scale numerical simulation. That is the laboriousness of modeling, when the number of structures and structure components analyzed is huge. The development of automated model construction, i.e., conversion of digital data available for a target structure to an analysis model which is directly input to a suitable seismic response analysis method, is thus required. In this study, the meta-modeling

theory is employed with automated modeling concept as a solution of automated model construction.

1.2 Objective

The objective of this study is to establish consistent seismic response analysis based on the meta-modeling theory. The target structure is bridge structure. The scope of this study is summarized as follows:

- Develop the necessary tools for consistent dynamic analysis of a structure based on the meta-modeling theory,
- Utilize the developed tools for a bridge structure and identify the advantages and disadvantages of the tools,
- Develop modules for an automated model construction for large scale bridge structure, and
- Investigate further possible improvement of the developed tools.

1.3 Thesis structure

The contents of this dissertation are as follows. First, the meta-modeling theory is explained in Chapter 2. According to the meta-modeling theory, new tools for consistent dynamic analysis of structure are developed in Chapter 3. Then, numerical experiments of applying the proposed tools to example problems are carried out in Chapter 4. Recommended possible improvements for developed tools are discussed in Chapter 5. Concluding remarks are made in Chapter 6.

Chapter 2

Meta-Modeling Theory

2.1 Overview

The main hinge in promoting a solid element analysis in civil engineering is a less clear relation between structural mechanics [16] and (solid) continuum mechanics [17, 18, 19]. It is taken for granted that structural mechanics and continuum mechanics share many elements, but, in my eyes, the difference between them has not been clearly discussed. Recently, being proposed is a meta-modeling theory [11], which rigorously allocates structural mechanics as a mathematical approximation of continuum mechanics in the sense that structural mechanics solves a Lagrangian problem of continuum mechanics using suitable mathematical approximations.

In order to relate different fidelity models which are constructed for one structure, we take advantage of the meta-modeling theory [11]. As for mechanical response, the meta-modeling theory starts from continuum mechanics as the basic physics. By adding mathematical approximations, the meta-modeling theory derives another modeling such as beam theory or shell theory in a systematic manner. The key concept of the meta-modeling theory is that all the modelings solve the same physical problem of continuum mechanics but use different mathematical approximations; continuum mechanics modeling does not use any approximation.

The contents of this chapter are as follows. First, the meta-modeling theory is briefly explained in Subsection 2.2. Then, in Subsection 2.3, we present the meta-modeling theory for a beam problem, clarifying a beam model that is consistent with continuum mechanics. The meta-modeling theory for a plate problem is presented at the end.

2.2 Summary of meta-modeling theory

In the meta-modeling theory, modeling means to create a mathematical problem for a target physical problem. There are many ways to develop a distinct mathematical problem, depending on the accuracy that is expected in solving the physical problem. The meta-modeling theory delivers a set of consistent modelings which produce an approximate solution of the original modeling. As an example in structural problems, the meta-modeling theory uses continuum mechanics modeling as the basic modeling. Some of structure mechanics modelings are specified as consistent modeling of the continuum mechanics modeling. Then, those consistent structure mechanics modelings produce an approximate solution of the continuum mechanics modeling.

For simplicity, we assume a homogeneous elastic body (V) with an isotropic elasticity tensor and density, denoted by $\mathbf{c}$ and ρ. If velocity and strain are denoted by $\mathbf{v}$ and $\boldsymbol{\epsilon}$ respectively, the Lagrangian of V is

$$\mathcal{L}[\mathbf{v}, \boldsymbol{\epsilon}] = \int_V \frac{1}{2}\rho \mathbf{v}\cdot\mathbf{v} - \frac{1}{2}\boldsymbol{\epsilon}:\mathbf{c}:\boldsymbol{\epsilon}\, \mathrm{d}v, \tag{2.1}$$

where · and : are the inner product and second-order contraction, respectively. We compute $\mathbf{v} = \dot{\mathbf{u}}$ and $\boldsymbol{\epsilon} = sym\{\boldsymbol{\nabla}\mathbf{u}\}$, using a displacement function $\mathbf{u}$ which satisfies prescribed boundary and initial conditions; sym stands for the symmetric part of the second-order tensor, $\dot{(\,.\,)}$ and $\boldsymbol{\nabla}(\,.\,)$ being temporal and gradient of $(\,.\,)$.

Structure mechanics employs a one dimensional stress-strain relation [20] that is not validated in any experiment. That is, Young's modulus, E, is used rather than the fourth-order tensor $\mathbf{c}$ as a material property of V. As an example, in the Cartesian coordinate of (x_1, x_2, x_3), the normal stress and strain component in the x_1-direction are related as

$$\sigma_{11} = E\epsilon_{11},$$

rather than $\boldsymbol{\sigma} = \mathbf{c}\!:\boldsymbol{\epsilon}$ or

$$\sigma_{11} = c_{1111}\epsilon_{11} + \cdots = \frac{(1-\nu)E}{(1+\nu)(1-2\nu)}\epsilon_{11} + \cdots,$$

where $\boldsymbol{\sigma}$ is stress.

According to the meta-modeling theory [11], we do not have to assume the one-dimensional stress-strain relation, but we employ the following alternative Lagrangian:,

$$\mathcal{L}^*[\mathbf{v}, \boldsymbol{\epsilon}, \boldsymbol{\sigma}] = \int_V \frac{1}{2}\rho\mathbf{v}\cdot\mathbf{v} - \left(\boldsymbol{\sigma}\!:\boldsymbol{\epsilon} - \frac{1}{2}\boldsymbol{\sigma}\!:\mathbf{c}^{-1}\!:\boldsymbol{\sigma}\right) \mathrm{d}v, \tag{2.2}$$

where $\mathbf{c}^{-1}$ is the inverse tensor of $\mathbf{c}$; see Appendix A for index form of $\mathcal{L}^*$. Since the terms in the parenthesis in Eq. (2.2) equal $\frac{1}{2}\boldsymbol{\epsilon}\!:\mathbf{c}\!:\boldsymbol{\epsilon}$, for $\boldsymbol{\sigma}$ satisfying $\boldsymbol{\epsilon} = \mathbf{c}^{-1}\!:\boldsymbol{\sigma}$, this Lagrangian is equivalent to the ordinary one of Eq. (2.1). It is easy to show that, if non-zero components of $\boldsymbol{\epsilon}$ and $\boldsymbol{\sigma}$ are ϵ_{11} and σ_{11} only, the second term in the integrand of $\mathcal{L}^*$ becomes $\sigma_{11}\epsilon_{11} - \frac{1}{2}\sigma_{11}^2/E$, and the variation with respect to σ_{11} is

$$\delta\left(\sigma_{11}\epsilon_{11} - \frac{1}{2}\frac{\sigma_{11}^2}{E}\right) = \frac{\delta\sigma_{11}}{E}(E\epsilon_{11} - \sigma_{11}).$$

As is seen, the one-dimensional stress strain relation is derived from the mathematical operation of taking variation, without making any assumption such as the one-dimensional stress-strain relation.

The meta-modeling theory leads to consistent modeling which solves the variational problem of $\mathcal{L}^*$. If no approximation is made for $\mathbf{u}$ (that produces $\mathbf{v}$ and $\boldsymbol{\epsilon}$) and $\boldsymbol{\sigma}$, it results in continuum mechanics modeling, and the governing equation for $\mathbf{u}$ is the wave equation, i.e.,

$$\rho(\mathbf{x})\ddot{\mathbf{u}}(\mathbf{x}, t) - \boldsymbol{\nabla}\cdot\left(\mathbf{c}(\mathbf{x})\!:\boldsymbol{\nabla}\mathbf{u}(\mathbf{x}, t)\right) = 0. \tag{2.3}$$

If certain approximations are made for $\mathbf{u}$ and $\boldsymbol{\sigma}$, it results in a consistent modeling that solves a different mathematical problem. However, this problem is to solve the same physical problem (that is described in terms of the variational problem) using the mathematical approximations.

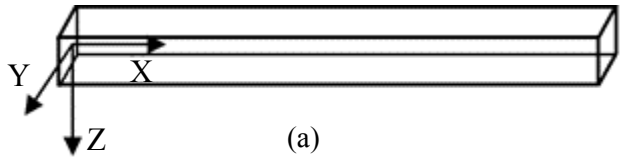

(a)

u	Deformation in x-direction (for beam)
w	Deflection in z-direction (for plate)
E, ρ	Young's modulus and density
A, I	Area and second moment of inertia (for plate)
H_0, H_2	Height and second moment (for plate)

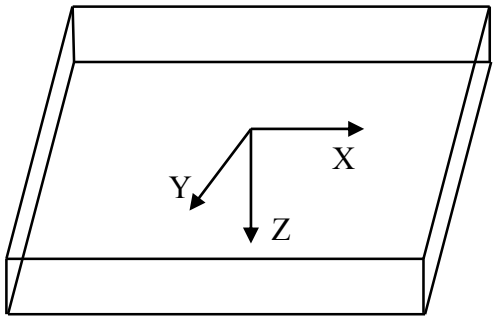

(b)

Figure 2.1: Schematic view of geometry with coordinate system: (a) beam; and (b) plate.

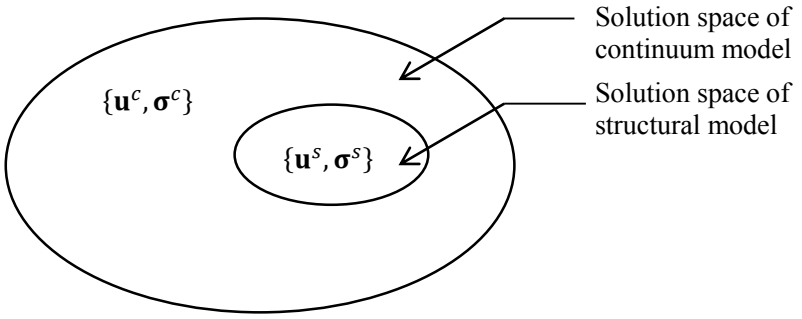

Figure 2.2: Solution space for structural and continuum model; solution space of structural model is subset of solution space of continuum model.

2.3 Meta-modeling for beam

According to the meta-modeling theory, a solution space of beam modeling is considered as a subset of a solution space of continuum mechanics of, $\{\mathbf{u}, \boldsymbol{\sigma}\}$; for the Lagrangian $\mathcal{L}^*$; see Fig. 2.2. For illustration, two functions, w and s, are used to determine non-zero components of $\mathbf{u}$ and $\boldsymbol{\sigma}$ as follows:

$$u_1 = -zw'(x,t), \qquad u_3 = w(x,t), \qquad \sigma_{11} = zs(x,t),$$

where, as shown in Fig. 2.1(a), the x_1- or x_3-axis is parallel or normal to the beam direction, respectively, and the bending moment produced by σ_{11} acts around the x_2-axis. Here, x and z are used instead of x_1 and x_3, and prime stands for derivative with respect to x. Note that w and s are function of x and t.

Substituting the approximated functions (in the beam modeling subset) into $\mathcal{L}^*$ and taking the variation of the resulting functional, we have

$$\delta\left(\int\int \frac{\rho A}{2}(\dot{w})^2 + \frac{\rho A}{2}(\dot{w}')^2 + Isw'' + \frac{I}{2E}s^2 \,\mathrm{d}x\mathrm{d}t\right) \tag{2.4}$$

$$= \int\int \frac{\partial}{\partial t}(\delta w' \rho I \dot{w}' + \delta w \rho A \dot{w}) + \frac{\partial}{\partial x}\left(\delta w' I s - \delta w(\rho I \ddot{w}' + I s')\right) + \delta w(\rho I \ddot{w}'' - \rho A \ddot{w} + I s'') + \delta s I \left(w'' + \frac{s}{E}\right) \mathrm{d}x\mathrm{d}t,$$

where $A = \int \mathrm{d}y\mathrm{d}z$ and $I = \int z^2 \, \mathrm{d}y\mathrm{d}z$, and dot stands for derivative with respect to t. Hence, $\delta \int \mathcal{L}^* \, \mathrm{d}t = 0$, leads to the governing equation of w, as

$$\rho A \ddot{w} - \rho I \ddot{w}'' + E I w'''' = 0, \tag{2.5}$$

with $s = -Ew''$; note that $s = -Ew''$is directly derived from $\delta \int \mathcal{L} \, \mathrm{d}t = 0$, and we do not have to make any assumption to relate w and s. The initial and boundary conditions are respectively obtained as follows:

$$\begin{cases} w \text{ given or } \dot{w} = 0, \\ w \text{ given or } \dot{w}' = 0, \end{cases} \tag{2.6}$$

$$\begin{cases} w \text{ given or } \rho I \ddot{w}' - E I w''' = 0, \\ w' \text{ given or } E I w'' = 0. \end{cases} \tag{2.7}$$

If we ignore minor differences, there are four representative beam modelings, namely, Bernoulli-Euler beam, Rayleigh beam, Shear beam and Timoshenko beam [21, 22, 23, 24, 25, 26, 27]. The difference in each beam modeling at dynamic state is identified easily from Table 2.1 [25]. The consistent beam modeling is actually Rayleigh beam [28]. Therefore, Rayleigh beam is consistent with continuum mechanics at dynamic state. Simultaneously, it is straightforward to show the consistency of Timoshenko beam modeling at dynamic state, as follows: Timoshenko beam model [22] uses the following non-zero components of $\mathbf{u}$ and $\boldsymbol{\sigma}$:

$$u_1 = -zw'(x,t), \qquad u_3 = w(x,t) + z\theta(x,t), \qquad \sigma_{11} = zs(x,t), \qquad \sigma_{31} = zr(x,t),$$

where θ is rotation around the y-axis and r is a function of x and t. Note that $z\theta$ is included in u_3; this term is regarded as the second term of the Taylor series expansion of u_3 with respect to z, while w is the first term of the expansion.

Substituting the above approximated functions into $\mathcal{L}^*$ and solving $\delta \int \mathcal{L}^* \, \mathrm{d}t = 0$, we obtain

$$\delta\left(\int\int \frac{\rho A}{2}(\dot{w})^2 + \frac{\rho I}{2}(\dot{w}')^2 + \dot{\theta}^2 + I(sw' + r\theta) + \frac{I}{2E}(w'')^2 + \frac{I}{2G}(\theta')^2 \, \mathrm{d}x\mathrm{d}t\right)$$

$$= \int\int \frac{\partial}{\partial t}\left(\delta w' \rho I \dot{w}' + \delta w \rho A \dot{w} + \delta\theta I \dot{\theta}\right) + \frac{\partial}{\partial x}(\delta w' I s - \delta w(\rho I \ddot{w}' + I s') + \delta\theta I r) + \delta w(\rho I \ddot{w}'' - \rho A \ddot{w} + I s'') + \delta s I \left(w'' + \frac{s}{E}\right) + \delta r I \left(\theta' + \frac{r}{2G}\right) \mathrm{d}x\mathrm{d}t = 0. \tag{2.8}$$

The governing equations of w and θ are derived as follows:

Table 2.1: Governing equations of four beam models.

Beam model	Governing equation
Bernoulli-Euler	$\rho A\ddot{w} + EIw'''' = 0$
Rayleigh	$\rho A\ddot{w} - \rho I\ddot{w}'' + EIw'''' = 0$
Shear	$\rho A\ddot{w} - \frac{\rho I}{kG}\ddot{w}'' + EIw'''' = 0$
Timoshenko	$\rho A\ddot{w} - \left(\rho I + \frac{\rho I}{kG}\right)\ddot{w}'' + \frac{\rho^2 I}{kG}\ddot{\ddot{w}} + EIw'''' = 0$

$$\rho A\ddot{w} - \rho I\ddot{w}'' + EIw'''' = 0,$$
$$\rho I\ddot{\theta} - 2GI\theta'' = 0.$$

where, G is shear modulus of the beam material.

This set of the differential equations of w and θ are similar to the governing equations of the Timoshenko beam model [25] It should be noted that no assumptions are made in deriving the governing equations of w and θ. Only a subset of the function space as described above is used in computing the Lagrangian.

A consistent model of a target continuum problem selects a subset of a function space of continuum mechanics, in order to obtain an approximate solution. The model is automatically validated in the framework of continuum mechanics. According to the meta-modeling theory, Rayleigh and Timoshenko beam modelings solve the same problem as the continuum model at dynamic state without employing Poisson's ration (ν), unlike continuum modeling; G is used for Timoshenko beam modeling. It was explained in the beginning of this section that an assumption of the one-dimensional stress–strain relation, made by the Rayleigh beam model does not match the tensorial relation of elasticity that is observed in experiments. According to the meta-modeling theory, we can explain that Rayleigh and Timoshenko beam modeling solve the same Lagrangian problem of continuum mechanics, using a special subset of the function space that happens to eliminate the contribution of ν in the governing equations. In other words, the comparison of a Rayleigh or Timoshenko beam element analysis with a solid element analysis is meaningful at dynamic state, and Bernoulli-Euler and shear beam modelings are consistent only at quasi-static state; see Table 2.1.

2.4 Meta-modeling for plate

Similar to a beam problem, we can allocate a suitable subset of the function space of continuum mechanics, $\{\mathbf{u}, \boldsymbol{\sigma}\}$, for $\mathcal{L}^*$, in order to obtain consistent plate governing equations; see list of related references [29, 30, 31, 32]. Here, we set non-zero components of $\mathbf{u}$ and $\boldsymbol{\sigma}$ as

$$u_1 = -zw_{,x}(x,y,t), \qquad u_2 = -zw_{,y}(x,y,t), \qquad u_3 = w(x,y,t),$$
$$\sigma_{11} = zs_{xx}(x,y,t), \qquad \sigma_{22} = zs_{yy}(x,y,t), \qquad \sigma_{12} = zs_{xy}(x,y,t),$$

where, as shown in Fig. 2.1(b), the x_1- or x_2-axis is on the plate plane, x_3-axis is normal to the surface of plate, and (x_1, x_2, x_3) is replaced by (x, y, z). We write an in-plane displacement component of plate using the gradient of w as

$$(u_1, u_2) = -z\boldsymbol{\nabla} w,$$

and in-plane stress components as

$$(\sigma_{11}, \sigma_{22}, \sigma_{12}) = z(s_{11}, s_{22}, s_{12}),$$

Using a two-dimensional second-order tensor $\mathbf{s}$. Here, w and $\mathbf{s}$ are function of x, y and t.

Substituting the approximated functions in the plate subset into $\mathcal{L}^*$and taking the variation of the resulting functional, we have

$$\delta\left(\int\int \frac{\rho H_2}{2}|\boldsymbol{\nabla}\dot{w}|^2 + \frac{\rho H_0}{2}\dot{w}^2 + H_2\left(\mathbf{s}\colon\boldsymbol{\nabla}\boldsymbol{\nabla}\mathrm{w} + \frac{1}{2}\mathbf{s}\colon\mathbf{c}^{-1}\colon\mathbf{c}\right)\mathrm{d}s\mathrm{d}t\right)$$

$$\begin{aligned}= \int\int \frac{\partial}{\partial t}(\boldsymbol{\nabla}\delta w\cdot\rho H_2\boldsymbol{\nabla}\dot{w} + \delta w\rho H_0\dot{w}) + \boldsymbol{\nabla}\cdot\left(\boldsymbol{\nabla}\delta w\cdot H_2\mathbf{s} - \delta w(\rho H_2\boldsymbol{\nabla}\ddot{w} + \boldsymbol{\nabla}\cdot\mathbf{s})\right)\\ + \delta w\left(\rho H_2\boldsymbol{\nabla}^2\ddot{w} - \rho H_0\ddot{w} + H_2\boldsymbol{\nabla}\cdot(\boldsymbol{\nabla}\cdot\mathbf{s})\right)\\ + \delta s\colon(\boldsymbol{\nabla}\boldsymbol{\nabla}\mathrm{w} + \mathbf{c}^{-1}\colon\mathbf{s})\,\mathrm{d}s\mathrm{d}t.\end{aligned} \tag{2.9}$$

Here, H_0 and H_2 are $\int \mathrm{d}z$ and $\int z^2\,\mathrm{d}z$. The same symbol $\mathbf{c}^{-1}$ is used for in-plane components of $\mathbf{s}$, and $\boldsymbol{\nabla}\boldsymbol{\nabla}\mathrm{w}$ and $\boldsymbol{\nabla}\cdot(\boldsymbol{\nabla}\cdot\mathbf{s})$ are a second-order tensor and a scalar, respectively.

We can derive the governing equations of w and $\mathbf{s}$ from vanishing of this variation. The expression of $\mathbf{s}$ is as follows;

$$\mathbf{c}^{-1}\colon\mathbf{s} = -\boldsymbol{\nabla}\boldsymbol{\nabla}\mathrm{w}, \tag{2.10}$$

meanwhile $\mathbf{c}^{-1}$ is for in-plane components and components of this tensor can be expressed as the following three-by-three matrix:

$$\frac{1}{E}\begin{bmatrix}1 & -v & 0\\ -v & 1 & 0\\ 0 & 0 & \dfrac{1+v}{2}\end{bmatrix}.$$

Here, $\mathbf{c}^{-1}$ is analogous to the elasticity tensor of two-dimensional state of plane stress. If we consider the inverse tensor of $\mathbf{c}^{-1}$, the components of inverse matrix are different from the corresponding components of the original $\mathbf{c}$. Just like a beam problem, we do not have to make an assumption of plane stress state, but it is automatically derived from $\mathcal{L}^*$ when suitable approximations are made for the functions.

The governing equation of consistent plate model can be obtained from expressions of w and $\mathbf{s}$ as

$$\rho H_0\ddot{w} - \rho H_2\boldsymbol{\nabla}^2\ddot{w} + \frac{H_2 E}{1-v^2}\boldsymbol{\nabla}^4 w = 0. \tag{2.11}$$

The initial and boundary conditions are respectively obtained as

$$\begin{cases} \boldsymbol{\nabla} w \text{ given or } \rho H_2 \boldsymbol{\nabla}^2 \dot{w} \ = 0, \\ w' \text{ given or } \rho H_0 \dot{w}' \ = 0, \end{cases} \tag{2.12}$$

$$\begin{cases} \mathbf{n}.\boldsymbol{\nabla} w \text{ given or } \boldsymbol{\nabla} \cdot (H_2 (\mathbf{c}^{-1})^{-\mathbf{1}} \mathbf{:} \boldsymbol{\nabla}\boldsymbol{\nabla} \mathrm{w}) \ = 0, \\ w \text{ given or } \mathbf{n}.\left(\rho H_2 \boldsymbol{\nabla} \ddot{w} - (\mathbf{c}^{-1})^{-\mathbf{1}} \boldsymbol{\nabla}^2 (\boldsymbol{\nabla} \cdot \mathbf{s})\right) . \end{cases} \tag{2.13}$$

The governing equations of the consistent plate model, Eq. (2.11), match with Kirchhoff-Love plate modeling [29, 30] that includes $-\rho H_2 \boldsymbol{\nabla}^2 \ddot{w}$ in addition to an ordinary plate model. According to the meta-modeling theory, Kirchhoff-Love plate modeling solves the same problem as the continuum modeling at dynamic state. Thus, the comparison of a Kirchhoff-Love plate element analysis with a solid element analysis is meaningful.

Chapter 3

Development of New Tools

3.1 Conversion between solid element solution and beam element solution based on meta-modeling

3.1.1 Overview

In civil engineering, it is believed that the structural element analysis which is tuned with experimental results can produce a more accurate solution than the solid element analysis. We have to accept that tuning a non-linear structural element with the experimental results is not a difficult task and the tuned structural element has high accuracy in predicting the structural responses. Nevertheless, the tuned structural element cannot guarantee high accuracy in computing responses which are not observed via experiment. This makes a clear contrast with the solid element analysis that computes structural responses at any point with more or less uniform accuracy. It is certainly true that measurement is made for key parts of a structure or a structural element. However, the uniform accuracy of the solid element analysis has been overlooked, unlike the fact that it only needs cheap and small material sample tests.

The complexity of the data conversion between solid element model and structural element model is another drawback, which prevents frequent usage of solid element model in actual civil engineering practices. An ordinary conversion method discussed in section 4.1, provides a temporary solution for the data conversion between the solid element model and the structural element model [1]. Established structural design processes are mainly based on cross-sectional forces [16, 33], such as axial force, shear force and bending moment. The outputs of solid element analysis, i.e., nodal forces and displacements, need to be efficiently converted to the structural element forces, which can be used for the structural design. This may lead to frequent usage of solid element models in the field of civil engineering.

In this section, we seek to develop a method of converting a solid element solution to a structural element solution [13], based on the meta-modeling theory. As it will be explained later in this section, the most suitable beam element solution is found for a given solid element solution, by minimizing the *distance* between them. This conversion method will contribute to promoting the solid element analysis since i) cross sectional force or moment is more accurately computed for a given solid element solution, compared to an ordinary method which merely computes surface integration of stress [12, 13, 15]; and ii) a structural element solution could be used as smart initial guess of solid element analysis for a large scale model [15].

3.1.2 Meta-modeling theory for 1D structure

In this section, we explicitly explain the meta-modeling theory of a one-dimensional (1D) structural theory, i.e., bar (or truss) and beam which are coupled. The meta-modeling theory

requests to solve a variational problem of $\mathcal{L}^*$ of Eq. (2.2), by using a suitable subset of continuum mechanics' function space. Denote this space by S, i.e.,

$$S = \{u_1(\mathbf{x}), u_2(\mathbf{x}), u_3(\mathbf{x}), \sigma_{11}(\mathbf{x}), \sigma_{22}(\mathbf{x}), \sigma_{33}(\mathbf{x}), \sigma_{23}(\mathbf{x}), \sigma_{31}(\mathbf{x}), \sigma_{12}(\mathbf{x})\},$$

where $\mathbf{x}$ stands for a three-dimensional coordinate. As for truss theory, we choose the following subset:

$$S^T = \{u_1(x_1), 0,0, \sigma(x_1), 0,0,0,0,0\};$$

the axis of the truss is chosen in the x_1-direction. A non-zero component of $\boldsymbol{\epsilon} = sym\{\boldsymbol{\nabla}\mathbf{u}\}$ for $\mathbf{u}$ in S^T is the normal strain component in the x_1- direction, i.e., $\epsilon = {u_1}'$ with prime standing for the derivative with respect to x_1. Hence, $\delta\mathcal{L}^* = 0$ with respect to σ yields $\sigma = E\epsilon$, and then $\delta\mathcal{L}^* = 0$ with respect to u_1 yields

$$(AE{u_1}')' = 0,$$

where A is the area of cross section of the truss axis (or the x_1- direction).

As a more general case, we consider that bending in the x_2- and x_3- directions is coupled with the above uniaxial deformation of truss theory. Again, according to the meta-modeling theory, we only choose a subset of S to approximately solve the variational problem of $\mathcal{L}^*$ of Eq. (2.2). The chosen subset is

$$S^{TB} = \{u_1(x_1) - x_2 u_2^{\prime(x_1)} - x_3 u_3^{\prime(x_1)}, u_2(x_1), u_3(x_1), \sigma(x_1), 0,0,0,0,0\}.$$

For $\mathbf{u}$ in S^{TB}, a non-zero component of strain is the normal strain in the x_1-direction, i.e., $\epsilon = {u_1}' - x_2{u_2}'' - x_3{u_3}''$. Hence, $\delta\mathcal{L}^* = 0$ with respect to σ yields $\sigma = E({u_1}' - x_2{u_2}'' - x_3{u_3}'')$, and $\delta\mathcal{L} = 0$ with respect to u_1, u_2 and u_3 yields

$$(AE{u_1}')' = 0, \qquad (EI_2{u_2}'')'' = 0, \qquad (EI_3 u_3'')'' = 0$$

where I_2 and I_3 are the second-order moments of inertia in the x_2- and x_3- directions, respectively.

3.1.3 Development of the tool

Based on meta-modeling, a beam element solution (which includes a truss element in it) is regarded as an approximate numerical solution of a variational problem of $\mathcal{L}^*$ of Eq. (2.2). It is natural to make the conversion from a solid element solution to a beam element solution, by finding a set of functions in the function space of S that is close to the solid element solution. It should be noted that the converted beam element solution does not satisfy the discretized governing equations, even though the solid element solution does.

A L2 norm is used as distance in the function space of S. That is, denoting by $(\mathbf{u}^s, \boldsymbol{\sigma}^s)$ and $(\mathbf{u}^c, \boldsymbol{\sigma}^c)$ a beam and a solid element solution, respectively, we define

$$N(\mathbf{u}^s, \boldsymbol{\sigma}^s) = \frac{|\mathbf{u}^s - \mathbf{u}^c|^2}{|\mathbf{u}^c|^2} + \frac{|\boldsymbol{\sigma}^s - \boldsymbol{\sigma}^c|^2}{|\boldsymbol{\sigma}^c|^2}, \tag{3.1}$$

where $|\cdot|^2$ is the L2 norm which is computed by integrating vector or tensor norm of $\mathbf{u}$ or $\boldsymbol{\sigma}$, over V, i.e.,

$$|\mathbf{u}|^2 = \int_V \mathbf{u}\cdot\mathbf{u}\,\mathrm{d}v, \qquad |\boldsymbol{\sigma}|^2 = \int_V \boldsymbol{\sigma}\cdot\boldsymbol{\sigma}\,\mathrm{d}v\,.$$

A solid element solution $(\mathbf{u^c}, \boldsymbol{\sigma^c})$ is now expressed in terms of generalized nodal displacement as follows:

$$u_i^c = \sum_\alpha u_i^\alpha \eta^\alpha(x), \qquad \sigma_{ij}^c = \sum_\alpha c_{ijkl} u_k^\alpha \eta_{,i}^\alpha\,(x),$$

where $u^{\boldsymbol{\alpha}}$ and η^α are the α^{th} nodal displacement and shape function, and $\eta_{,i}^\alpha$ stands for the i-th component of η^α's gradient, $\boldsymbol{\nabla}\eta^\alpha$. In terms of discretized w and θ_2, a uniaxial beam element solution is expressed as

$$u_1^s = \sum_\alpha \; -x_3\left(w^\alpha \frac{\mathrm{d}\xi_w^\alpha}{\mathrm{d}x_1} + \theta_2^\alpha \frac{\mathrm{d}\xi_\theta^\alpha}{\mathrm{d}x_1}\right),$$

$$u_3^s = \sum_\alpha \; (w^\alpha \xi_w^\alpha + \theta_2^\alpha \xi_\theta^\alpha),$$

$$\sigma_{11}^s = \sum_\alpha \; -Ex_3\left(w^\alpha \frac{\mathrm{d}^2\xi_w^\alpha}{\mathrm{d}x_1^2} + \theta_2^\alpha \frac{\mathrm{d}^2\xi_\theta^\alpha}{\mathrm{d}x_1^2}\right),$$

where ξ_w^α and ξ_θ^α are the α-th beam element shape function for vertical displacement and rotation. Minimization of Eq. (3.1) with respect to w^α and θ_2^α results in

$$\sum_\beta \left\{ \begin{bmatrix} A_w^{\alpha\beta} & B_w^{\alpha\beta} \\ A_\theta^{\alpha\beta} & B_\theta^{\alpha\beta} \end{bmatrix} \begin{bmatrix} w^\beta \\ \theta_2^\beta \end{bmatrix} - \begin{bmatrix} C_{w,i}^{\alpha\beta} & D_w^{\alpha\beta} \\ C_{\theta,i}^{\alpha\beta} & D_\theta^{\alpha\beta} \end{bmatrix} \begin{bmatrix} u_i^\beta \\ u_3^\beta \end{bmatrix} \right\} = \begin{bmatrix} 0 \\ 0 \end{bmatrix}, \tag{3.2}$$

where,

$$A_w^{\alpha\beta} = \int \left(I_2 \frac{\mathrm{d}\xi_w^\alpha}{\mathrm{d}x_1}\frac{\mathrm{d}\xi_w^\beta}{\mathrm{d}x_1} + A\xi_w^\alpha \xi_w^\beta + WE^2 I_2 \frac{\mathrm{d}^2\xi_w^\alpha}{\mathrm{d}x_1^2}\frac{\mathrm{d}^2\xi_w^\beta}{\mathrm{d}x_1^2} \right) \mathrm{d}x_1,$$

$$B_w^{\alpha\beta} = \int \left(I_2 \frac{\mathrm{d}\xi_w^\alpha}{\mathrm{d}x_1}\frac{\mathrm{d}\xi_\theta^\beta}{\mathrm{d}x_1} + A\xi_w^\alpha \xi_\theta^\beta + WE^2 I_2 \frac{\mathrm{d}^2\xi_w^\alpha}{\mathrm{d}x_1^2}\frac{\mathrm{d}^2\xi_\theta^\beta}{\mathrm{d}x_1^2} \right) \mathrm{d}x_1,$$

$$C_{w,i}^{\alpha\beta} = -\int \left(\delta_{i1} x_3 \frac{\mathrm{d}\xi_w^\alpha}{\mathrm{d}x_1}\eta^\beta + WEc_{11ij} x_3 \frac{\mathrm{d}^2\xi_w^\alpha}{\mathrm{d}x_1^2}\frac{\mathrm{d}\eta^\beta}{\mathrm{d}x_j} \right) \mathrm{d}v,$$

$$D_w^{\alpha\beta} = \int \xi_w^\alpha \eta^\beta \,\mathrm{d}v.$$

It should be noted that from $\xi_w^\alpha \rightarrow \xi_\theta^\beta$ (where "→" is a replacement symbol),

$$A_w^{\alpha\beta} \rightarrow A_\theta^{\alpha\beta}, \qquad B_w^{\alpha\beta} \rightarrow B_\theta^{\alpha\beta}, \qquad C_{w,i}^{\alpha\beta} \rightarrow C_{\theta,i}^{\alpha\beta}, \qquad D_w^{\alpha\beta} \rightarrow D_\theta^{\alpha\beta},$$

with,

$$A = \int \mathrm{d}x\mathrm{d}y, \qquad I_2 = \int x_3^2 \,\mathrm{d}A, \qquad W = \frac{|\mathbf{u^c}|^2}{|\boldsymbol{\sigma^c}|^2}, \qquad \delta_{i1} - Kronecker's\ delta.$$

In a similar fashion, the case of biaxial bending in beam can be treated, the non-zero components which are u_1^s, u_2^s, u_3^s and σ_{11}^s; the beam element analysis computes $u_2^s = v$, $u_3^s = w$ and determines $u_1^s = u - x_3 w' - x_2 v'$ and $\sigma_{11}^s = E(u' - x_3 w'' - x_2 v'')$. In terms of discretized w, v, u, θ_3 and θ_2, a beam element solution is expressed as

$$u_1^s = \sum_\alpha \left[u^\alpha \xi^\alpha(x) - x_3 \left(w^\alpha \frac{\mathrm{d}\xi_w^\alpha}{\mathrm{d}x_1} + \theta_2^\alpha \frac{d\xi_\theta^\alpha}{dx_1} \right) - x_2 \left(v^\alpha \frac{\mathrm{d}\xi_w^\alpha}{\mathrm{d}x_1} + \theta_3^\alpha \frac{\mathrm{d}\xi_\theta^\alpha}{\mathrm{d}x_1} \right) \right],$$

$$u_2^s = \sum_\alpha (v^\alpha \xi_w^\alpha + \theta_3^\alpha \xi_\theta^\alpha), \qquad u_3^s = \sum_\alpha (w^\alpha \xi_w^\alpha + \theta_2^\alpha \xi_\theta^\alpha),$$

$$\sigma_{11}^s = \sum_\alpha E \left[u^\alpha \frac{\mathrm{d}\xi^\alpha}{\mathrm{d}x_1} - x_3 \left(w^\alpha \frac{\mathrm{d}^2\xi_w^\alpha}{\mathrm{d}x_1^2} + \theta_2^\alpha \frac{\mathrm{d}^2\xi_\theta^\alpha}{\mathrm{d}x_1^2} \right) - x_2 \left(v^\alpha \frac{\mathrm{d}^2\xi_w^\alpha}{\mathrm{d}x_1^2} + \theta_3^\alpha \frac{\mathrm{d}^2\xi_\theta^\alpha}{\mathrm{d}x_1^2} \right) \right],$$

where ξ^α is the beam element shape function for axial displacement. Minimization of Eq. (3.1) with respect to u^α, v^α, w^α, θ_y^α and θ_z^α results in

$$\sum_\beta \left\{ \begin{bmatrix} A_w^{\alpha\beta} & B_w^{\alpha\beta} & E_w^{\alpha\beta} & F_w^{\alpha\beta} & 0 \\ A_\theta^{\alpha\beta} & B_\theta^{\alpha\beta} & E_\theta^{\alpha\beta} & F_\theta^{\alpha\beta} & 0 \\ E_w^{\alpha\beta} & F_w^{\alpha\beta} & G_w^{\alpha\beta} & H_w^{\alpha\beta} & 0 \\ E_\theta^{\alpha\beta} & F_\theta^{\alpha\beta} & G_\theta^{\alpha\beta} & H_\theta^{\alpha\beta} & 0 \\ 0 & 0 & 0 & 0 & K^{\alpha\beta} \end{bmatrix} \begin{bmatrix} w^\beta \\ \theta_2^\beta \\ v^\beta \\ \theta_3^\beta \\ u^\beta \end{bmatrix} - \begin{bmatrix} C_{w,i}^{\alpha\beta} & 0 & D_w^{\alpha\beta} \\ C_{\theta,i}^{\alpha\beta} & 0 & D_\theta^{\alpha\beta} \\ J_{w,i}^{\alpha\beta} & D_w^{\alpha\beta} & 0 \\ J_{\theta,i}^{\alpha\beta} & D_\theta^{\alpha\beta} & 0 \\ L_i^{\alpha\beta} & 0 & 0 \end{bmatrix} \begin{bmatrix} u_i^\beta \\ u_2^\beta \\ u_3^\beta \end{bmatrix} \right\} = \begin{bmatrix} 0 \\ 0 \\ 0 \\ 0 \\ 0 \end{bmatrix}. \tag{3.3}$$

Here,

$$E_w^{\alpha\beta} = \int \left(I_{32} \frac{\mathrm{d}\xi_w^\alpha}{\mathrm{d}x_1} \frac{\mathrm{d}\xi_w^\beta}{\mathrm{d}x_1} + WE^2 I_{32} \frac{\mathrm{d}^2\xi_w^\alpha}{\mathrm{d}x_1^2} \frac{\mathrm{d}^2\xi_w^\beta}{\mathrm{d}x_1^2} \right) \mathrm{d}x_1,$$

$$F_w^{\alpha\beta} = \int \left(I_{32} \frac{\mathrm{d}\xi_w^\alpha}{\mathrm{d}x_1} \frac{\mathrm{d}\xi_\theta^\beta}{\mathrm{d}x_1} + WE^2 I_{32} \frac{\mathrm{d}^2\xi_w^\alpha}{\mathrm{d}x_1^2} \frac{\mathrm{d}^2\xi_\theta^\beta}{\mathrm{d}x_1^2} \right) \mathrm{d}x_1,$$

$$G_w^{\alpha\beta} = \int \left(I_3 \frac{\mathrm{d}\xi_w^\alpha}{\mathrm{d}x_1} \frac{\mathrm{d}\xi_w^\beta}{\mathrm{d}x_1} + A\xi_w^\alpha \xi_w^\beta + WE^2 I_3 \frac{\mathrm{d}^2\xi_w^\alpha}{\mathrm{d}x_1^2} \frac{\mathrm{d}^2\xi_w^\beta}{\mathrm{d}x_1^2} \right) \mathrm{d}x_1,$$

$$H_w^{\alpha\beta} = \int \left(I_3 \frac{\mathrm{d}\xi_w^\alpha}{\mathrm{d}x_1} \frac{\mathrm{d}\xi_\theta^\beta}{\mathrm{d}x_1} + A\xi_w^\alpha \xi_\theta^\beta + WE^2 I_3 \frac{\mathrm{d}^2\xi_w^\alpha}{\mathrm{d}x_1^2} \frac{\mathrm{d}^2\xi_\theta^\beta}{\mathrm{d}x_1^2} \right) \mathrm{d}x_1,$$

$$J_{w,i}^{\alpha\beta} = -\int \left(\delta_{i1} x_2 \frac{\mathrm{d}\xi_w^\alpha}{\mathrm{d}x_1} \eta^\beta + WEc_{11ij} x_2 \frac{\mathrm{d}^2\xi_w^\alpha}{\mathrm{d}x_1^2} \frac{\mathrm{d}\eta^\beta}{\mathrm{d}x_j} \right) \mathrm{d}v,$$

$$K^{\alpha\beta} = \int \left(A\xi^\alpha \xi^\beta + WE^2 \frac{\mathrm{d}\xi^\alpha}{\mathrm{d}x_1} \frac{\mathrm{d}\xi^\beta}{\mathrm{d}x_1} \right) \mathrm{d}x_1,$$

$$L_i^{\alpha\beta} = \int \left(\delta_{i1} \xi^\alpha \eta^\beta + WEc_{11ij} \frac{\mathrm{d}\xi^\alpha}{\mathrm{d}x_1} \frac{\mathrm{d}\eta^\beta}{\mathrm{d}x_j} \right) \mathrm{d}v,$$

from $\xi_w^\alpha \rightarrow \xi_\theta^\beta$,

$$E_w^{\alpha\beta} \to E_\theta^{\alpha\beta}, \quad F_w^{\alpha\beta} \to F_\theta^{\alpha\beta}, \quad G_w^{\alpha\beta} \to G_\theta^{\alpha\beta}, \quad H_w^{\alpha\beta} \to H_\theta^{\alpha\beta}, \quad J_{w,i}^{\alpha\beta} \to J_{\theta,i}^{\alpha\beta}, \quad D_w^{\alpha\beta} \to D_\theta^{\alpha\beta},$$

with,

$$I_3 = \int x_2^2 \, \mathrm{d}A, \quad I_{32} = \int x_3 x_2 \, \mathrm{d}A.$$

Equation (3.3), which is supposed to be used to obtain beam solution field, can be modified considering a symmetry of cross-section. Symmetry of the cross-section causes I_{32} to be zero, then

$$E_w^{\alpha\beta} = 0, \quad F_w^{\alpha\beta} = 0, \quad E_\theta^{\alpha\beta} = 0, \quad F_\theta^{\alpha\beta} = 0.$$

The uniaxial or biaxial beam displacement field can be obtained by solving Eq. (3.2) or (3.3). The force field of the beam can be found by using the displacement field via Eq. (3.4). Figure 3.1 shows the procedure of the conversion method which produces the beam displacement field with the consistent beam force field.

$$\begin{aligned}
&\text{Axial force along } x_1 && = && EAu_1{}' \\
&\text{Bending moment about } x_2 && = && -EI_2u_3{}'' \\
&\text{Bending moment about } x_3 && = && -EI_3u_2{}'' \\
&\text{Shear force along } x_3 && = && -EI_2u_3{}''' \\
&\text{Shear force along } x_2 && = && -EI_3u_2{}'''
\end{aligned} \tag{3.4}$$

3.1.4 Numerical verification of the tool

Non- prismatic members are widely used in steel portal frames to create well distributed stresses in the structure so that the utilization of steel can be optimized [24]. A straightforward technique used earlier to analyze a tapered beam is to divide it into a number of uniform elements [34], even though it is inefficient. The governing differential equations for tapered members with variable coefficients and closed solutions cannot be derived except for a few special cases [35].

This is a straightforward problem for meta-modeling based conversion method which is being proposed in this section. The typical conversion method merely computes surface integration of solid element nodal forces to estimate the beam shear force and the nodal displacement is averaged to estimate the beam displacement. The integration is not easy when the element configuration is not uniform, and the accuracy is often lost when the cross section of interest has only a few (or zero) nodes on it. The beam solution space that is obtained from the Bernoulli-Euler beam modeling has a clear relationship between each component of the solid element solution; see Eq. (3.4).

A tapered circular cantilever beam is tested for uniaxial bending in this numerical validation test. The parameters for this example are shown in Fig. 3.2; the parameters are for the loading, dimensions and material properties of the problem.

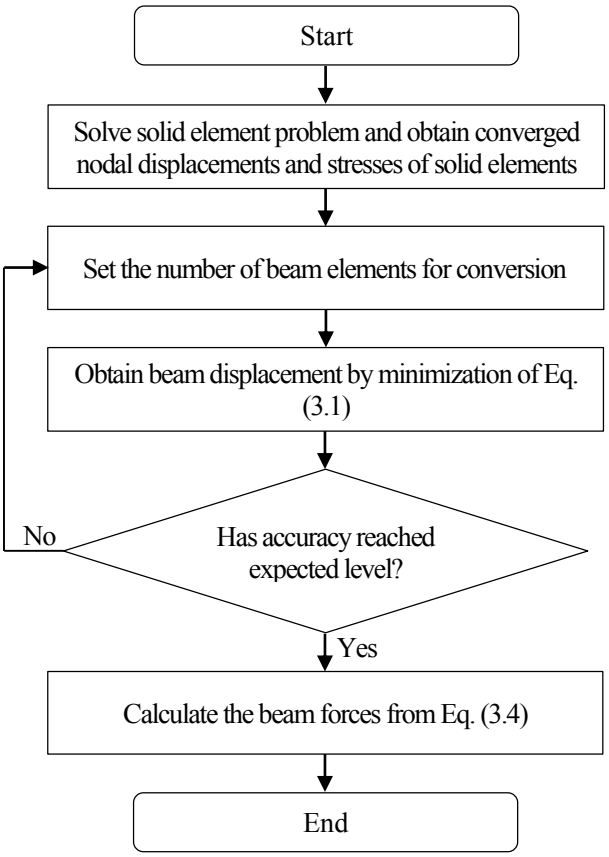

Figure 3.1: Flow chart of meta-modeling based conversion method.

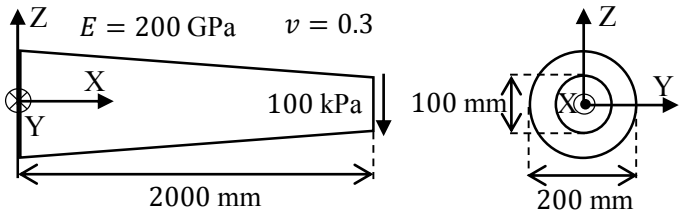

Figure 3.2: Schematic view of tapered circular cantilever member.

3.1.4.1 Results and discussion

The relative difference in converting a solid element solution to a beam element solution according to the proposed method is shown in Fig. 3.3(a); an analytical solution is used for the reference. Distance in the beam solution space is used for the analytical beam solution and the converted beam solution, and this difference is negligible. As for the function, the largest difference occurs near the fixed end of the cantilever, which is expected due to violation of the Bernoulli-Euler assumption near to the fixed end. Figure 3.3(a) does not include results at the fixed end of the cantilever due to a presence of zero in analytical beam solution.

Figure 3.3(b) shows the relative difference of vertical displacement component of the converted solution, compared with that obtained by the finer beam element model. According to the flow chart that is presented in Fig. 3.1, the objective of this conversion is a solution of finer beam element model that is obtained from the given solid element

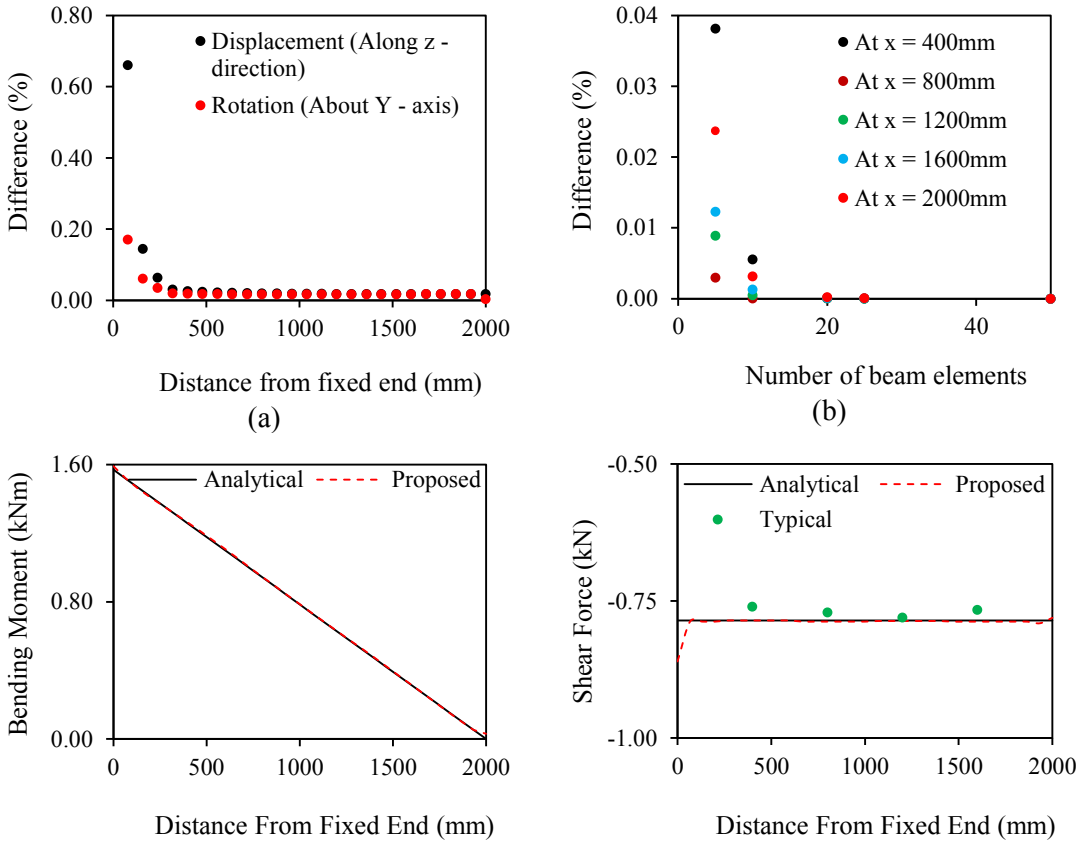

Figure 3.3: Data conversion of tapered circular cantilever member: (a) absolute percentage differences compared with beam analytical solution; (b) absolute percentage differences of displacement compared with finer beam element model solution; (c) bending moment diagram (about y-axis); and (d) shear force diagram (along z-direction).

Table 3.1: Absolute percentage difference compared with analytical shear force result $\left(\frac{\text{Abs(AS}-\text{TM or PM)}\times 100}{\text{AS}}\right)$.

Location (mm)	Proposed method	Typical method
400	0.01	3.30
800	0.25	1.91
1200	0.11	0.66
1600	0.26	2.50

solution. The finer beam element model contains 100 beam elements in this problem. The number of the beam elements in the target problem is reduced while keeping the same level of accuracy according to Fig. 3.3(b). Depending on the type of the problem, the level of accuracy for a beam element solution is fixed; the level mainly depends on the level of accuracy of the given solid element solution. For a given level of accuracy, an acceptable number of beam elements is determined. A user has freedom to choose the number, depending on the accuracy level that is required. As shown in this example, the acceptable number of the beam elements is 10 to 100; see Fig. 3.3(b).

Figure 3.3(c) shows the distribution of the bending moment obtained by the proposed method and that of the analytical solution. The distribution is smooth over an

entire target domain of the beam model except near the fixed end. The accuracy of computing the bending moment is clearly seen in this figure.

A distribution of shear force is presented in Fig. 3.3(d). This diagram includes shear force distribution that is obtained by the proposed method, a typical method which uses integration, and an analytical solution that solves the Bernoulli-Euler beam problem. There is a difference between the bending moment computed by the proposed method and the analytical solution at the fixed end of the cantilever; this difference is due to the violation of the beam assumption near the fixed end. The comparison of the distribution of the two methods of converting a solid element solution with the analytical solution is displayed in Table 3.1. As shown in this table, the accuracy of the proposed method is higher than the typical method. We should mention that the typical method only produces cross-section wise conversion; see Fig. 3.3(d). The proposed conversion method has a capability to estimate cross sectional forces for the whole domain of the model, since it converts the solution or the displacement and force functions unlike the typical method.

3.2 Construction of consistent lumped mass model (CLMM) based on meta-modeling

3.2.1 Overview

Lumped mass model is popular on account of its simplicity and conservative prediction of the response; see references [8, 9, 10, 36, 37, 38, 39]. As for a typical lumped mass model, the target structure is discretized with a set of beam elements. A lumped mass for each node of the model is estimated from the portion of the weight of the target structure, which is called “tributary area consideration”. There are mainly two ways to estimate the stiffness of a spring in a lumped mass model, namely, a static method and a geometric method. The static method uses an arbitrary static load applied to a single layer of the full (3D) finite element model. This is similar to a pushover analysis [5]. The geometric method considers the geometric shape of the cross-section, in order to calculate the sectional moment of inertia and shear coefficients.

In constructing a lumped mass model as explained above we do not consider the consistency of the model with the physical problem or with other more sophisticated models. This is mainly because it is easy to tune the lumped mass model, in order to reproduce observed or synthesized dynamic response; tuning is usually applied to the stiffness of the springs. According to our view point, simplicity does not have to destroy consistency. Even though a set of models of different fidelity is available, each model ought to solve the same physical problem (that is a Largrangian problem of continuum mechanics). In order to relate a lumped mass model, we propose a methodology based on the meta-modeling theory [11, 14] in this section.

3.2.2 Development of the tool

According to the meta-modeling theory explained in Chapter 2, a lumped mass model which is consistent with a continuum mechanics model is obtained by substituting approximate functions of displacement to the modified Lagrangian; see Appendix B for the definition of the approximate functions. As a simple example, we consider a pier of a bridge. We regard the pier as a cantilever, and choose approximate functions that

correspond to the beam at quasi-static state. Functions which correspond to the beam at dynamic state can be used as other approximate functions; see Section 5.1.

According to the meta-modeling theory, the approximate displacement functions of the following form are used:

$$\{u_1, u_2, u_3\} = U(t)\{-zw'(x), 0, w(x)\}, \tag{3.5}$$

where u_1, u_2 and u_3 are displacement components in the x_1-, x_2- and x_3-directions, respectively, with (x_1, x_2, x_3) being the Cartesian coordinate. For simplicity, we replace (x_1, x_2, x_3) with (x, y, z) when we consider approximate functions; for instance, the x_3 component, $u_3(x_1, x_2, x_3)$, is approximated as $w(z)$, and $U(t)$ is the amplitude of the displacement mode that is caused by the horizontal force at the top. Then, w is a solution of the following beam problem:

$$\begin{cases} (EIw'')'' = 0 & 0 < x < L, \\ (w, w') = (0,0) & x = 0, \\ (w, w'') = (1,0) & x = L. \end{cases} \tag{3.6}$$

Note that the coordinate x is chosen in the vertical direction and, for simplicity, z is taken in the horizontal direction which lays on the bending plane of the pier; E is Young's modulus and I is the second moment of area with respect to the z-direction, and L is the height. The function of w is determined since Eq. (3.6) has a unique solution. Substituting $\mathbf{u}$ of Eq. (3.5) and the corresponding $\boldsymbol{\sigma}$, we calculate the modified Lagrangian as

$$\mathcal{L} = \frac{1}{2}M\dot{U}^2(t) - \frac{1}{2}KU^2(t), \tag{3.7}$$

where

$$\{M, K\} = \int \{\rho(Aw^2 + I(w')^2), EI(w'')^2\}\, \mathrm{d}x \tag{3.8}$$

with A being the cross-sectional area of the pier.

It should be emphasized that, while $\int \rho A w^2\, \mathrm{d}x$ is usually used as a mass of the pier, the meta-modeling theory yields $\int \rho I (w')^2\, \mathrm{d}x$ as additional mass, which accounts for the effect of angular momentum. While Bernoulli-Euler beam theory neglects it, Shear beam modeling includes this angular momentum effect. Therefore, the lumped mass modeling as given by the Lagrangian of Eq. (3.7) is in accordance with the Shear beam modeling that is known to be more accurate than Bernoulli-Euler beam modeling.

Besides translation, we can readily include rotation in the consistent lumped mass modeling. We use other approximate displacement functions,

$$\{u_1, u_2, u_3\} = \Theta(t)\{-zh'(x), 0, h(x)\}, \tag{3.9}$$

where $\Theta(t)$ is the amplitude of displacement mode that is induced by rotational force at the top, and h is a solution of the following beam problem:

$$\begin{cases} (EIh'')'' = 0 & 0 < x < L, \\ (h, h') = (0,0) & x = 0, \\ (h', h''') = (1,0) & x = L. \end{cases} \tag{3.10}$$

The modified Lagrangian is computed in the same form as Eq. (3.7) if $\{M, K\}$ of Eq. (3.8) are computed by using h instead of w.

The modified Lagrangian for coupling of translation and rotation is readily obtained by substituting the sum of $\mathbf{u}$ given by Eqs. (3.5) and (3.9). That is,

$$\mathcal{L} = \frac{1}{2}M_U\dot{U}^2(t) - \frac{1}{2}K_U U^2(t) + \frac{1}{2}M_\Theta\dot{\Theta}^2(t) - \frac{1}{2}K_\Theta\Theta^2(t) + M_{U\Theta}\dot{U}(t)\dot{\Theta}(t) - K_{U\Theta}U(t)\Theta(t), \tag{3.11}$$

where $\{M_U, K_U\}$ and $\{M_\Theta, K_\Theta\}$ are given by Eq. (3.8) using w and h, respectively, and

$$\{M_{U\Theta}, K_{U\Theta}\} = \int \{\rho(Awh + Iw'h'), EIw''h''\}\, \mathrm{d}x. \tag{3.12}$$

As it is seen, the coupling between translation and rotation naturally appears via $\{M_{U\Theta}, K_{U\Theta}\}$ of Eq. (3.12).

In substituting the sum of $\mathbf{u}$ given by Eqs. (3.5) and (3.9), we have to pay attention to coupling of translation and rotation. For instance, at $x = L$, we have

$$u_3 = U + \Theta h(L), \quad \frac{\partial u_3}{\partial x_1} = Uw'(L) + \Theta;$$

recall that $w(L) = 1$ and $h'(L) = 1$. The right side of the above equations is the quantity that can be measured. Therefore, the measured data should be compared with $\{U + \Theta h(L), Uw'(L) + \Theta\}$, rather than $\{U, \Theta\}$.

3.2.3 Numerical verification of the tool

Before employing the developed CLMM for the seismic response analysis, we have to check the quality of the model. To this end, we employ a solid element model which is developed by using *ADVC* [40, 41]. A selected pier geometry of simple bridge for this quality check is shown in Fig. 3.4. This simple bridge includes only one pier with 7.5 m height and bridge deck acts as rigid body in both the longitudinal and transverse directions of the bridge. The rotation degree of freedom of the bridge deck also prevents in this simple model. The construction of the CLMM is described in the next paragraphs.

As explained in the preceding section, a lumped mass model requires two parameters, namely, an equivalent mass and a stiffness coefficient [42, 43, 44]. According to the meta-modeling theory, lumped mass modeling is to use the approximate displacement functions of Eq. (3.5); recall that $U(t)$ is an unknown function. The modified Lagrangian yields an ordinary differential equation for $U(t)$, and the mass and stiffness are computed by using $w(x)$.

As for this bridge structure, we use quasi-static beam theory to determine w, assuming that the pier provides stiffness and the deck moves like a rigid body. That is, setting the x_1- and x_2-axes parallel and normal to the bridge direction, respectively, and setting the x_3-axis as the vertical direction, we use approximate functions of the following form:

$$\{u_1, u_2, u_3\} = \begin{cases} U(t)\{-xw'(z), 0, w(z)\} & 0 < z < H, \\ U(t)\{-xw'(H), 0, w(H)\} & H < z < H + T, \end{cases} \tag{3.13}$$

where $x = x_1$ and $z = x_3$; $0 < z < H$ is for a pier and $H < z < H + T$ is for a deck; H and T are the height of the pier and the thickness of the deck, respectively. Note that the displacement function of the above ensures that the deck moves as a rigid body. Posing suitable boundary conditions, we can determine w. For instance, we choose

$$w(0) = 0, w'(0) = 0, w(H) = 1, w'(H) = 0,$$

which interprets the boundary conditions at $z = 0$ and $z = H$ as the zero displacement with the zero rotation and the unit displacement with the zero rotation, respectively. Here, setting $w(H) = 1$ means that $U(t)$ is the displacement of the pier top as well as the movement of the whole deck.

The approximate function w, which is selected according to quasi-static beam theory, is fully determined by solving the boundary value problem. When it is given, the modified Lagrangian becomes

$$\mathcal{L} = \frac{1}{2} M \dot{U}^2(t) - \frac{1}{2} K U^2(t), \tag{3.14}$$

where

$$M = M_d + \int_0^H \rho(Aw^2 + I(w')^2)\, \mathrm{d}z, \tag{3.15}$$

$$K = \int_0^H EI(w'')^2\, \mathrm{d}z, \tag{3.16}$$

with A and I being the cross section area and the second moment of inertia of pier, respectively. M_d is the lumped mass of the deck. In this experiment, it is 252827 kg.

In the same manner, we can construct a lumped mass model in the transverse direction. The approximate functions are

$$\{u_1, u_2, u_3\} = \begin{cases} U(t)\{-yw'(z), 0, w(z)\} & 0 < z < H, \\ U(t)\{-yw'(H), 0, w(H)\} & H < z < H + T. \end{cases}$$

The solid model is constructed based on the same geometric configuration as shown in Fig. 3.4, except part(b), the same material properties presented in Table 3.2 are used; for part(b), the density and Young's modulus are changed as 14,555.14 kg/m^3 and 25,000 GPa; the density of the part (b) is changed, in order to account for the mass of the deck which is included in the span and simplified in the model, and the stiffness of the part (b) is changed, as well, in order to allow rigid body motion.

3.2.3.1 Results and discussion

Natural frequencies of the lumped mass model and the equivalent solid model are calculated, and the results are summarized in Table 3.3. Note that, due to the symmetry, the natural frequency of the lumped mass model in the longitudinal direction coincides with that in the transverse direction. Comparison of the natural frequencies ensures that the differences of the natural frequencies are less than 0.175%. Therefore, we conclude that the quality of the consistent lumped mass model is within an acceptable level.

Linear elastic seismic responses of the two models are compared for further inspection of the quality of the CLMM. For a given set of ground motion data, the maximum

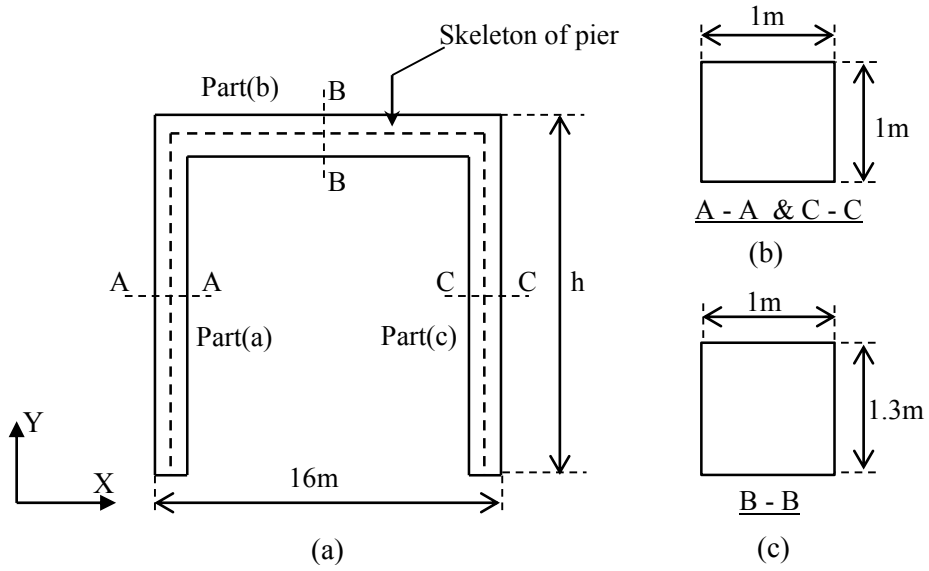

Figure 3.4: The geometry of simple bridge pier: (a) cross section of bridge pier; (b) cross section of A-A; and (c) cross section of B-B.

Table 3.2: Material properties and lumped mass information.

Density of pier (Concrete)	2400kg/m^3
Density of deck (Steel)	7800kg/m^3
Young's modulus (Concrete)	25GPa
Young's modulus (Steel)	200GPa
Damping ratio (Concrete)	5%

Table 3.3: Natural frequency results of both solid element and lumped mass models in both directions.

Model	Transverse / (Hz)	Longitudinal / (Hz)
Lumped mass	3.426	3.426
Solid	3.420	3.421

displacements are computed for the CLMM and the solid model; 20 ground motions are used in both the longitudinal and transverse directions. The relative differences of the maximum displacements of the CLMM with respect to that of the solid model are presented in Fig. 3.5(a) and (b), for the ground motions in the longitudinal and transverse directions, respectively. As is seen, there are some differences. This is mainly because the CLMM accounts for the 1st bending mode only, while the solid model a few modes. The maximum difference occurs at the 12th input ground motion in the transverse direction; see Fig. 3.6(a) for the ground motion. The difference in the time series response of displacement is shown in Fig. 3.6(b). Since the maximum difference is 0.065 mm, we conclude that the quality of the CLMM remains within an acceptable level, just like the quality check in terms of the natural frequency.

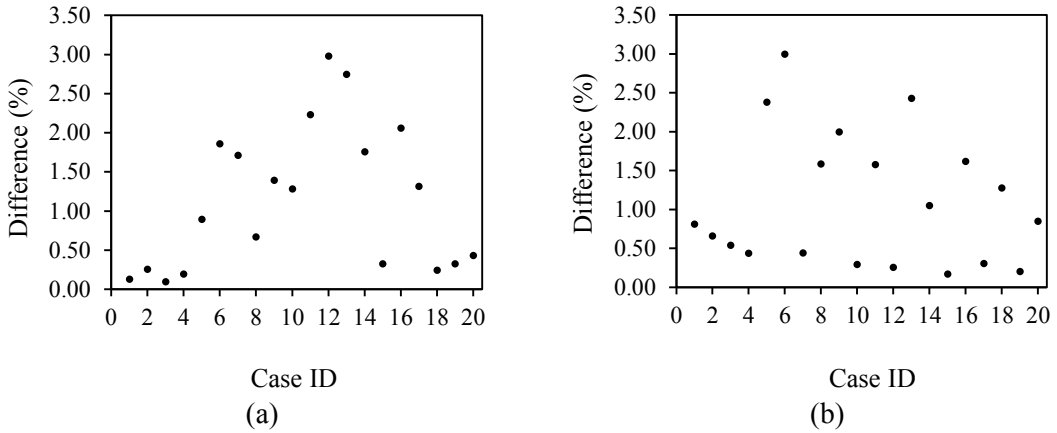

Figure 3.5: Percentage difference of maximum displacement between solid element analysis and lumped mass analysis: (a) along transverse direction; and (b) along longitudinal direction.

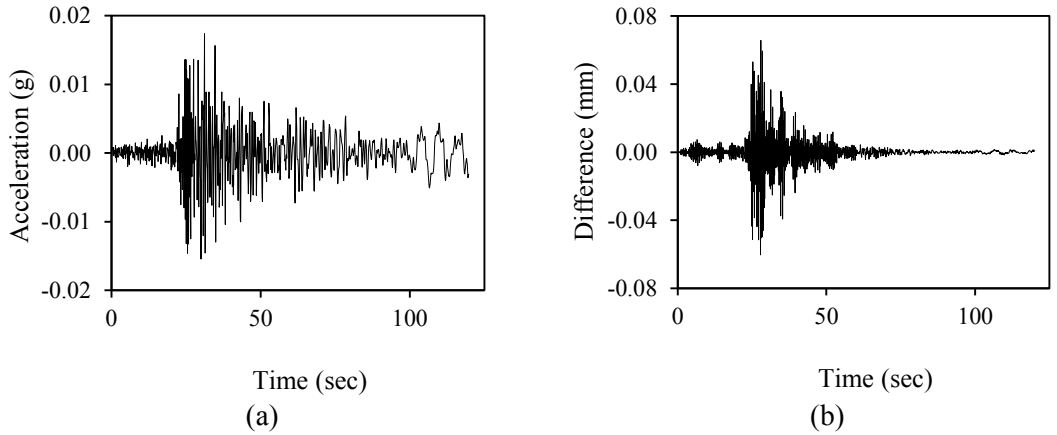

Figure 3.6: Case 12 (verification of CLMM): (a) input ground motion along transverse direction; and (b) absolute difference between solid element analysis and lumped mass model analysis along transverse direction.

It is taken for granted that for such a ground motion as stimulates higher modes, a lumped mass model that accounts for the first model only fails to provide an accurate seismic response. It is thus needed to improve the model so that it is able to take into consideration the effects of higher modes on the responses. We explain this improvement of the lumped mass model which uses modal analysis in Chapter 5.

3.3 Construction of consistent mass spring model (CMSM) based on meta-modeling

3.3.1 Overview

There are some limitations of the CLMM which was developed in this chapter. They are; 1) working with only single mass point, 2) applicable to limited geometric shape and 3) dependence of accuracy of response based on location of mass point in the system. It is surely desirable that a lumped mass model that has the same fundamental dynamic

characteristics as more sophisticated models is constructed for any arrangement of mass points. To overcome these limitations of the CLMM a new consistent mass spring model (CMSM) is proposed in this subsection.

Proposed CMSM contains two mass points with three springs which will be discussed in this subsection later. The displacement response of this CMSM is independent of locations of mass points in the system. In this subsection, first we clarify approximations which are made in deriving governing equation for a mass spring system from a continuum mechanics theory. Numerical verification of developed CMSM is carried out by considering both beam theory solution and solid element solutions with enough results presented at the end of this section.

3.3.2 Development of the tool

A mass spring model is a set of masses and linear springs, and the direction of the mass movement is fixed. As the simplest case, we study a mass spring model which consists of two masses. We seek to construct a mass spring model which shares the same fundamental dynamic characteristics as continuum mechanics; this model is called consistent mass spring model (CMSM).

3.3.2.1 General formulation

According to the meta-modeling theory, we consider an approximate displacement function of the following form:

$$\mathbf{u}(\mathbf{x},t)=\sum_{\alpha=1}^{2}U^{\alpha}(t)\boldsymbol{\phi}^{\alpha}(\mathbf{x}), \tag{3.17}$$

where $U^{\alpha}(t)$ is displacement of the α-th mass point and $\boldsymbol{\phi}^{\alpha}$ is the corresponding displacement mode.

By definition, the displacement is required to satisfy the following two requirements:

A1) $\boldsymbol{\phi}^{\alpha}(\mathbf{x}^{\alpha})$ is a unit vector.

A2) $\boldsymbol{\phi}^{\alpha}(\mathbf{x}^{\beta})$ vanishes for $\alpha\neq\beta$.

Here, $\mathbf{x}^{\alpha}$ is the location of the α-th mass point. We substitute Eq. (3.17) into Eq. (2.1), and obtain

$$\mathcal{L}=\sum_{\alpha,\beta=1}^{2}\frac{1}{2}m^{\alpha\beta}\dot{U}^{\alpha}\dot{U}^{\beta}-\frac{1}{2}k^{\alpha\beta}U^{\alpha}U^{\beta}, \tag{3.18}$$

where

$$m^{\alpha\beta}=\int_{V}\rho\boldsymbol{\phi}^{\alpha}\boldsymbol{\phi}^{\beta}\,\mathrm{d}v \text{ and } k^{\alpha\beta}=\int_{V}\boldsymbol{\nabla}\boldsymbol{\phi}^{\alpha}:\mathbf{c}:\boldsymbol{\nabla}\boldsymbol{\phi}^{\beta}\,\mathrm{d}v. \tag{3.19}$$

Since a Lagrangian of a conventional mass spring model of two masses is in the form of

$$\frac{1}{2}(\cdot)\left(\dot{U}^1\right)^2+\frac{1}{2}(\cdot)\left(\dot{U}^2\right)^2-\frac{1}{2}(\cdot)(U^2-U^1)^2-\frac{1}{2}(\cdot)(U^2)^2$$

with $(\cdot)$ being a suitable scalar, $\mathcal{L}$ of Eq. (3.18) becomes the above, if the following two requirements are satisfied:

B1) $m^{12}=0$.

B2) $k^{12}+k^{22}=0$.

It is readily seen that finding two functions $\boldsymbol{\phi}^1$ and $\boldsymbol{\phi}^2$ which satisfy the four conditions of A1, A2, B1 and B2 is generally not possible.

3.3.2.2 General formulation for $\mathcal{L}^*$

When $\mathbf{c}$ is isotropic, we can construct a consistent mass spring system using Young's modulus only. We introduce $\boldsymbol{\sigma}$ whose non-zero component is σ_{11} only; we choose the x_1-axis as the longitudinal direction for a structure like a bar or a beam. Substitution of Eq. (3.17) and $\sigma_{11}=S\phi^\sigma$ into Eq. (2.2) leads

$$\mathcal{L}^*=\sum_{\alpha,\beta=1}^{2}\frac{1}{2}m^{\alpha\beta}\dot{U}^\alpha\dot{U}^\beta-\sum_\alpha Sa^\alpha U^\alpha+\frac{b}{2E}S^2, \tag{3.20}$$

where

$$a^\alpha=\int_V\phi^\sigma(\boldsymbol{\nabla}\boldsymbol{\phi}^\alpha)_{11}\,\mathrm{d}v,\ b=\int_V(\phi^\sigma)^2\,\mathrm{d}v. \tag{3.21}$$

It follows from $\delta\mathcal{L}^*=0$ with respect to S that

$$S=\sum_\alpha\frac{E}{b}a^\alpha U^\alpha, \tag{3.22}$$

and $\mathcal{L}^*$ becomes

$$\mathcal{L}^*=\sum_{\alpha,\beta=1}^{2}\frac{1}{2}m^{\alpha\beta}\dot{U}^\alpha\dot{U}^\beta-\frac{E}{2b}a^\alpha a^\beta U^\alpha U^\beta. \tag{3.23}$$

Note that only E appears in this $\mathcal{L}^*$, unlike $\mathcal{L}$ with $k^{\alpha\beta}$ that is computed by using $\mathbf{c}$.

3.3.2.3 Utilization of dynamic modes

Dynamic modes ought to be used in constructing a mass spring model, so that it shares the same dynamic fundamental characteristics with a continuum model. We suppose that two dynamic modes $\{\boldsymbol{\psi}^\alpha,\omega^\alpha\}$ ($\alpha=1$ or 2), are given; $\boldsymbol{\psi}^\alpha$ is a mode shape and ω^α is a natural frequency. Recall that the dynamic mode satisfies

$$\rho(\omega^\alpha)^2\boldsymbol{\psi}^\alpha+\boldsymbol{\nabla}\cdot(\mathbf{c}\colon\nabla\boldsymbol{\psi}^\alpha)=0, \tag{3.24}$$

and

$$\int_V\rho\boldsymbol{\psi}^\alpha\cdot\boldsymbol{\psi}^\beta\,\mathrm{d}v=0,\quad\int_V\boldsymbol{\nabla}\boldsymbol{\psi}^\alpha\colon\mathbf{c}\colon\boldsymbol{\nabla}\boldsymbol{\psi}^\beta\,\mathrm{d}v=0, \tag{3.25}$$

for $\omega^{\alpha} \neq \omega^{\beta}$.

For simplicity, we use $\mathcal{L}$ of Eq. (2.1), and, substituting $\mathbf{u} = \sum u^{\alpha}\boldsymbol{\psi}^{\alpha}$ into it, we obtain

$$\mathcal{L} = \sum_{\alpha,\beta=1}^{2} \frac{1}{2} m^{\alpha}\left(\dot{U}^{\alpha}\right)^{2} - \frac{1}{2} k^{\alpha}(U^{\alpha})^{2}, \tag{3.26}$$

where

$$m^{\alpha} = \int_{V} \rho \boldsymbol{\psi}^{\alpha} \cdot \boldsymbol{\psi}^{\beta}\, \mathrm{d}v,\ k^{\alpha} = \int_{V} \boldsymbol{\nabla}\boldsymbol{\psi}^{\alpha} : \mathbf{c} : \boldsymbol{\nabla}\boldsymbol{\psi}^{\beta}\, \mathrm{d}v. \tag{3.27}$$

Due to the orthogonality, Eq. (3.25), $\{\boldsymbol{\psi}^{\alpha}\}$ does not produce cross terms. Furthermore, due to Eq. (3.24), it is readily seen that m^{α} and k^{α} of Eq. (23) satisfy

$$(\omega^{\alpha})^{2} m^{\alpha} = k^{\alpha}, \tag{3.28}$$

for $\alpha = 1$ and 2.

Now, we seek to find suitable linear combinations of $\{\boldsymbol{\psi}^{\alpha}\}$ that satisfy the requirements A1 and A2. To this end, we consider the following combination:

$$\boldsymbol{\phi}^{\alpha} = \sum t^{\alpha\beta}\, \boldsymbol{\psi}^{\alpha}, \tag{3.29}$$

where $t^{\alpha\beta}$ is a component of two-by-two matrix. It is readily seen that this matrix can be determined when $\boldsymbol{\psi}^{1}$ and $\boldsymbol{\psi}^{2}$ do not change the direction and are parallel to each other.

3.3.3 Numerical verification of the tool with beam theory solution

Simple cantilever beam with uniform cross-section is used for this numerical verification of the tool with the beam theory solution; see Fig. 3.7(a) for geometric and material properties of numerical test. Linear isotropic elasticity is assumed. In this discussion two mass points (M_1 and M_2) are located at 2m and 0.8m distance from the fixed end of cantilever respectively. It should be emphasized that the frequency response of CMSM does not depend on the locations of mass points. A schematic view of the CMSM with third spring which connects the first mass to the ground is shown in Fig. 3.7(b). The stiffness coefficients, K_1, K_2 and K_3, are computed as follows:

$$K_1 = k^{22} + k^{12}, \qquad K_2 = (-k^{12}) \qquad \text{and} \qquad K_3 = k^{11} + k^{12}.$$

where $k^{\alpha\beta}$'s are computed according to Eq. (3.19). The parameters of the CMSM are summarized in Tables 3.4 and 3.5. Input ground motion which is rich between 0Hz to 5Hz in frequency domain is shown in Fig. 3.9. This numerical verification test contains two cases considering contributed dynamic mode shapes ($\boldsymbol{\psi}^{\beta}$) of the cantilever problem to CMSM; see Fig. 3.10 for the first three dynamic mode shapes of cantilever problem. First case uses first and second dynamic modes while second case uses second and third.

3.3.3.1 Results and discussion

Calculated displacement mode shapes ($\boldsymbol{\phi}^{\alpha}$) in both cases are displayed in Fig. 3.11(a) and (b). Table 3.6 and 3.7 show the frequency response of each case with beam theory solution.

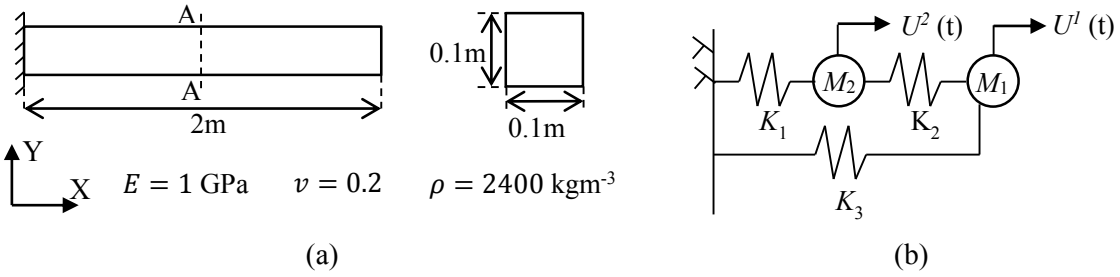

Figure 3.7: Schematic views: (a) a prismatic cantilever member; and (b) a consistent mass spring system consisting of two mass points.

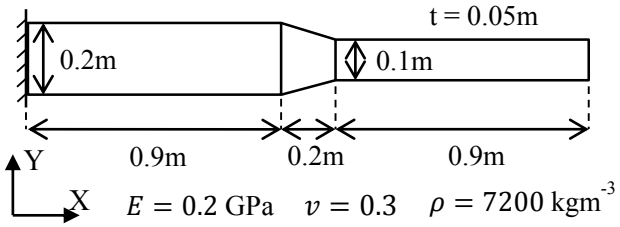

Figure 3.8: Schematic view of a non-prismatic 3D cantilever member (Uniform thickness t = 0.05m).

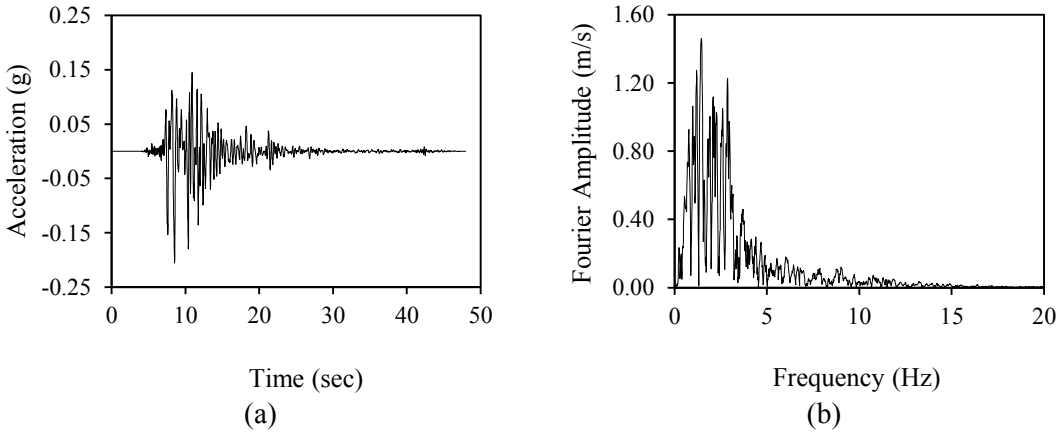

Figure 3.9: Input ground motion for prismatic cantilever member: (a) in time domain; and (b) in frequency domain.

As is seen, the natural frequencies of the CMSM coincide with those of the beam element model. Time series of displacement responses of two mass points for selected time interval in both cases are shown in Fig. 3.12 and 3.13. These results of CMSM are well matching with the frame solution but not at all in the second case; see Fig. 3.13(a) and (b). It is clear that we need to select major dynamic modes considering input ground motion to construct

the CMSM to obtain better results for displacement response. The relative errors of maximum displacement between beam and CMSM model are presented in Table 3.8.

The base shear and bending moment of the cantilever beam is computed. There are two approaches for computing this force. The first approach is conventional, and the base shear, F, is computed as the product of the stiffness and displacement, as

$$F(t) = K_1 U^2(t) + K_3 U^1(t). \tag{3.30}$$

And the bending moment, M, is computed as the product of the force acting on mass point and the distance between mass point and base (X_α), as

$$M(t) = X_2 K_1 U^2(t) + X_1 K_3 U^1(t). \tag{3.31}$$

The second approach uses the displacement function and the resulting force. The shear force and bending moment are computed as follows:

$$\mathbf{F}(t) = \sum u^\alpha(t) \left(EI\left(\boldsymbol{\psi}'''(\mathbf{x})\right)^\alpha \right), \tag{3.32}$$

$$\mathbf{M}(t) = \sum u^\alpha(t) \left(EI\left(\boldsymbol{\psi}''(\mathbf{x})\right)^\alpha \right), \tag{3.33}$$

Where E is Young's modulus and $I = \int z^2 \, \mathrm{d}y\mathrm{d}z$. When $\mathbf{x} = \mathbf{0}$, it corresponds to the base of the beam. This computation is logical in the sense that the present CMSM is essentially the same as the modal analysis [42, 43, 44], and is able to compute local responses by using the approximate displacement, i.e., $\mathbf{u} = \sum u^\alpha \boldsymbol{\psi}^\alpha$.

The base shears and bending moment computed by using Eqs. (3.30), (3.31), (3.32) and (3.33) are presented in Figs. 3.14 and 3.15 for case 1. It is displayed for the time interval selected from the full response. The base shear and bending moment computed by using the beam element model are also presented as the reference. As is seen from Table 3.9, the relative errors of the first approach are much higher than those of the second approach. It should be noted that, according to the definition of the spring constants, Eq. (3.19), the shear force and bending moment given by Eqs. (3.30) and (3.31) respectively are regarded as an average of forces acting in the beam; see Appendix C for more detailed explanation. However, both the methods give huge relative errors for base shear and bending moment estimation in case 2 due to poor selection of dynamic modes for construction process of the CMSM; see Table 3.9.

3.3.4 Numerical verification of the tool with solid element solution

A non-prismatic 3D cantilever beam with uniform thickness is employed, as a simple example of constructing a CMSM from a solid element model; see Fig. 3.8 for geometric configuration and material properties of the beam. Linear isotropic elasticity is assumed. A solid element model is constructed for this beam. We consider dynamic response in the y- and z-directions and call as case 1 and 2, respectively. Dynamic modes, $\{\boldsymbol{\psi}^\alpha, \omega^\alpha\}$, are computed for these cases, separately.

We locate two mass points at 2 m and 1 m distance from the fixed end. First two dynamic mode shapes, $\{\boldsymbol{\psi}^\alpha\}$, and approximate displacement functions, $\{\boldsymbol{\phi}^\alpha\}$, in the z-direction are displayed in Figs. 3.16 and 3.17, respectively. The parameters of the CMSM

are summarized in Tables 3.10 and 3.11. The ground motion which is rich between 5 Hz to 10 Hz in frequency domain is used as input for this test in both cases; see Fig. 3.18.

3.3.4.1 Results and discussion

Tables 3.12 and 3.13 present two natural frequencies of the CMSM in the both cases, together with those of the original solid element model. As is seen, the natural frequencies of the CMSM coincide with those of the solid element model.

Time series of displacement responses are compared with those of the original solid element model; see Fig. 3.19 for displacement responses of the time interval selected from the full response. It is seen that the response of CMSM in case 1 matches well with that of the solid element model but not in case 2. The difference in the responses is due to the fact that the CMSM uses only the first two modes. However, when input ground motion does not contain higher mode components, the difference is small such as in case 1. The relative errors of maximum displacement between solid and CMSM model are presented in Table 3.14.

The base shear of the cantilever beam is computed. Both the approaches are used for computing this force at the base. The second approach has been modified for solid element as follows.

$$\mathbf{F}(t) = \sum u^{\alpha}(t) \int \mathbf{n} \cdot \left(\mathbf{c}(\mathbf{x}) : \boldsymbol{\nabla}\boldsymbol{\psi}^{\alpha}(\mathbf{x})\right) \mathrm{ds}, \tag{3.34}$$

where $\mathbf{x} = \mathbf{0}$ corresponds to the base of the beam, $\mathbf{n}$ is the unit normal on base, and the surface integration is made on the base.

The base shears computed by using Eqs. (3.30) and (3.34) are presented in Fig. 3.20 for case 1. It is displayed for the time interval selected from the full response. The base shear computed by using the solid element model is also presented as the reference. As is seen from Table 3.15, the relative errors of the first approach are much higher than those of the second approach as we expected. However, both the methods give huge relative errors for base shear estimation in case 2 due to higher mode effect; see Table 3.15.

Table 3.4: CMSM stiffness parameters of prismatic cantilever member.

Stiffness parameter	Value / (Nm)	
	Case 1	Case 2
K_1	920247.663	1633730.561
K_2	53363.412	-270718.518
K_3	-47299.143	436623.125

Table 3.5: CMSM mass parameters of prismatic cantilever member.

Mass parameter	Value / (kg)	
	Case 1	Case 2
M_1	8.535	6.674
M_2	180.219	29.267
M_{12}	21.373	4.441

Table 3.6: Natural frequency of CMSM and prismatic cantilever beam model (case 1).

Selected mode	Frequency / (Hz)	
	CMSM	Beam
First	2.607	2.607
Second	16.337	16.337

Table 3.7: Natural frequency of CMSM and prismatic cantilever beam model (case 2).

Selected mode	Frequency / (Hz)	
	CMSM	Beam
Second	16.337	16.337
Third	45.743	45.743

Table 3.8: Relative error for maximum displacement between prismatic cantilever beam and CMSM models.

Case	Location	Error / %
1	M_1	0.733
	M_2	0.599
2	M_1	99.943
	M_2	96.485

Table 3.9: Relative error for maximum resulting force at base of prismatic cantilever member between beam and CMSM models.

Case	Force type	Error / (%)	
		1st approach	2nd approach
1	Shear force	127.895	0.927
	Bending moment	856.889	0.987
2	Shear force	91.281	94.215
	Bending moment	92.415	95.234

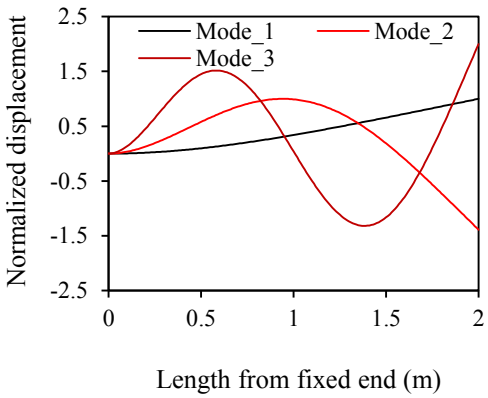

Figure 3.10: First three dynamic modes of the 2D cantilever problem.

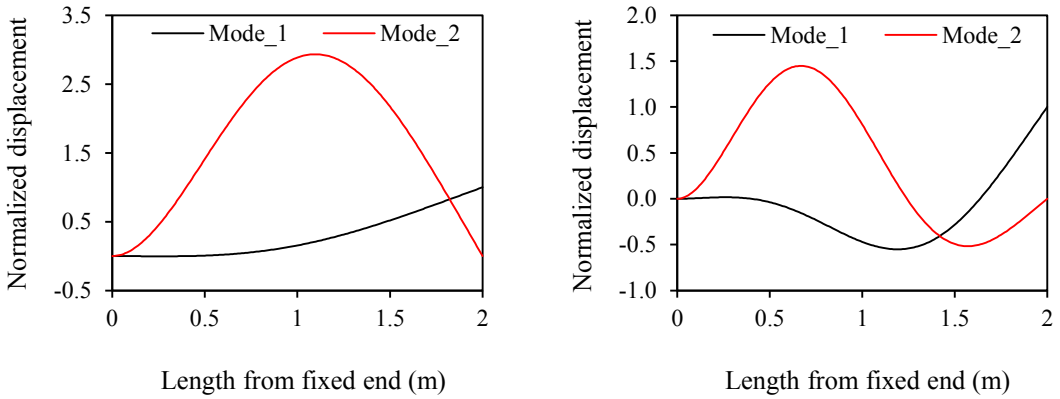

Figure 3.11: Developed approximate displacement modes: (a) case 1; and (b) case 2.

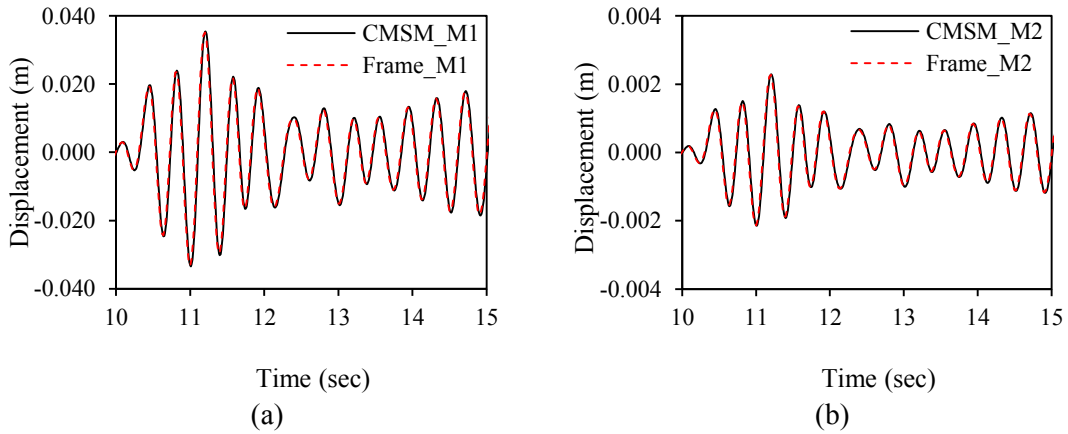

Figure 3.12: Displacement of prismatic cantilever member in case 1: (a) at M_1 location; and (b) at M_2 location.

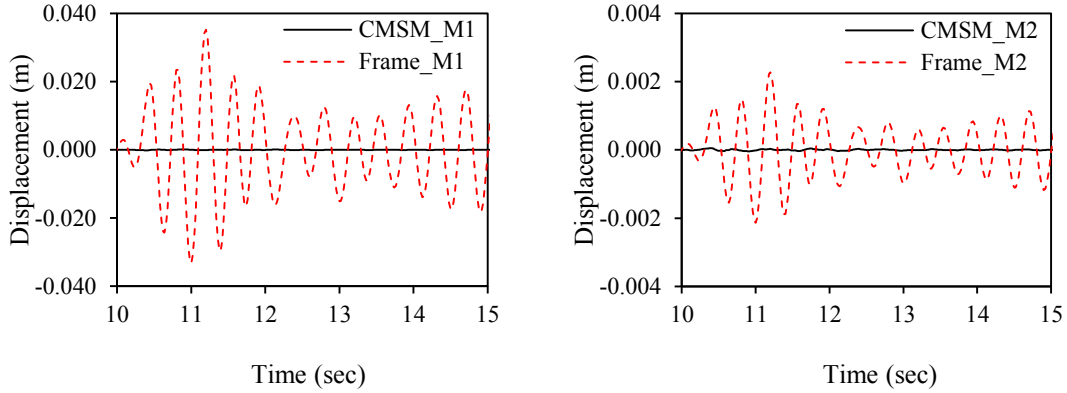

Figure 3.13: Displacement of prismatic cantilever member in case 2: (a) at M_1 location; and (b) at M_2 location.

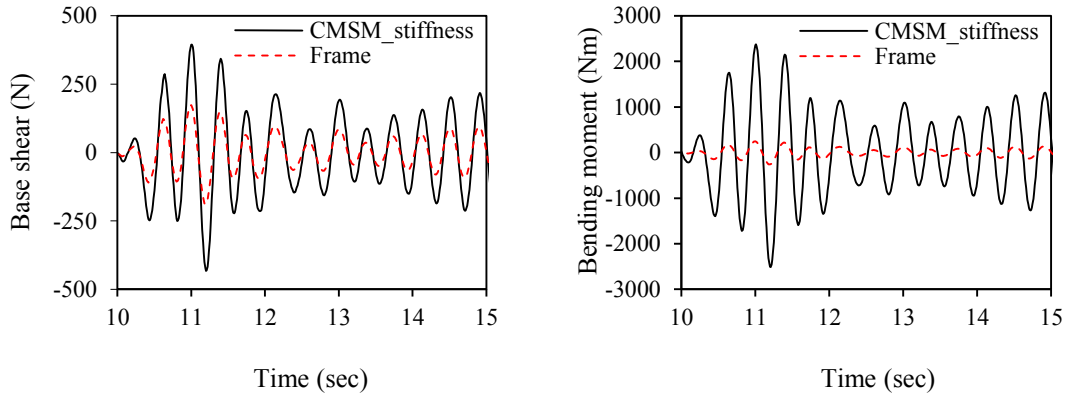

Figure 3.14: Resulting forces of prismatic cantilever problem from 1st approach in case 1: (a) base shear along y-direction; and (b) base bending moment around z-axis.

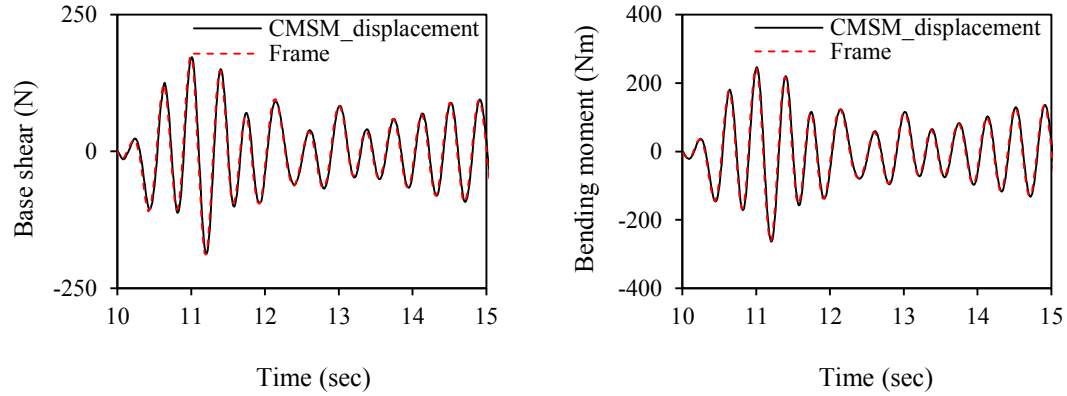

Figure 3.15: Resulting forces of prismatic cantilever problem from 2nd approach in case 1: (a) base shear along y-direction; and (b) base bending moment around z-axis.

Table 3.10: CMSM stiffness parameters of non-prismatic cantilever member.

Stiffness parameter	Value / (Nm)	
	Case 1	Case 2
K_1	6185.093	1218.625
K_2	28847.112	2976.364
K_3	-3678.061	-719.650

Table 3.11: CMSM mass parameters of non-prismatic cantilever member.

Mass parameter	Value / (kg)	
	Case 1	Case 2
M_1	8.803	9.758
M_2	48.206	45.169
M_{12}	6.987	5.814

Table 3.12: Natural frequency of CMSM and solid non-prismatic cantilever member model along y-direction (case 1).

Selected mode	Frequency / (Hz)	
	CMSM	Solid
First	1.623	1.623
Second	5.669	5.668

Table 3.13: Natural frequency of CMSM and solid non-prismatic cantilever member model along z-direction (case 2).

Selected mode	Frequency / (Hz)	
	CMSM	Solid
First	0.455	0.455
Second	2.151	2.150

Table 3.14: Relative error for maximum displacement between solid non-prismatic cantilever member and CMSM models.

Case	Location	Error / (%)
1	M_1	3.241
	M_2	2.940
2	M_1	12.85
	M_2	11.36

Table 3.15: Relative error for maximum base shear between solid non-prismatic cantilever member and CMSM models.

Case	Error / (%)	
	1st approach	2nd approach
1	16.923	3.744
2	94.133	71.393

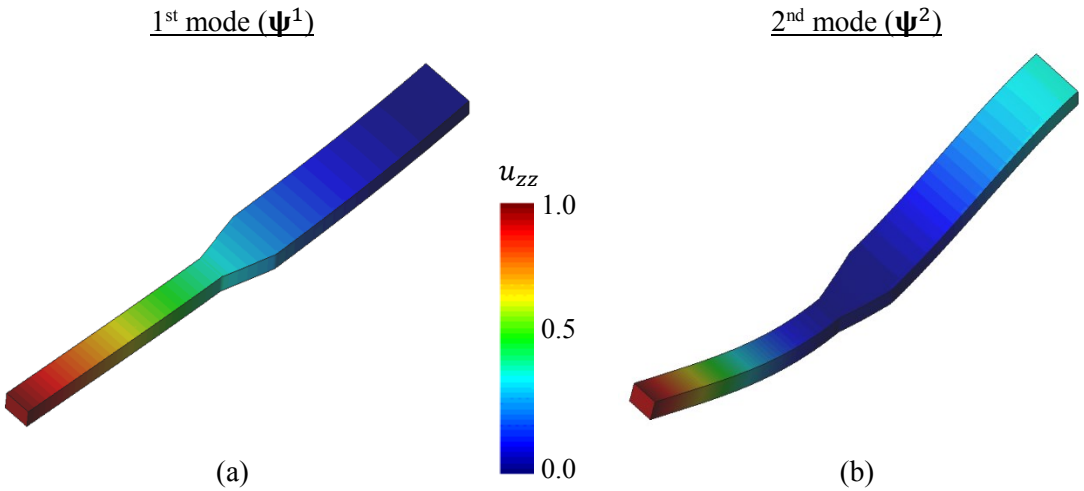

Figure 3.16: First two dynamic modes of non-prismatic cantilever member along z-direction (case 2).

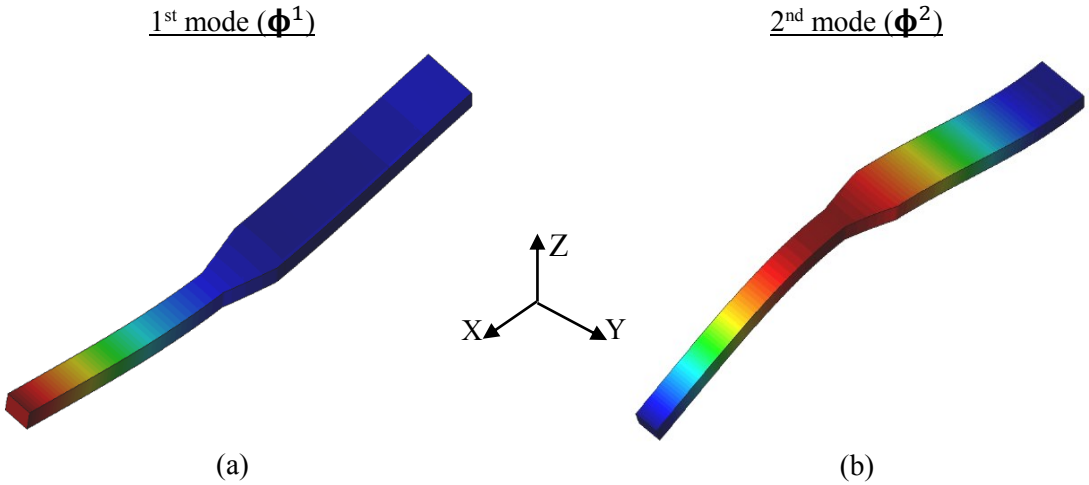

Figure 3.17: Developed approximate displacement modes of non-prismatic cantilever member along z-direction (case 2).

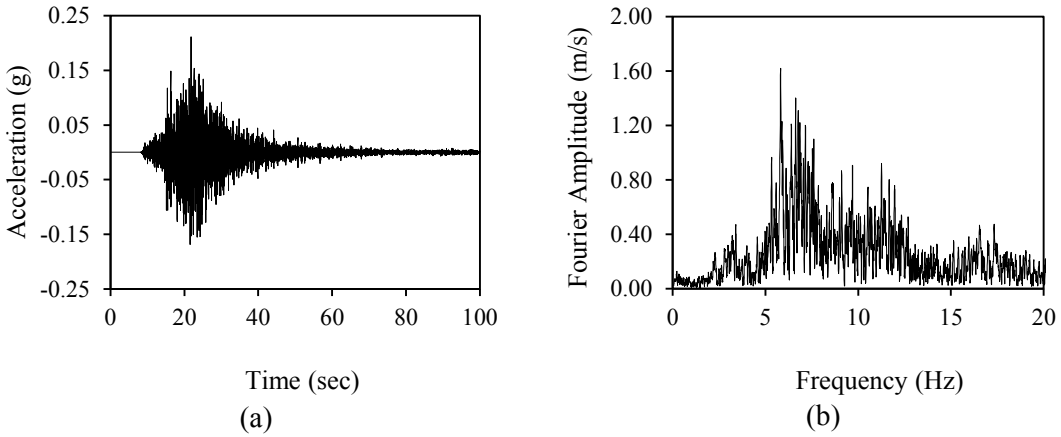

Figure 3.18: Input ground motion for non- prismatic cantilever member: (a) in time domain; and (b) in frequency domain.

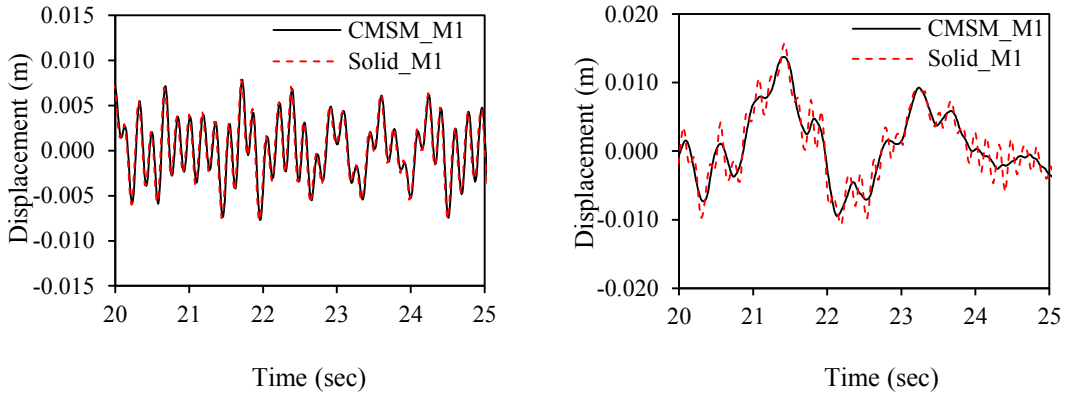

Figure 3.19: Displacement of non-prismatic cantilever at M_1 location: (a) along y-direction (case 1); and (b) along z-direction (case 2).

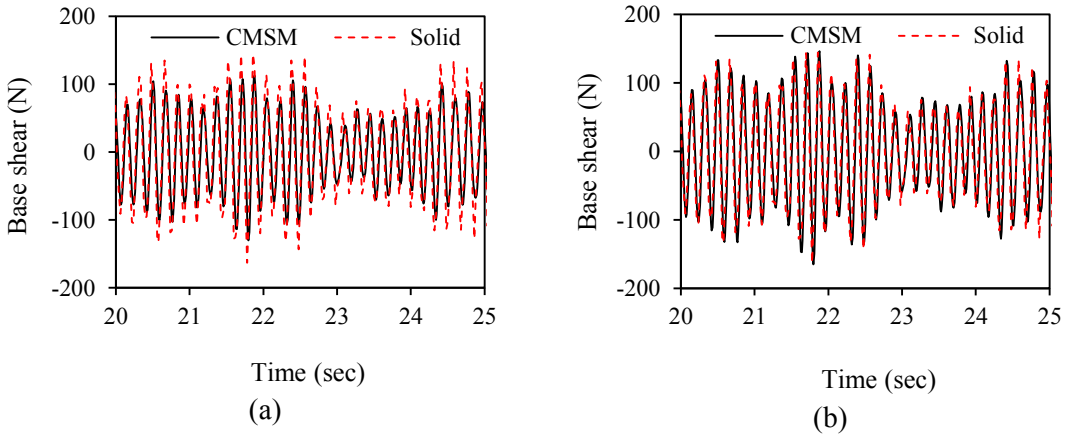

Figure 3.20: Base shear force of non-prismatic cantilever along z-direction in case 1: (a) 1st approach; and (b) 2nd approach.

Chapter 4

Numerical Experiments

4.1 Overview

The main aim of this chapter is implementations of the developed tools for practical numerical experiments in order to assess their capabilities in static and dynamic analysis. Most of the numerical experiments presented in this chapter discuss about a seismic response analysis of a bridge structure, which is the objective of this dissertation. When it comes to a large scale numerical experiment such as a bridge structure, automated process is introduced to overcome laboriousness of manual modeling since the number of target structures and structure components is huge.

The contents of this chapter are as follows. First, the rigorous conversion tool of solid and beam element solutions is employed to calculate beam cross-sectional forces from the solid element solution and estimate an initial guess for a CG method from the beam element solution in Section 2. Then, in Section 3, the CLMM is used with an automated construction process to obtain a seismic response for a freeway bridge structures. In Section 4, implementation of the CMSM is studied for single- and multi-span bridge structures under seismic loads in a consistent manner. Implementation of the meta-modeling based consistent models for quality assurance of the automated high fidelity bridge structures are studied at the end of this chapter.

4.2 Implementation of rigorous conversion of solid and beam element solution

4.2.1 Calculation of cross-sectional force from solid element solution

4.2.1.1 Biaxial bending in cantilever member

Biaxial bending in a beam or a column is commonly encountered in a structural analysis [46]. Prediction of bidirectional bending by the typical method is not a straightforward task due to coupling of the biaxial bending with an axial force. Decoupling of the biaxial bending moment needs curve fitting technique which is an extension of the typical method. The proposed meta-modeling based conversion method can handle this problem without any further modification. This is a good example showing the wide range of applicability of this proposed rigorous conversion method.

Cantilever with uniform square (200mm×200mm) cross-section is used in this numerical experiment. Figure 4.1 shows the problem setting of this numerical experiment with material data. Three displacement boundary conditions are located at the right end of cantilever system; these are 5mm, -5mm and -10mm along x, y and z directions respectively.

Results and discussion

According to Fig. 3.1, the aim is to obtain finer converged beam element solution from the given solid element solution space. Numerical validation of this method shows that there is an acceptable range of beam elements for the solid element to beam element conversion which mainly depends on the level of convergence of the given solid element space and form of work. The acceptable range of the beam elements for this numerical experiment is 10 to 100. In this numerical experiment 100 beam elements are employed to estimate the finer beam element solution space from the given solid element solution.

The beam forces which are consistent with obtained beam displacements are shown in Figs. 4.2(a), (b), (c) and (d) respectively. The biaxial bending moments in the cantilever that are obtained from the proposed meta-modeling based conversion method, are shown in Fig. 4.2(a). The proposed and typical conversion methods are employed to obtain beam shear forces (τ_{xy} , τ_{xz}) as seen in Fig. 4.2(b) and (c). Obtained beam axial forces in the both ways are presented in Fig. 4.2(d). Absolute percentage differences of predicted shear forces and axial force results by using the typical method, compared to the proposed method are shown in Table 4.1.

The proposed meta-modeling based conversion method [13] has the capability to provide the biaxial bending moment which is complicated to provide in the typical method. The proposed conversion method decouples the biaxial bending in displacement space but the typical method decouples it in force space which is more complicated to solve. Prediction of shear forces and axial force in the both ways gives marginally different solutions; see Table 4.1. Calculated shear forces from the proposed method have some deviation at the fixed end due to complex stress behavior at the fixed end of the cantilever.

This shear force deviation at the fixed end of cantilever cannot be observed from the shear force diagrams, because the amount of deviation is very small as compared with the overall value of shear force in the beam domain. Nevertheless, the solid element solution space of biaxial bending can be efficiently converted to the beam element solution space, with including bidirectional bending by using the proposed conversion method.

4.2.1.2 Ramp tunnel

Construction of long tunnels has increased rapidly due to higher demand of public transportation. These long tunnels need a ramp tunnel, which connects the main tunnel located under-ground to ground level. However, a ramp tunnel has a complicated structural behavior which cannot be accurately estimated from 2D model. A detailed analysis model of the ramp tunnel which is used in this numerical experiment, and large-scale numerical computation for the 3D ramp tunnel in seismic response analysis are well described in past works [1, 2]. 3D data conversion for one of the main tunnel parts that is shown in Fig. 4.4(b), is considered under this numerical experiment. This is a real field application where the meta-modeling based conversion method is directly applied to obtain beam solution field.

A target frequency range of 0Hz to 6Hz is selected for this analysis. A direction of input ground motion is shown in Fig. 4.4 which is parallel to the selected main tunnel. An input ground motion to a bedrock is shown in Fig. 4.3(a). Material properties and boundary conditions of the tunnel system were well described in the past studies [1, 2].

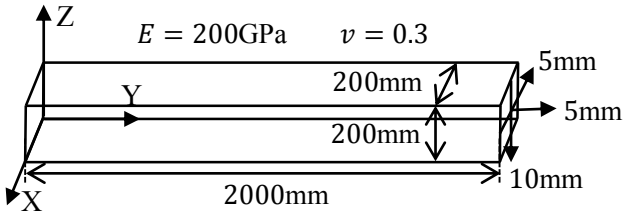

Figure 4.1: Schematic view of uniform cantilever member for data conversion.

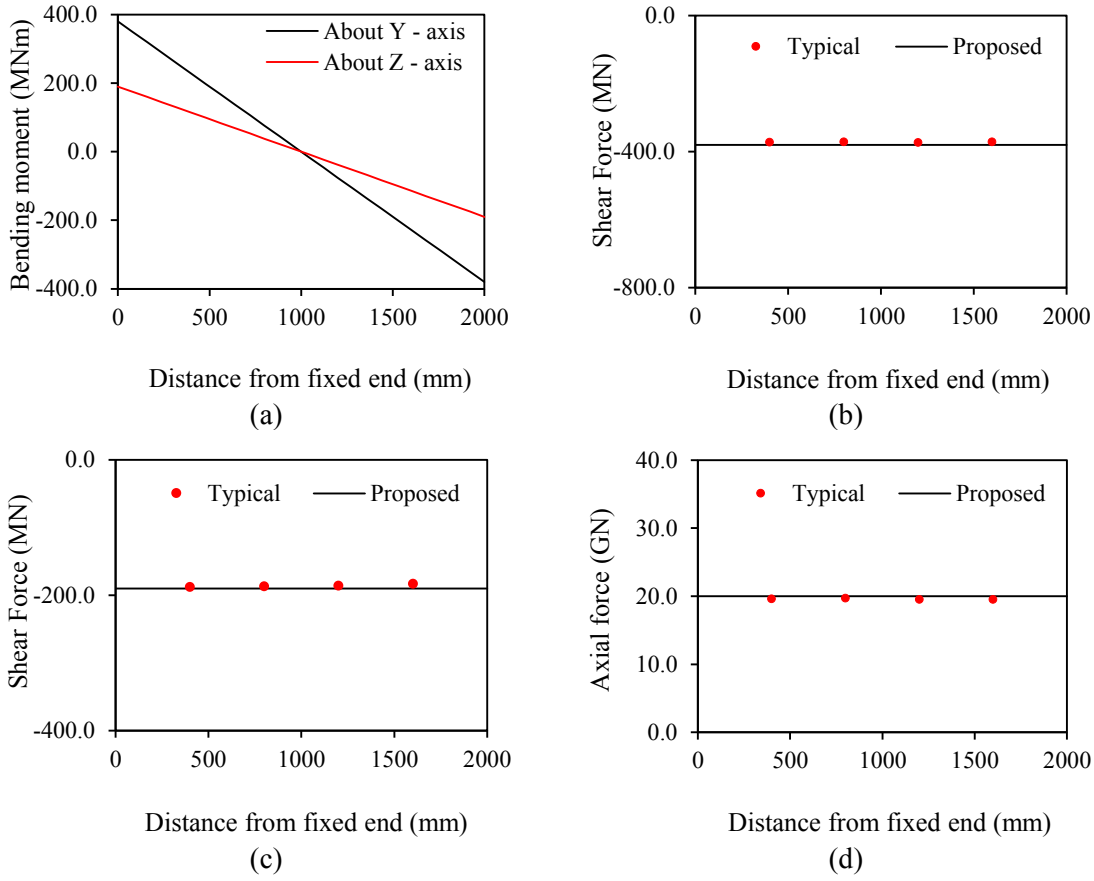

Figure 4.2: Data conversion of uniform cantilever member: (a) bending moment diagram; (b) shear force diagram (along z-direction); (c) shear force diagram (along y-direction); and (d) axial force diagram (along x-direction).

Table 4.1: Comparison of results (uniform cantilever member) between typical method and proposed method $\left(\frac{\text{Abs(PM}-\text{TM)}\times 100}{\text{PM}}\right)$.

Location (mm)	Axial force	Shear force (τ_{xy})	Shear force (τ_{xz})
400	2.09	1.88	1.09
800	1.53	2.14	1.59
1200	2.58	1.60	2.17
1600	2.61	2.15	3.86

Results and discussion

Conversion results which are presented in this numerical experiment belong to the solid result field of the 1650th time step out of 5000 time steps in the numerical analysis. A converged beam element solution is obtained from flow chart which is shown in Fig. 3.1. Beam bending moments which are consistent with the obtained beam displacement field are shown in Figures 4.3(b) and (c). Beam axial forces and shear force are calculated by using the both proposed and typical methods and results are presented in Table 4.2, 4.3 and 4.4, Figs. 4.3(d), (e) and (f).

In this numerical experiment, the main tunnel part of ramp tunnel acts as a rod rather than a beam due to the input ground motion direction. This can be seen clearly from the results of axial force and shear force diagrams; see Figs. 4.3(d), (e) and (f). The shear force and bending moment results are very small compared to section capacity of the main tunnel, though the proposed method shows the capability to obtain those results in acceptable level.

A rapid change is observed due to behavior of the input ground motion in the obtained beam force field results between 400m and 500m along the main tunnel axis. The proposed conversion method shows potential to estimate this type of local change effectively.

Absolute percentage difference of the typical method when compared with the proposed method in shear force shows a huge difference that cannot be observed in the axial load; see Table 4.2. It is already mentioned that the shear force in the main tunnel part is very small compared to the cross-sectional shear force capacity of the main tunnel. Results from Table 4.3 and 4.4, clearly indicate that the direct differences are not large and they are within a reasonable range. The meta-modeling based conversion method shows that it has the ability to detect beam solution from solid solution, in real practical problem effectively.

4.2.2 Meta-modeling based initial guess for conjugate gradient (CG) method

Meta-modeling could be used as new initial guess of a conjugate gradient (CG) method [47, 48, 49, 50, 51, 52] of solid element analysis; we have not found any study which seeks to apply physics based meta-modeling to an initial guess. The basic idea of this is to use a solid element solution converted from a beam element solution as an initial solution of the CG method.

To explain the above idea clearly, we denote by $\mathbf{u}^s$ and $\mathbf{u}^c$ the beam element solution and the converted solid element solution, respectively. The distance function in Eq. (3.1) can adjust for this task as follows:

$$N(\mathbf{u}^c, \boldsymbol{\sigma}^c) = \frac{|\mathbf{u}^s - \mathbf{u}^c|^2}{|\mathbf{u}^s|^2} + \frac{|\boldsymbol{\sigma}^s - \boldsymbol{\sigma}^c|^2}{|\boldsymbol{\sigma}^s|^2}. \tag{4.1}$$

Following an identical process as in Sec. 3.1.3, we can obtain similar expression as Sec. 3.1.3. Here definition of W needs to be changed as follows:

$$W = \frac{|\mathbf{u}^s|^2}{|\boldsymbol{\sigma}^s|^2}.$$

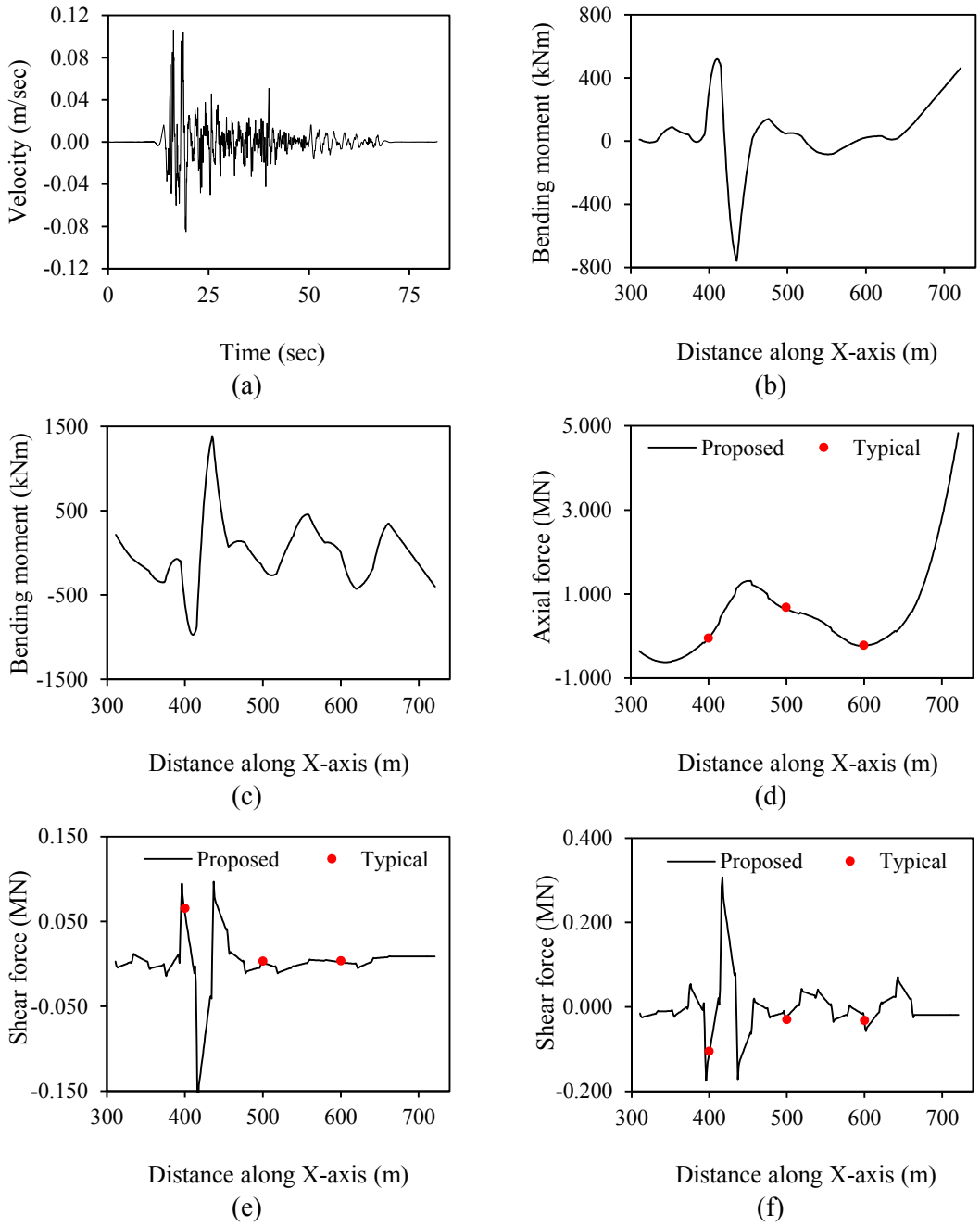

Figure 4.3: Data conversion of ramp tunnel structure: (a) Input ground motion on bed rock; (b) bending moment (about z-axis); (c) bending moment (about y-axis); (d) axial force (along x-direction); (e) shear force (along y-direction); and (f) shear force (along z-direction).

Since $\mathbf{u}^s$ is regarded as an approximate solution of the continuum mechanics problem, it is expected that $\mathbf{u}^c$ which is converted from $\mathbf{u}^s$ will serve as a good initial solution of the CG method; see Appendix D for CG algorithm.

Frame problem with lateral loading and cantilever beam with biaxial bending are discussed under this section to cover applications of the meta-modeling based initial guess for CG method. Here, the cantilever and frame problems are constructed in beam element and solid element solutions are obtained from the proposed CG method. These numerical

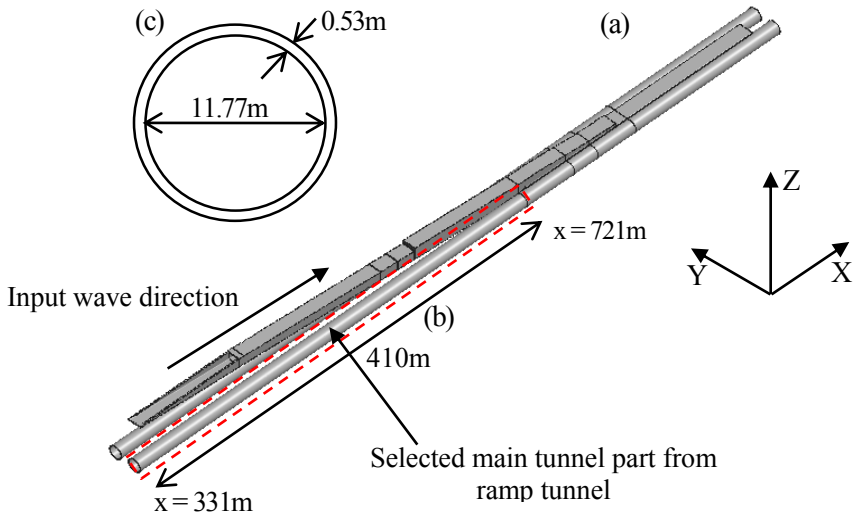

Figure 4.4: Ramp tunnel structure: (a) ramp tunnel; (b) selected main tunnel part; and (c) uniform cross-section of main tunnel.

Table 4.2: Comparison of results (ramp tunnel structure) between typical method and proposed method $\left(\frac{Abs(PM-TM)\times 100}{PM}\right)$.

Location / (m)	Axial force	Shear force (τ_{xy})	Shear force (τ_{xz})
400	5.40	8.57	3.79
500	5.63	60.57	23.39
600	2.16	55.29	14.37

Table 4.3: Shear force of main tunnel part (τ_{xy}) in each method at selected locations along x-axis.

Location / (m)	Proposed method / (kN)	Typical method / (kN)
400	-109.21	-105.22
500	-23.15	-30.22
600	-36.88	-32.24

Table 4.4: Shear force of main tunnel part (τ_{xz}) in each method at selected locations along x-axis.

Location/ (m)	Proposed method / (kN)	Typical method / (kN)
400	59.66	65.25
500	1.27	3.21
600	1.45	3.25

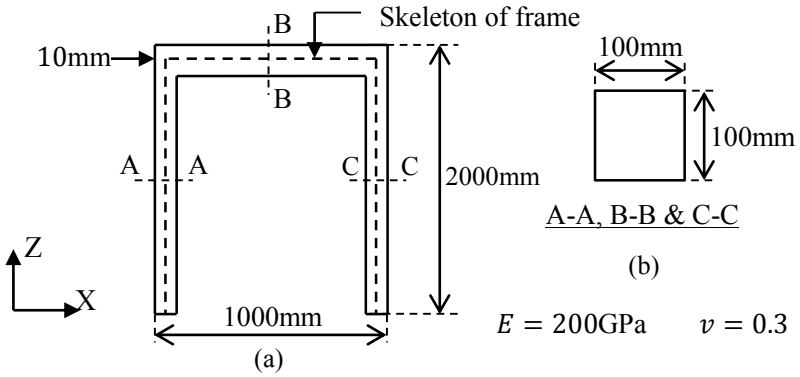

Figure 4.5: Schematic view of frame: (a) cross-section of frame; and (b) cross-section of A-A, B-B & C-C.

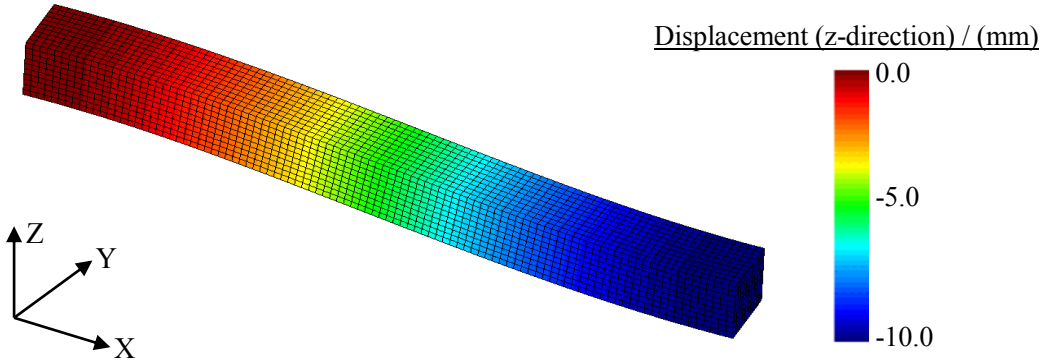

Figure 4.6: Approximated displacement (z–direction) for solid element system from equivalent beam element system (cantilever problem).

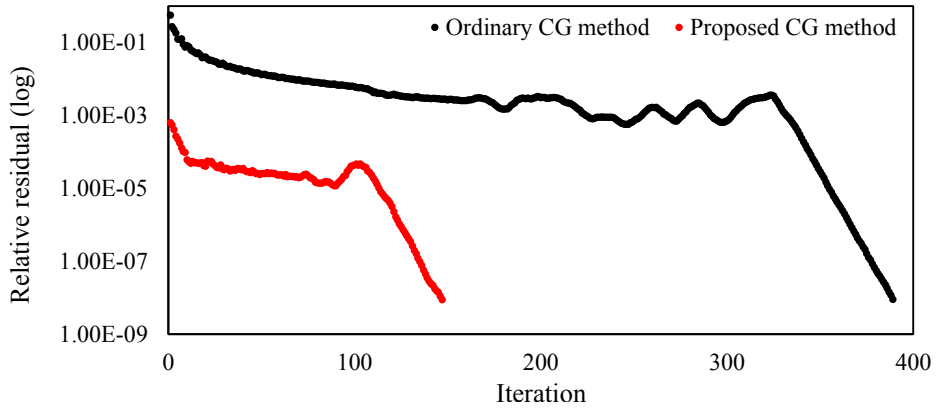

Figure 4.7: Relative residual in each iteration for both CG methods (cantilever problem).

experiments show the implementations of the meta-modeling based initial guess for the CG method with its advantages.

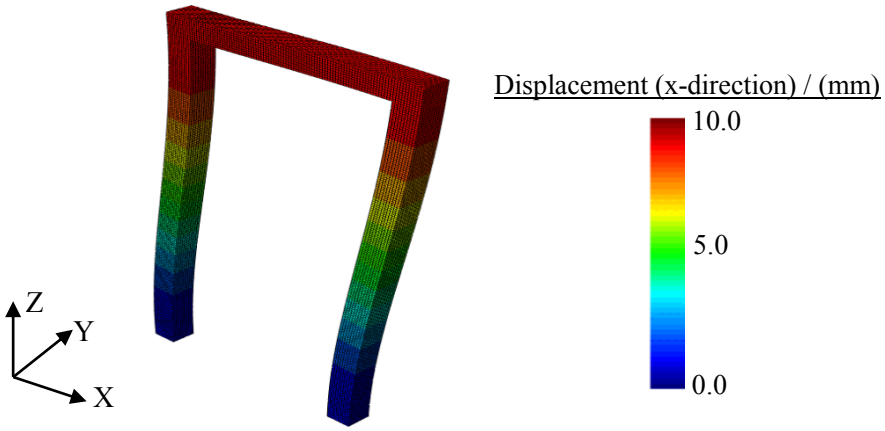

Figure 4.8: Approximated displacement (x-direction) for solid element system from equivalent beam element system (frame problem).

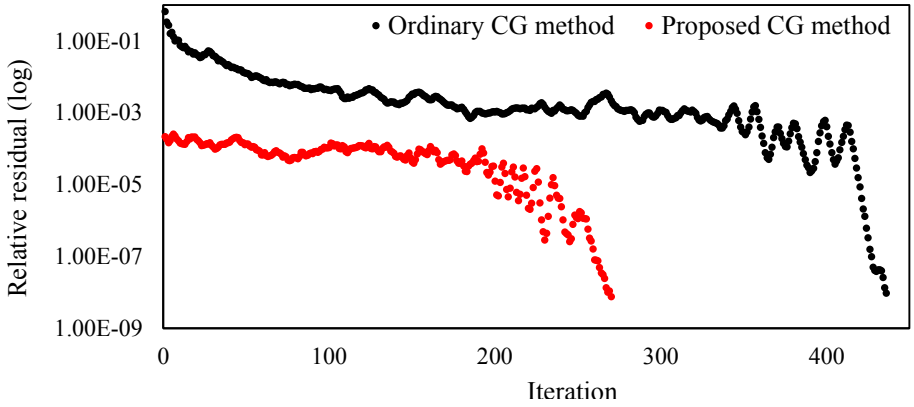

Figure 4.9: Relative residual in each iteration for both CG methods (frame problem).

The frame and cantilever problem with uniform square cross-section are used in these numerical experiments. Figures. 4.1 and 4.5 show the problem settings of these numerical experiments with material data. Only one displacement boundary condition is located at the top left end of frame system; that is 10mm along x direction and the bottom of frame is fully fixed. In the cantilever system, three displacement boundary conditions are located at the right end of cantilever system; these are -5mm, 5mm and -10mm along x, y and z directions respectively and the left end of cantilever beam is fully fixed.

4.2.2.1 Results and discussion

The initial guesses for the target solid element problems which are shown in Figs. 4.1 and 4.5, are constructed from the equivalent beam element systems by minimizing the expression in Eq. (4.1). The converted solid element displacement solutions are shown in Fig. 4.6 and 4.8. Performance of the proposed CG method is compared with the ordinary CG method that uses initial guess as zero vector. It shows that, the proposed CG method is 2.62 and 1.92 times faster than the ordinary CG method for the cantilever and frame problem which includes around 50,000 and 80,000 degrees of freedom (dof) respectively. In this example λ is fixed to 1×10^{-8}. Figures 4.7 and 4.9 show relative residual in each iteration for the both CG methods.

According to this result, it is clear that the amount of iterations drastically reduces in the proposed CG method as compared to the ordinary CG method; see Figs. 4.7 and 4.9.

We hope this positive effect may become larger with a target problem size (dof). If we can create pre-condition from the meta-modeling theory, it is more effective than the meta-modeling based initial guess. Currently, we are working on developing the meta-modeling based pre-condition for the CG method; see Chapter 5.

4.3 Automated construction of consistent lumped mass model for road network

It is excessively difficult to create a manual modeling for a large scale numerical simulations, because of huge number of structure and components. Automated construction process [14] is introduced to overcome this laborious work in this section. The quality of an analysis model that is produced by the automated model construction must be examined. In general, there is a trade-off relation between the accuracy and the complexity of the model. A more complicated model produces a more accurate estimate, but it ought to be difficult to examine the quality of all model components. In developing automated model construction, we have to pay full attention to this trade-off relation.

The author proposes a methodology of automated construction which accounts for the model quality. The key point of the proposed methodology is to construct a set of consistent models for one structure. The consistent model means that the model is used to solve the same problem of the target structure response, by using different mathematical approximations; the fidelity of the model becomes higher as less approximations are made. Suitable mathematical approximations are made, so that approximate solutions of different accuracy are obtained for each of the consistent models. The model quality is more easily examined for a simpler consistent model. Comparing the analysis results with the simpler model, the quality of which is examined, we are able to examine the quality of a more complicated model. By repeating this comparison, we will realize the quality check of a most complicated model of a target structure.

This numerical experiment is aimed at developing an automated model construction for a consistent lumped mass model (CLMM), which is the fundamental model for the seismic response analysis. The lumped mass model is the simplest as it consists of only two parameters as explained in the preceding section [42, 43]. A road network, which consists of numerous bridges, is chosen as a target structure in this experiment.

4.3.1 Decoding of GIS data

The following two types of GIS data are used for automated modeling: 1) 2D GIS data that include 2D polygon data about road network configurations; and 2) 3D GIS data of ground surface elevation. Information about how polygons are connected to form a structure is not included in the 2D GIS data. Thus, the 3D GIS data and the attribute tables in the 2D GIS data are used to guess the connection of neighboring polygons, so that the configuration of a structure is identified.

A decoding program is developed for each of these GIS data. It creates a separate file which includes a set of connected polygons for a particular segment of a road network. The segment is specified according to class information of the road network; there are four main classes as shown in Table 4.5. Figure 4.10 presents a typical example of the segment that is created by the decoding classes. Light green and yellow in Fig. 4.10 represents the whole road network and the target part of the network, respectively. As is seen, there are

no flaws in the segment. Detailed manual inspection is made to examine this segment by comparing it with photos provided by Google Earth.

The decoded GIS data need to be interpreted in order to construct an analysis model. As an example, the interpretation of the configuration and elevation of the center line of the road network is presented. First, the plane configuration of the line is interpreted by using the 2D GIS data, as follows:

I. Convert vector data of polygons to raster data.
II. Apply thinning to identify the center line [53].
III. Prune line segments shorter than 10m.
IV. Separate line segments at each junction, removing complexity at junctions.

Next, the elevation of the center line is estimated by using the difference between the profile and the terrain data that are stored in the 3D GIS data. Noises of estimated elevation data are removed.

In Fig. 4.11, we present an example of the decoding procedures explained above. The target is a segment of a highway road network, the most part of which is bridges, though the tunnel sub-class is excluded; see Fig. 4.11(a). The ramp part of the segment, the configuration of which changes in a short distance, is removed due to the poor resolution of the profile elevation data which are available for this area; see Fig. 4.11(b).

4.3.2 Parameter estimation

This task needed for the automated construction of the lumped mass model is the automated computation of M and K by using Eq. (3.15) and (3.16), inputting the decoded and interpreted data of the target structure; for instance, M_d is computed from the volume calculation of the solid CAD model of the deck. The CLMM is automatically constructed for the first segment of the road network which includes 14 piers; see Fig. 4.11(c) and Fig. 4.12. That is, the values of M and K are computed in the both transverse and longitudinal directions of each pier. Symmetrical geometry of the pier, as shown in Fig. 3.4, provides identical values of M and K for the both directions. The computed values of M and K for the selected segment are presented in Fig. 4.13(a) and (b), respectively.

The detailed procedures of computing the values of M and K are itemized as follows:

I. The interval of piers is fixed as 20 m along the center line due to lack of pier location information in GIS data that is used; see Fig. 4.12 for the frame and solid CAD models of this segment.
II. A steel girder bridge deck is used to estimate the mass of deck for this experiment.
III. Fix connection is used for the connection between the deck and the pier, to satisfy the posed boundary conditions.

The material properties used are summarized in Table 3.2. The total mass of the deck in each span is lumped to the fix connected frame in both the longitudinal and transverse directions, so that the segment is analyzed individually or fully ignoring coupling with neighboring segments.

4.3.3 Response analysis

In view of the quality check results of CLMM, we presume that automated lumped mass models have similar quality. We thus proceed to make a seismic response analysis of the highway road, as shown in Fig. 4.11(c), using all the models. Linear elastic seismic response is computed in the both longitudinal and transverse directions for selected segments of the highway road; see Fig. 4.12. A set of ground motions is used; these ground motion data are selected from K-NET [54] database by considering following criteria:

I. the location of earthquake epicenter that lay between longitude $135^{o} \sim 145^{o}$ and latitude $30^{o} \sim 40^{o}$,
II. the depth of epicenter from surface that less than 60km,
III. the magnitude of earthquake that more than 5.0 and
IV. the earthquakes occurred since 1996 till now.

There are 616 surface ground motion records that fulfill the above requirements. The peak accelerations of selected ground motion records in the NS and EW directions are presented in Fig. 4.14(a) and (b), respectively; the three highest peak accelerations that belong to the 80^{th}, 208^{th} and 91^{st} ground motion records among the selected 616 ground motions are highlighted in red, blue and green, respectively, in these figures.

Both the NS and EW components of each record are input to the highway segment separately, and the seismic responses are calculated around 1,200 times for each lumped mass model of the pier. The maximum drift ratio of the pier is used as an index of the seismic response [55, 56] and they are plotted in Fig. 4.15(a) and (b) for the longitudinal and transverse directions, respectively. The highlighted results in Figs. 4.15(a) and (b) show the drift ratio computed for the three ground motions highlighted in Fig. 4.14(a) and (b). As for these highlighted results, there is no any unexpected change or intuitively unexpected behavior. We emphasize that smooth variation of the results is well understood, due to the nature of the linear analysis as well as the smooth variation of the input parameters of the piers, which are shown in Fig. 4.13(a) and (b). While this is a necessary condition, this result of no intuitively unexpected behavior suggests that the automatically constructed lumped mass model is good enough to be used for the seismic response analysis of the bridge piers.

The automated model construction will be extended to a larger part of the road network. Actually, it would be a straightforward task, since the programs of decoding and interpreting the GIS data and constructing a lumped mass model are already developed; the decoding and interpretation programs need to be improved, in order to be applied to segments of a more complicated configuration, such as a ramp. The methodology of the automated model construction can be extended from the simplest lumped mass model to a more sophisticated model according to the meta-modeling theory; an eventual goal is a full solid element model for non-linear finite element analysis.

Table 4.5: Main and sub classes of road network.

Main class	Sub class
Highway National road General road Main local road	Tunnel Intersection Surface

(a)

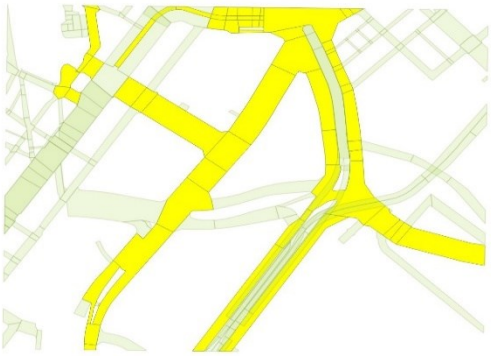

(b)

(c)

Figure 4.10: Example of decoding of GIS data to identify road network configuration: (a) extraction of general road; (b) extraction of main local road; and (c) extraction of highway.

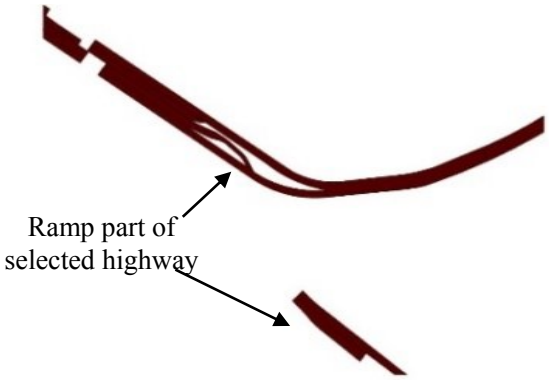

(a)

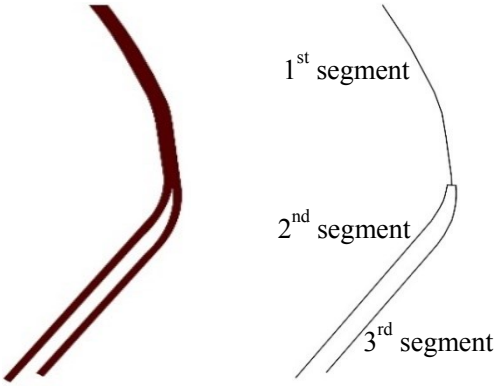

(b) (c)

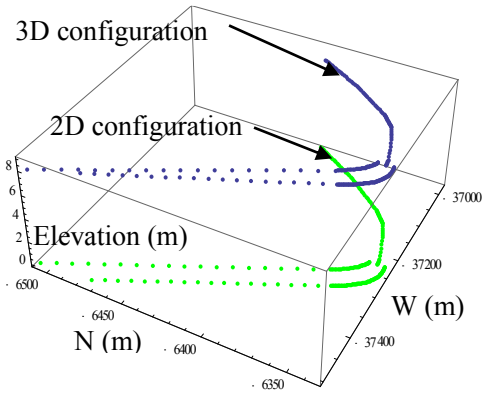

(d)

Figure 4.11: Example of applying decoding procedures to GIS data: (a) exclusion of highway main-class tunnel sub-class; (b) exclusion of highway main-class tunnel and ramp part; (c) extraction of 2D centreline arrangement; and (d) arrangement of 3D centreline.

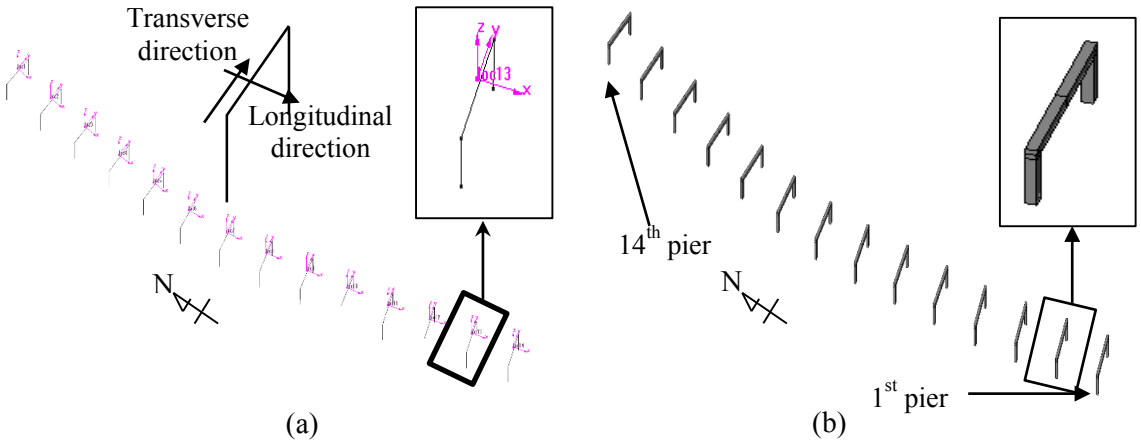

Figure 4.12: CAD model for selected highway segment: (a) frame CAD model; and (b) solid CAD model.

4.4 Implementation of CMSM for bridge structure

4.4.1 Single-span simple bridge structure

4.4.1.1 Problem setting

A CMSM model is constructed for a single span bridge structure, and it is exposed to time history analysis. Ground motion is input in the longitudinal direction of the bridge, and the response in the same direction is computed. Input ground motion for this example is shown in Fig. 3.9 which is rich in low frequency. The deck structure of this bridge acts as rigid body in both the longitudinal and transverse directions of the bridge due to provided boundary conditions for it. Two mass points of the CMSM are located along the pier axis; see Fig. 4.16. Table 4.6 shows material properties of both pier and deck structures. Linear isotropic elasticity is assumed.

First, the solid element model is constructed to obtain the first two dynamic modes in the longitudinal direction. In Fig. 4.17, the mode shapes, $\boldsymbol{\psi}^1$ and $\boldsymbol{\psi}^2$, are displayed. Next, the CMSM parameters are estimated by using the computed first two dynamic modes in the longitudinal direction of the bridge. The results are summarized in Tables 4.7 and 4.8. Finally, time history analysis is conducted for the both solid element model and CMSM to obtain the deck structure displacement response and the resulting shear force at the pier base by inputting the target ground motion in the longitudinal direction of the bridge. The base shear force of the CMSM is estimated by employing Eq. (3.34).

4.4.1.2 Results and discussion

Developed approximate displacement functions of the CMSM, $\boldsymbol{\phi}^1$ and $\boldsymbol{\phi}^2$, are displayed in Fig. 4.18. It is clear that these displacements fulfill the requirement A1 that is discussed in section 3.3. The first two natural frequencies of the CMSM match those of the solid element model, as expected; see Table 4.9.

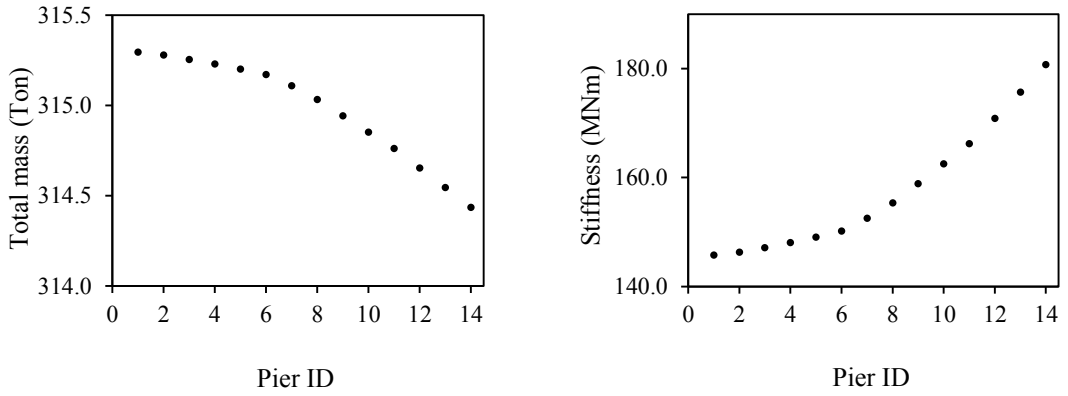

(a) (b)

Figure 4.13: Lumped mass parameters for each pier along both directions: (a) mass (M); and (b) stiffness (K).

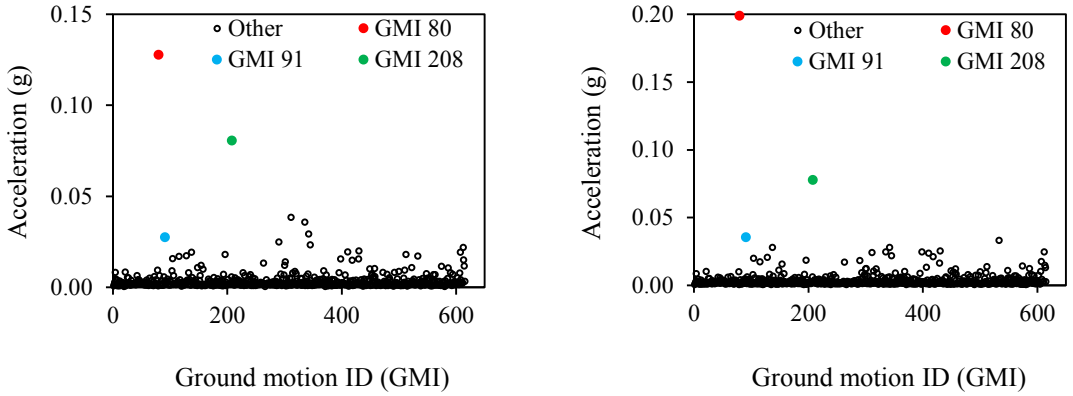

(a) (b)

Figure 4.14: Peak acceleration of selected ground motions: (a) along WE direction; and (b) along NS direction.

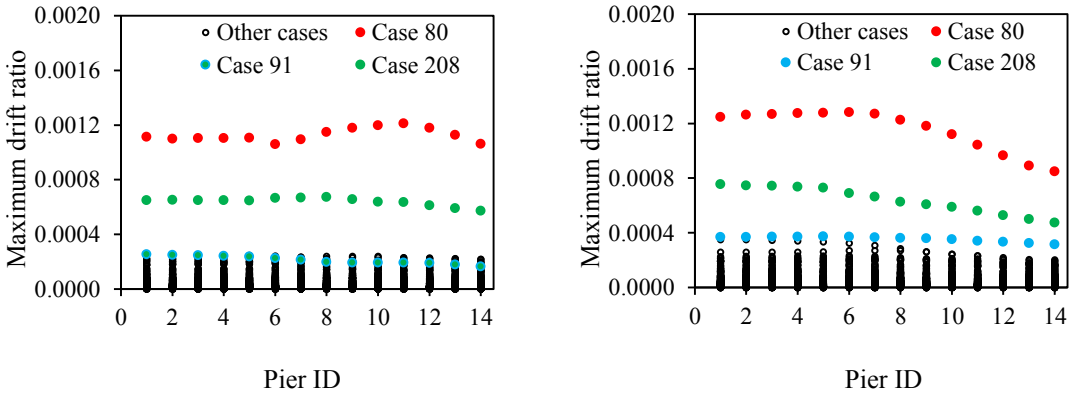

(a) (b)

Figure 4.15: Drift ratio in each pier: (a) along transverse direction; and (b) along longitudinal direction.

The deck displacement in the longitudinal direction of the bridge computed from the solid element model and the displacement of the first mass point of the CMSM are shown in Fig. 4.19 for the time interval selected from the full response. They are in good agreement since input ground motion is rich in the first two natural frequencies. The relative

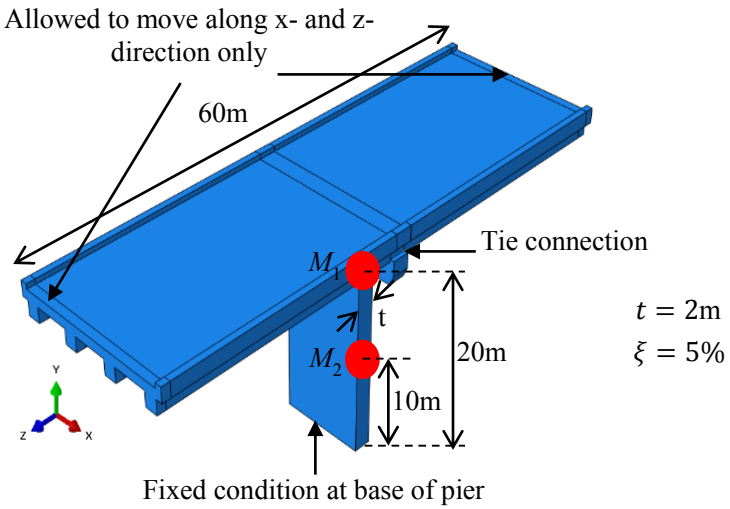

Figure 4.16: Single span simple bridge model for CMSM.

error of the CMSM estimation is around 3.75%. In this case, this simple bridge structure vibrates mainly in the first dynamic mode.

It is clear that a CMSM is able to make accurate estimate of displacement, by identifying major dynamic modes of a target structure subjected to given ground motion; these modes are included into the construction process of the CMSM. According to Eq. (3.34), a displacement field which is computed by the CMSM leads to accurate estimate of the base shear force, as well. As shown in Fig. 4.20, the relative error of estimating the base shear is around 4.92%.

4.4.2 Multi-span continuous bridge structures

4.4.2.1 Problem setting

As a more realistic example, a CMSM is constructed for a multi-span continuous bridge structure. Three structures with different types of pier arrangement are studied; see Fig. 4.21 and Table 4.10. Like the previous case, the longitudinal and transverse directions are considered separately. The CMSM for the transverse direction includes two dynamic modes while that for the longitudinal direction uses only first mode. This is because in the longitudinal direction, the first mode has a much lower natural frequency than other modes.

Tie connection is used for the connection between the pier and the deck in this problem. This is the simplest connection, and more sophisticated connection could be used if more detailed information is available for the connection. A spring of 2 GNm spring constant in the longitudinal direction is attached at the left end of the deck in cases 1 and 2, while no spring is attached at the right end; see Fig. 4.21 where the left and right ends are designated by A and B, respectively.

Table 4.11 shows the material properties of the both pier and deck. Linear isotropic elasticity is assumed. The cross-section of the deck is shown in Fig. 4.22, and the geometrical properties of this cross section are summarized in Table 4.12. Configuration of

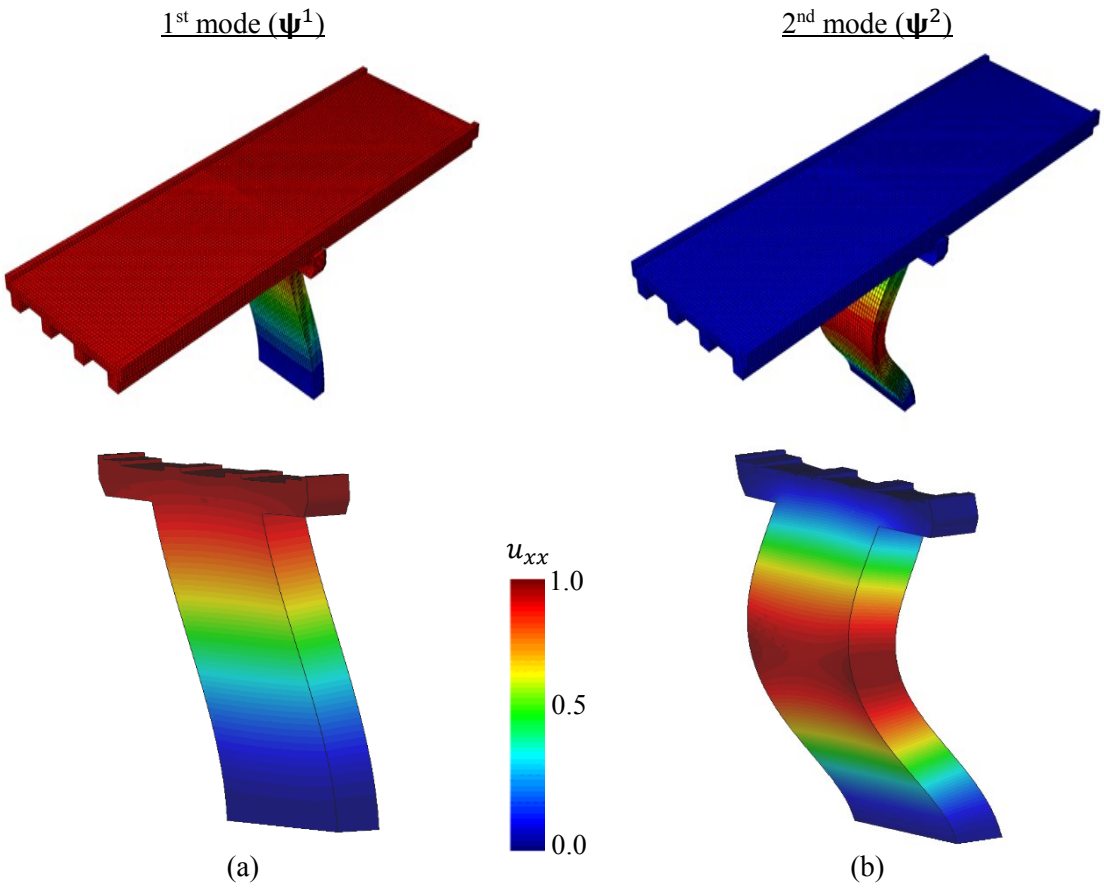

Figure 4.17: First two dynamic modes of single-span simple bridge structure along longitudinal direction of bridge.

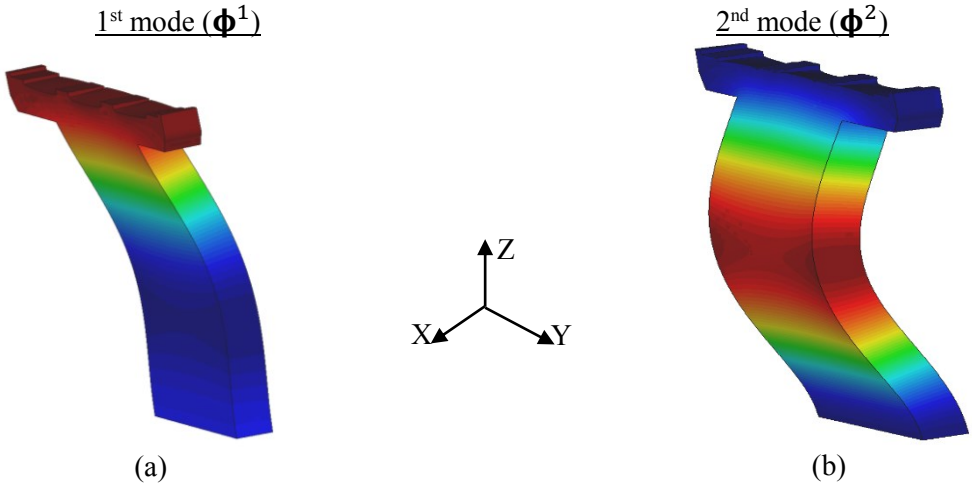

Figure 4.18: Developed approximate displacement modes of single-span simple bridge structure along longitudinal direction of bridge.

an actual pier and approximate pier is displayed in Fig. 4.23. The ground motion displayed in Fig. 3.9 is employed.

First, instead of a solid element model, we construct a simpler frame element model, in order to obtain first two dynamic mode shapes in the transverse direction ($\boldsymbol{\psi}_z^1$ and $\boldsymbol{\psi}_z^2$)

Table 4.6: Material data of single-span simple bridge model.

Item	E / (GPa)	ρ / (Kgm^{-3})	v
Pier	192	2400	0.2
Deck	200	7200	0.3

Table 4.7: CMSM stiffness parameters for single-span simple bridge structure.

Stiffness parameter	Value / (GNm)
K_1	11.750
K_2	9.514
K_3	-3.974

Table 4.8: CMSM mass parameters for single-span simple bridge structure.

Mass parameter	Value / (ton)
M_1	14465.321
M_2	-191.797
M_{12}	494.655

Table 4.9: Natural frequency of single-span simple bridge structure along longitudinal direction.

Model type	1st mode / (Hz)	2nd mode / (Hz)
Lumped mass	1.502	33.004
Solid	1.503	33.001

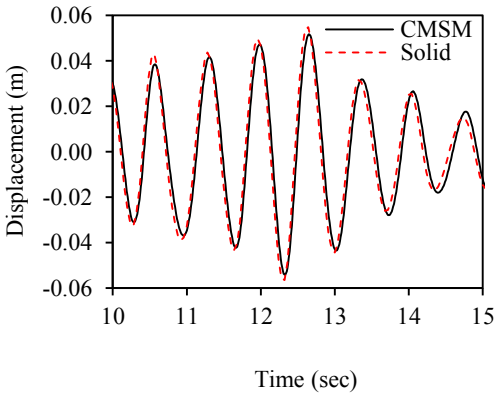

Figure 4.19: Displacement of single-span simple bridge deck (M_1) along x-direction.

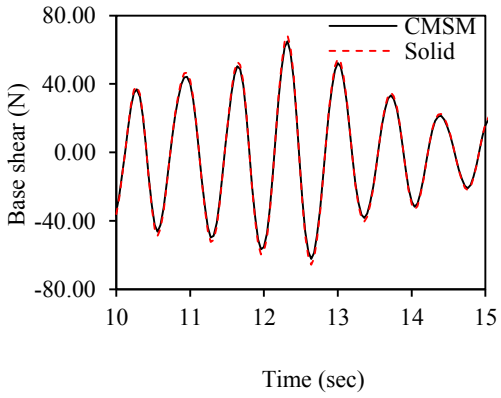

Figure 4.20: Base shear of single-span simple bridge pier base along x-direction.

and first dynamic mode shape in the longitudinal direction ($\boldsymbol{\psi}_x^1$); see Fig. 4.24(a) for $\boldsymbol{\psi}_z^1$ and $\boldsymbol{\psi}_z^2$ of case 1. Approximate displacement functions ($\boldsymbol{\phi}_z^1$ and $\boldsymbol{\phi}_z^2$) of case 1 for the transverse direction are shown in Fig. 4.24(b). Second, we determine locations of mass points along the deck axis, considering target locations of response output from the model; see Fig. 4.21. Third, CMSM parameters are computed from the dynamic mode shapes and the mass points' locations.

4.4.2.2 Results and discussion

Natural frequencies of the CMSM's in the longitudinal and transverse directions are presented in Tables 4.13 and 4.14, respectively; the natural frequencies of the original frame element models are presented, too. As is seen, the natural frequencies of the CMSMs coincide with those of the frame element models.

Time series of displacement responses of the CMSM is compared with that of the original frame element model; see Figs. 4.25(a) and (b) for case 1. It is seen that the response of the CMSM matches well with that of the frame element model. Relative errors of the maximum displacement in the longitudinal and transverse directions of the CMSM are presented in Tables 4.15 and 4.16, respectively. As is seen, the maximum relative error in all the cases is 2.637%.

Next, shear force and bending moment at the base of the fourth pier (P4) are estimated; see Fig. 4.21 for the location of P4. Equations (3.32) and (3.33) are used to estimate base shear, $\mathbf{F}$, and the bending moment $\mathbf{M}$ that acts on the base P4 ($\mathbf{x} = \mathbf{0}$) respectively. In Figs. 4.26 and 4.27, respectively, $\mathbf{F}$ and $\mathbf{M}$ are presented for the longitudinal and transverse directions. Relative errors of the maximum resultant force are summarized in Tables 4.17 and 4.18. As is seen, the maximum relative error in all the cases is 4.514%, and it is clear that the CMSM can be used to approximately estimate structural seismic responses.

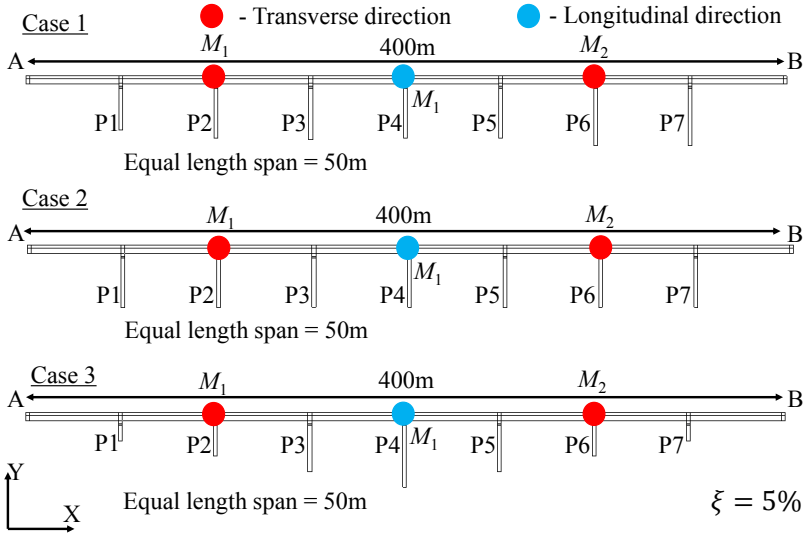

Figure 4.21: Geometric and mass points' information about multi-span bridge models.

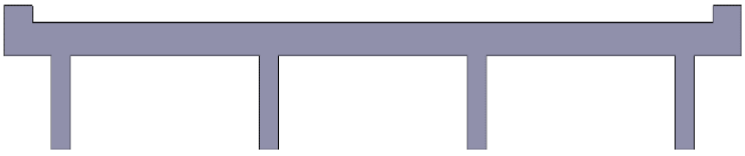

Figure 4.22: Cross-section of bridge deck in multi-span bridge models.

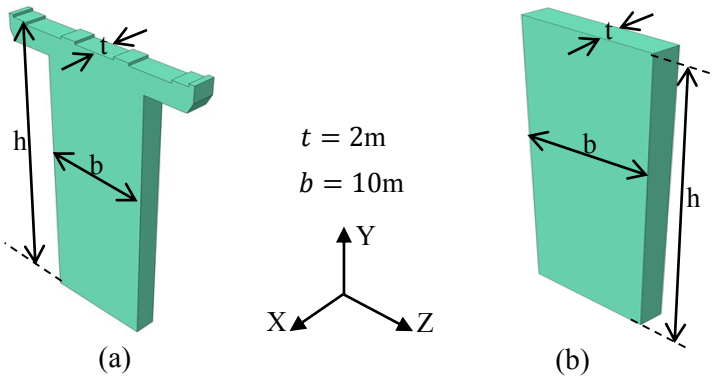

Figure 4.23 Pier structure: (a) actual geometry; and (b) approximate geometry for beam model of multi-span bridge models.

Table 4.10: Pier height data of multi-span bridge models.

Pier ID	Height / (m)		
	Case 1	Case 2	Case 3
1	22	25	8
2	26.3	25	16
3	27.1	25	24
4	26.3	25	32
5	26.1	25	24
6	30.2	25	16
7	30.1	25	8

Table 4.11: Material data of multi-span bridge models.

Item	E / (GPa)	ρ/ (Kgm^{-3})	v
Pier	24	2400	0.2
Deck	200	3000	0.3

Table 4.12: Beam properties of uniform deck part in multi-span bridge models.

Beam parameter	Value
Area	25.850 m^2
I_{zz}	22.009 m^4
I_{yy}	895.726 m^4
I_{xy}	0.000 m^4
J	7.393 m^4

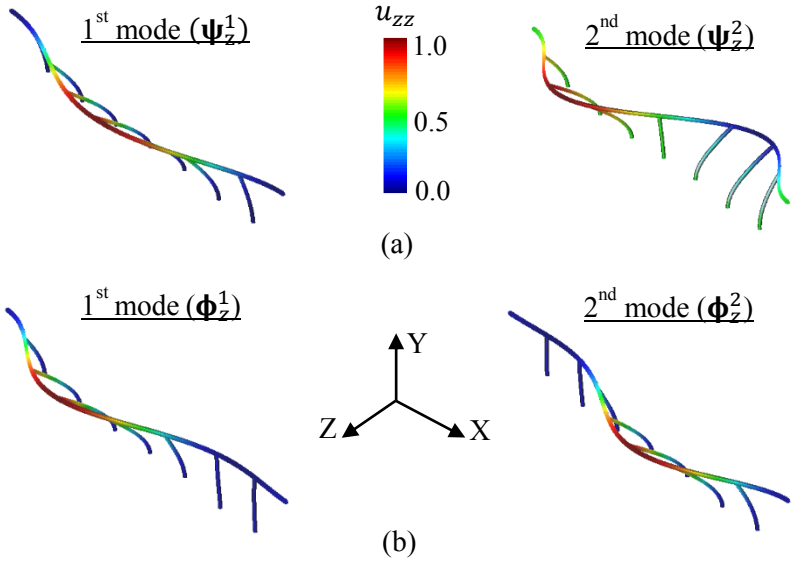

Figure 4.24: Multi-span bridge model along transverse direction of bridge (case 1): (a) first two dynamic modes; and (b) developed approximate displacement modes.

Table 4.13: Natural frequency of multi-span bridge models along longitudinal direction of bridge.

Case	Mode ID	Frequency / (Hz)	
		Frame	CMSM
1	1	1.345	1.345
2	1	1.377	1.377
3	1	1.836	1.836

Table 4.14: Natural frequency of multi-span bridge models along transverse direction of bridge.

Case	Mode ID	Frequency / (Hz)	
		Frame	CMSM
1	1	1.938	1.938
	2	3.112	3.111
2	1	2.066	2.068
	2	3.182	3.183
3	1	2.317	2.317
	2	3.713	3.715

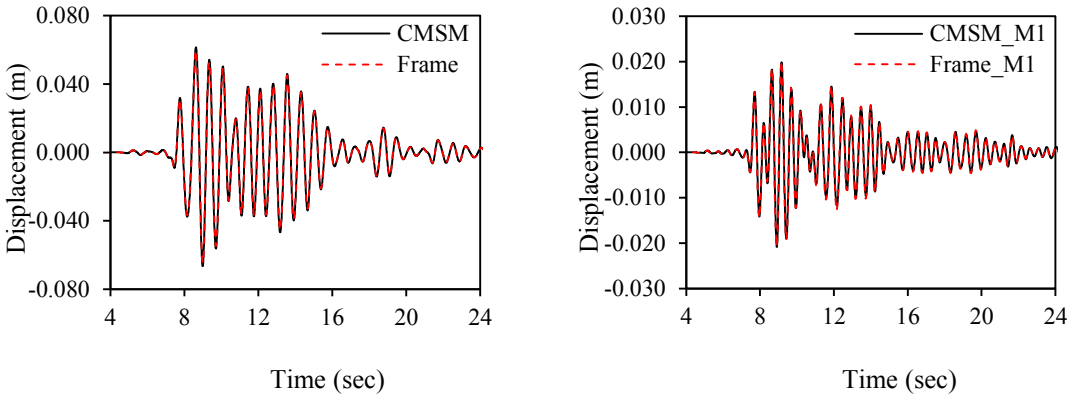

(a) (b)

Figure 4.25: Displacement results of multi-span bridge model in case 1: (a) CMSM model of longitudinal direction at M_1 point; and (b) CMSM model of transverse direction at M_1 mass point.

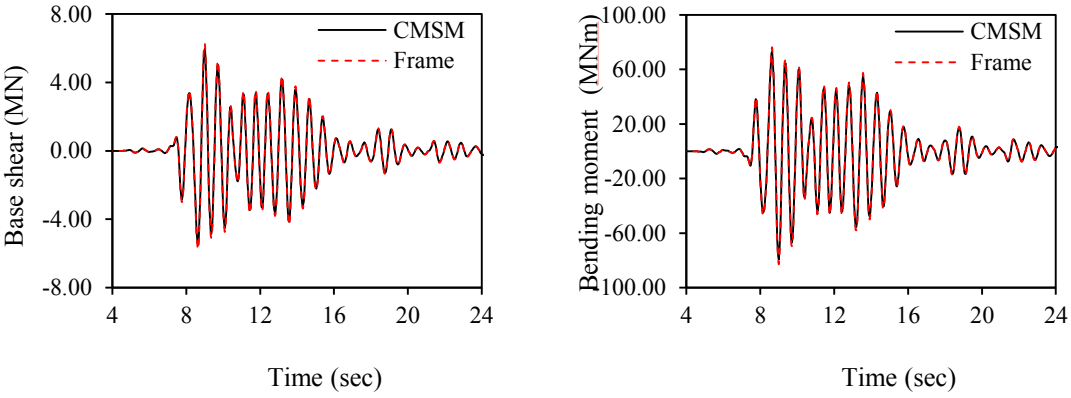

(a) (b)

Figure 4.26: Resultant force of multi-span bridge model at base of P4 in case 1 (CMSM model of longitudinal direction): (a) base shear along x-direction; and (b) bending moment about z-axis.

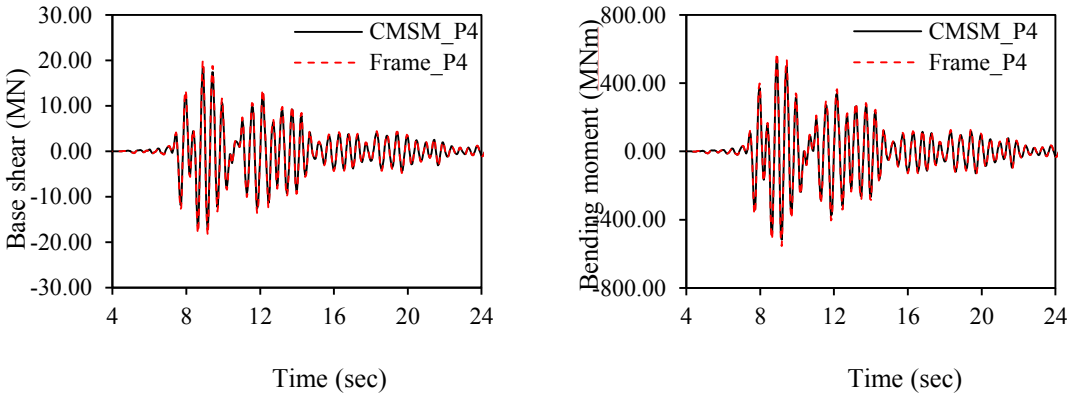

(a) (b)

Figure 4.27: Resultant force of multi-span bridge model at base of P4 in case 1 (CMSM model of transverse direction): (a) base shear along z-direction; and (b) bending moment about x-axis.

Table 4.15: Relative error for maximum displacement between frame and CMSM model along longitudinal direction (CMSM model for longitudinal direction).

Case	Location	Error / (%)
1	M_1	2.067
2	M_1	2.015
3	M_1	0.930

Table 4.16: Relative error for maximum displacement between frame and CMSM model along transverse direction (CMSM model for transverse direction).

Case	Location	Error / (%)
1	M_1	0.191
	M_2	1.667
2	M_1	2.227
	M_2	2.227
3	M_1	2.637
	M_2	2.637

Table 4.17: Relative error for maximum resulting force at base of P4 between frame and CMSM model along longitudinal direction (CMSM model for longitudinal direction).

Case	Force type	Error / (%)
1	Shear	3.634
	BM	3.523
2	Shear	3.886
	BM	3.541
3	Shear	4.322
	BM	3.832

Table 4.18: Relative error for maximum resulting force at base of P4 between frame and CMSM model along transverse direction (CMSM model for transverse direction).

Case	Force type	Error / (%)
1	Shear	4.514
	BM	4.231
2	Shear	3.995
	BM	3.537
3	Shear	3.895
	BM	3.324

(BM – Bending moment)

4.5 Implementation of meta-modeling based consistent models for quality assurance of automated high fidelity bridge structure

4.5.1 Set of multi-span bridge structures

4.5.1.1 Problem setting

Three straight (SC) and three curved (CC) multi-span bridge structures with different types of pier arrangement are studied in this numerical experiment for the quality assurance of the automated model; see Fig 4.28 and Tables 4.20 and 4.21 for the geometric arrangement of these bridge structures. The continuous deck structures of target bridges are only allowed to move in the longitudinal direction of the bridge, the piers are fixed to the ground at the pier base, and tie connection is used for the connection between the pier and the deck. Tie connection is the simplest, and more sophisticated connection could be used if more detailed information is available for the connection.

Four consistent models are developed for each bridge structure. They are (1) a CLMM, (2) a CMSM, (3) a frame model, and (4) a solid element model. First, the automated construction module is used to develop a solid element model and a frame models separately; see Appendix E for the automated construction processes. Then, a CLMM is constructed from the frame model; see Sec. 3.2 for the construction of CLMM. The deck structures of the target bridges are not considered as a rigid body, when responses in the transverse direction is studied, due to the pre-posed boundary conditions for the deck structure. Hence, a CLMM is constructed only for the responses in the longitudinal direction. Next, a CMSM is constructed from the solid element model. Unlike the CLMM, the CMSM is constructed for both the longitudinal and transverse directions; see Sec. 4.3 and Figs. 4.30 and 4.31 for construction of CMSM.

Table 4.19 shows the material properties of the pier and the deck structures. Linearly isotropic elasticity is assumed. The configuration of the pier is displayed in Fig. 4.29(a), and the cross-section of the deck is shown in Fig. 4.21(b). Frequency and time domain analyses are conducted for the target bridge structures, in order to check the consistency of the developed models and the applicability of the consistent low fidelity model for quality assurance process of the automated solid element model. The ground motion displayed in Fig. 3.9 is employed.

4.5.1.2 Results and discussion

Natural frequencies of the CLMM's in the longitudinal direction are presented in Table 4.22; the natural frequencies of the first mode of the frame models are presented, too. As is seen, the natural frequencies of the CLMM's do not have a good agreement with those of the frame models, except for the cases of SC_1 and SC_2. This is due to the contribution of stiffness from the deck structure to the first mode in the longitudinal direction; in the current CLMM, the deck structure is assumed to be a rigid body. Figure 4.32 shows the axial strain distribution in the first mode in the longitudinal direction for SC_2 and CC_3. These two models are, respectively, the best and the worst, in comparison of the frequency with that of the frame models. It is clear that the deck structure of CC_3 generates more axial strain than that of SC_2, which induces stiffer responses for the first mode in the longitudinal direction. When the target structure becomes complicated such as case CC_3, the current CLMM cannot perform well; we need to improve it in the future by considering a deformable deck structure.

Natural frequencies of the CMSM's in the transverse and longitudinal directions are presented in Tables 4.23 and 4.25, respectively; the natural frequencies of the original solid element models are presented, too. As is seen, the natural frequencies of the CMSM's coincide with those of the solid element models, as expected.

First three natural frequencies of the frame model and the solid element model in the transverse and longitudinal directions are presented in Tables 4.24 and 4.26, respectively. It is seen that there is good agreement of the natural frequencies in the longitudinal direction but less agreement is observed for the natural frequency in the transverse direction. Figures 4.33 and 4.34 show the distribution of normal strain component in the longitudinal direction (or axial strain) along the deck axis, for the first three modes of the solid element model in the longitudinal and transverse directions, respectively. In this study, the axial strain distribution of the modes in the longitudinal direction is similar to that of the frame model that is based on the beam theory; the distribution is nearly parallel to the cross-section of the deck along the deck structure axis; see Fig. 4.33. It is clearly seen in Fig. 4.34 that the axial strain distribution of the modes in the transverse direction cannot be well obtained by using the frame model and that plate or shell element models should be used so that strain distribution in both longitudinal and transverse directions is captured.

Based on the above observation, we conduct time history analyses only for the longitudinal direction of each bridge structure. Responses of the CLMM's, CMSM's and frame models are compared with those of the solid element model; see Figs. 4.35 and 4.36 for the case of SC_2 and CC_3, respectively. It is seen that the responses of the CMSM and frame model matches well with those of the solid element model, but that the response of CLMM's does not match well except the case of SC_2. Figures 4.37(a) and (b) show input ground motion in the frequency domain and the natural frequency of each model of the case of SC_2 and CC_3 are designated. The natural frequency of the CLMM of CC_3 shifts to the peak amplitude range of the input ground motion, which causes a larger difference in displacement response; see Figs. 4.36(c) and 4.37(b). The natural frequencies of all the modes of the case of SC_2, which is the simplest bridge structure, coincide with each other; see Fig. 4.37(a). Relative errors of the maximum displacement in the longitudinal direction of the each model are presented in Table 4.27. As is seen, the maximum error is 16.049% for CLMM's of the case of CC_3.

We need to choose a suitable consistent model of low fidelity for the quality assurance of a model of higher fidelity (solid element model) that is constructed in an automated manner. The model of low fidelity is used as a reference, in examining the response of the target structure of complex configuration. In this study, a pair of a CMSM and a frame model are for such quality assurance of the automated solid element model for all the six bridge structures; the responses in the longitudinal direction are used.

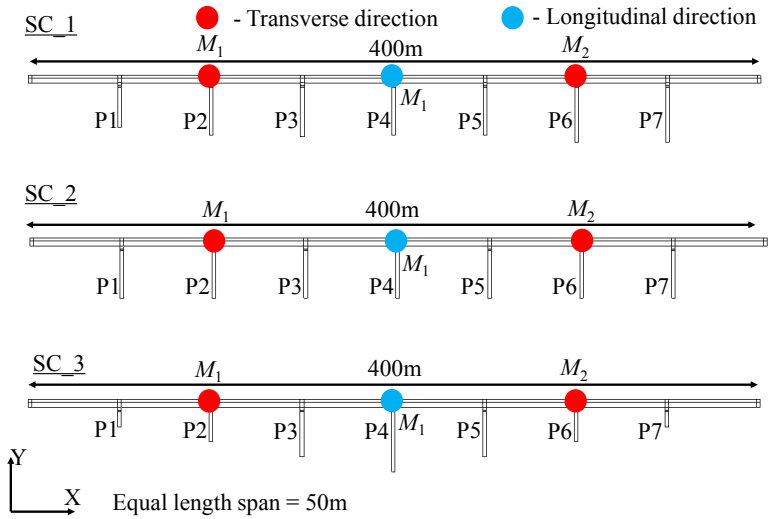

(a)

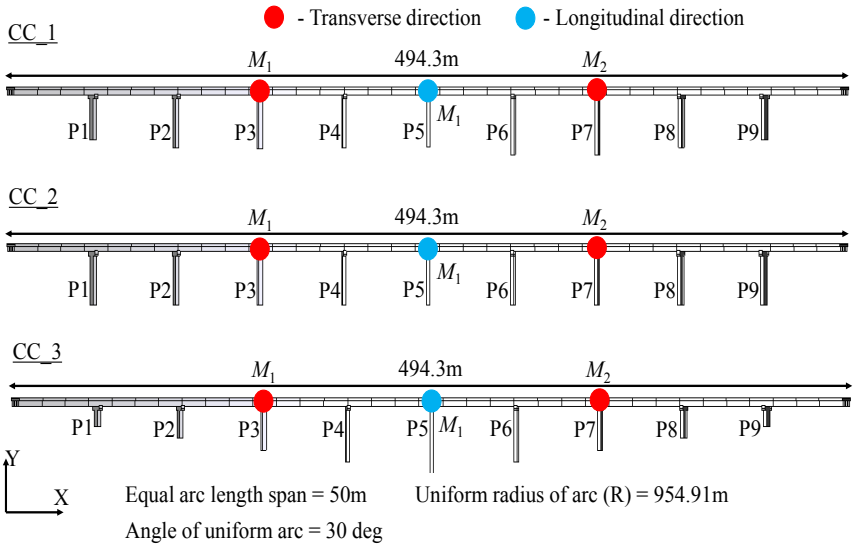

(b)

Figure 4.28: Geometric and mass points' information about multi-span bridge structures: (a) straight continuous (SC); and (b) curved continuous (CC).

Table 4.19: Material data of multi-span bridge structures (SC & CC).

Item	E / GPa	ρ / Kgm^{-3}	ν
Pier	24	2400	0.2
Deck	200	2000	0.3

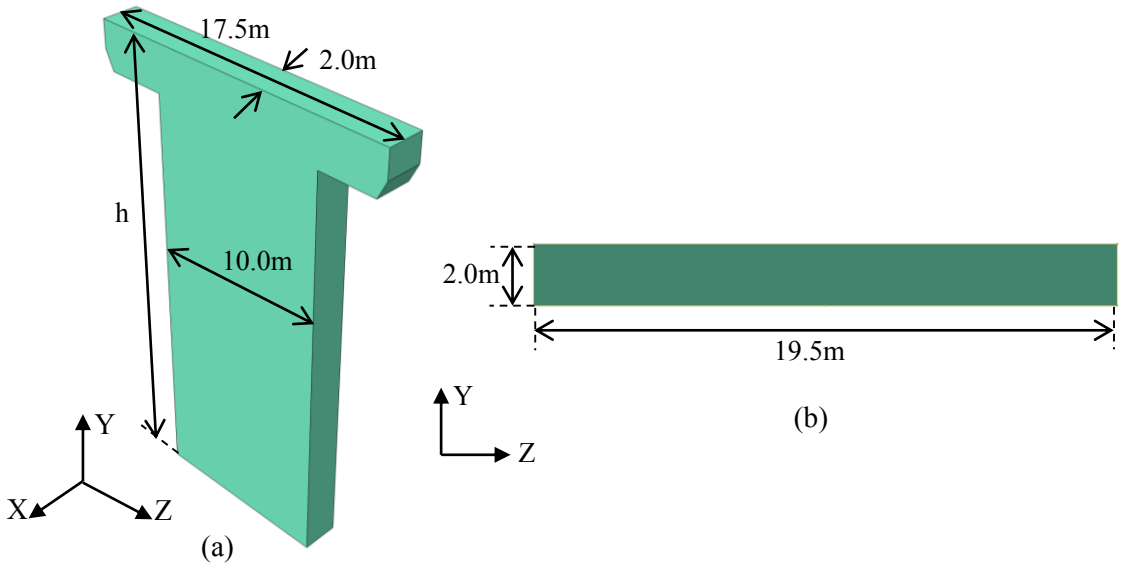

Figure 4.29: Multi-span bridge models (SC & CC): (a) pier geometry; and (b) deck cross-section geometry.

Table 4.20: Pier height data of straight bridge models (SC).

Pier ID	Height / m		
	SC_1	SC_2	SC_3
1	22.0	25.0	8.0
2	26.3	25.0	16.0
3	27.1	25.0	24.0
4	26.3	25.0	32.0
5	26.1	25.0	24.0
6	30.2	25.0	16.0
7	30.1	25.0	8.0

Table 4.21: Pier height data of curved bridge models (CC).

Pier ID	Height / m		
	CC_1	CC_2	CC_3
1	22	25.0	8.0
2	26.3	25.0	14.0
3	27.1	25.0	20.0
4	26.3	25.0	26.0
5	26.1	25.0	32.0
6	30.2	25.0	26.0
7	30.1	25.0	20.0
8	26.3	25.0	14.0
9	22.0	25.0	8.0

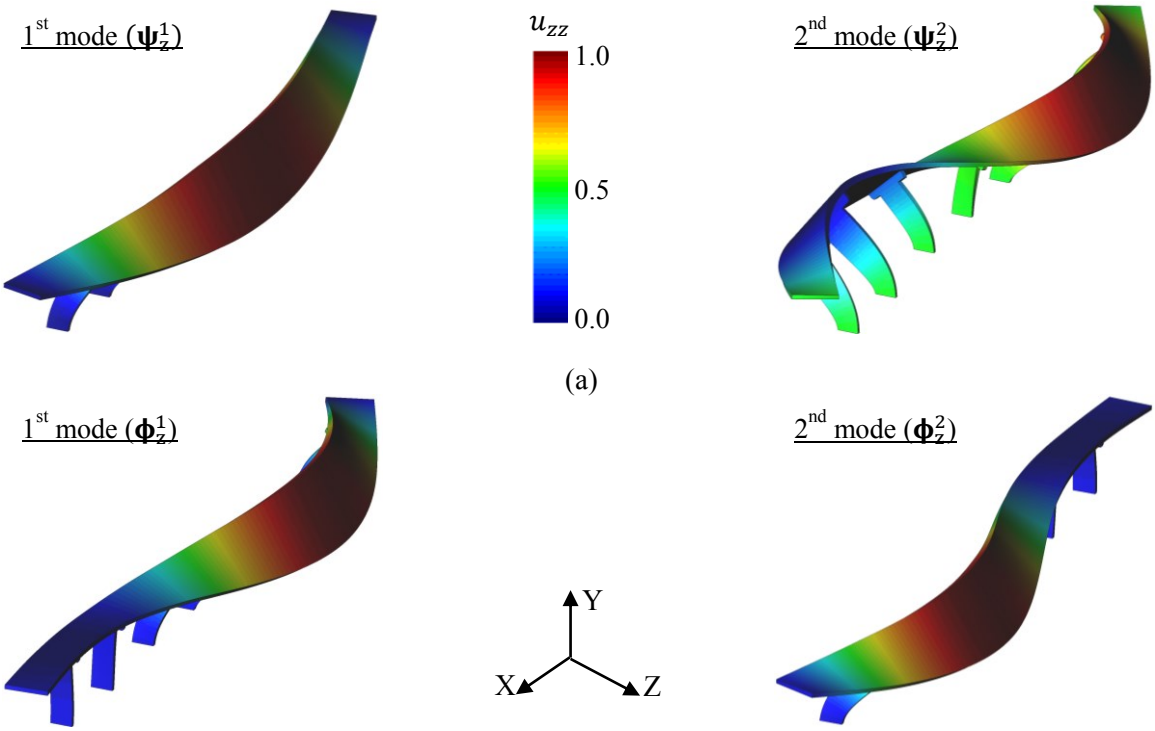

Figure 4.30: Solid bridge model along transverse direction of bridge (SC_1): (a) first two dynamic modes; and (b) developed approximate displacement modes.

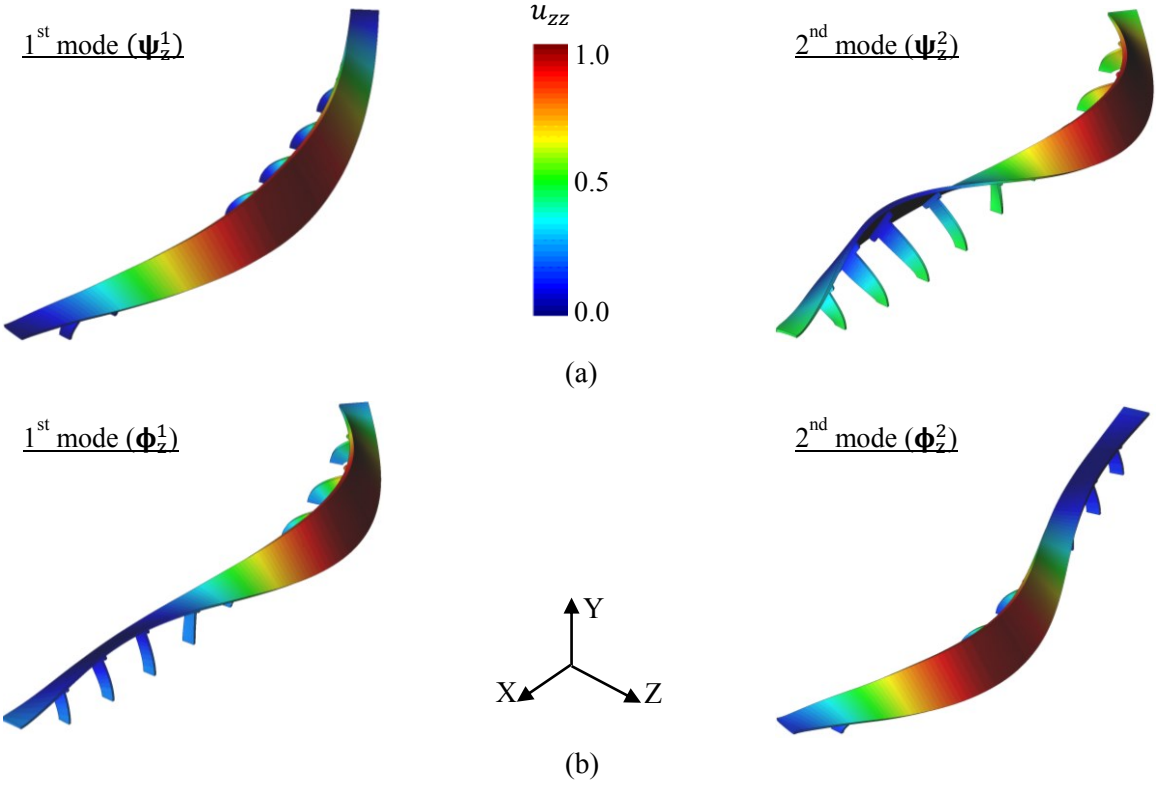

Figure 4.31: Solid bridge model along transverse direction of bridge (CC_1): (a) first two dynamic modes; and (b) developed approximate displacement modes.

Table 4.22: Natural frequency of multi-span bridge structure (CLMM and frame element models) along longitudinal direction.

Case ID	Frequency / (Hz)		Difference / (%)
	CLMM	Frame (1st mode)	
SC_1	0.614	0.623	1.444
SC_2	0.665	0.673	1.189
SC_3	1.504	1.620	7.160
CC_1	0.628	0.690	8.985
CC_2	0.656	0.711	7.735
CC_3	1.398	1.610	13.167

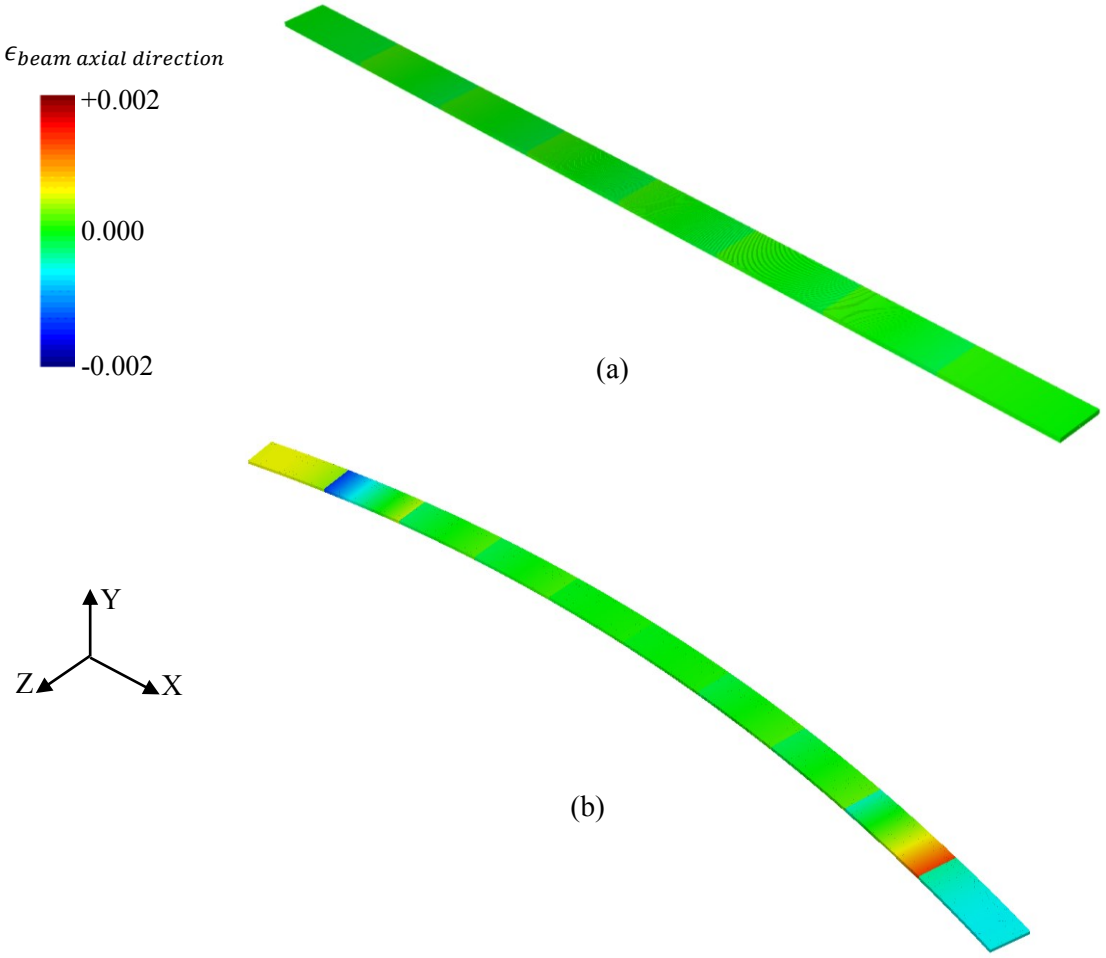

Figure 4.32: Axial strain contours plot of deck structure (frame element model) for first mode along longitudinal direction of bridge: (a) SC_2; and (b) CC_3.

Table 4.23: Natural frequency of multi-span bridge structure (CMSM and solid element models) along transverse direction.

Case ID	Frequency / (Hz)				Difference / (%)	
	CMSM		Solid			
	1st mode	2nd mode	1st mode	2nd mode	1st mode	2nd mode
SC_1	1.625	2.610	1.624	2.610	0.062	0.000
SC_2	1.752	2.703	1.752	2.702	0.000	0.037
SC_3	2.191	3.882	2.190	3.881	0.046	0.026
CC_1	1.541	2.152	1.540	2.151	0.065	0.046
CC_2	1.692	2.254	1.692	2.253	0.000	0.044
CC_3	1.894	3.131	1.893	3.130	0.053	0.032

Table 4.24: Natural frequency of multi-span bridge structure (frame and solid element models) along transverse direction.

Case ID	Mode ID	Frequency / (Hz)		Difference / (%)
		Frame	Solid	
SC_1	1	1.989	1.624	22.475
	2	3.540	2.610	35.632
	3	6.193	4.835	28.087
SC_2	1	2.103	1.752	20.051
	2	3.625	2.702	34.160
	3	6.231	4.873	27.868
SC_3	1	2.326	2.190	6.210
	2	4.339	3.881	11.801
	3	6.814	5.936	14.785
CC_1	1	1.710	1.540	11.039
	2	2.611	2.151	21.385
	3	4.310	3.514	22.652
CC_2	1	1.884	1.692	11.348
	2	2.732	2.253	21.261
	3	4.349	3.526	23.341
CC_3	1	1.999	1.893	5.599
	2	3.370	3.130	7.668
	3	5.064	4.571	10.785

Table 4.25: Natural frequency of multi-span bridge structure (CMSM and solid element models) along longitudinal direction.

Case ID	Frequency / (Hz)		Difference / (%)
	CMSM	Solid (1st mode)	
SC_1	0.630	0.630	0.000
SC_2	0.680	0.680	0.000
SC_3	1.640	1.640	0.000
CC_1	0.713	0.712	0.140
CC_2	0.730	0.730	0.000
CC_3	1.624	1.623	0.062

Table 4.26: Natural frequency of multi-span bridge structure (frame and solid element models) along longitudinal direction.

Case ID	Mode ID	Frequency / (Hz)		Difference / (%)
		Frame	Solid	
SC_1	1	0.623	0.630	1.111
	2	3.691	3.750	1.573
	3	3.810	3.880	1.804
SC_2	1	0.673	0.680	1.029
	2	3.717	3.785	1.796
	3	3.828	3.902	1.896
SC_3	1	1.620	1.640	1.220
	2	3.789	3.884	2.446
	3	3.985	4.088	2.520
CC_1	1	0.690	0.712	3.090
	2	3.720	3.699	0.568
	3	3.826	3.896	1.797
CC_2	1	0.711	0.730	2.602
	2	3.736	3.734	0.054
	3	3.837	3.907	1.792
CC_3	1	1.610	1.623	0.801
	2	3.783	3.752	0.826
	3	3.950	4.056	2.613

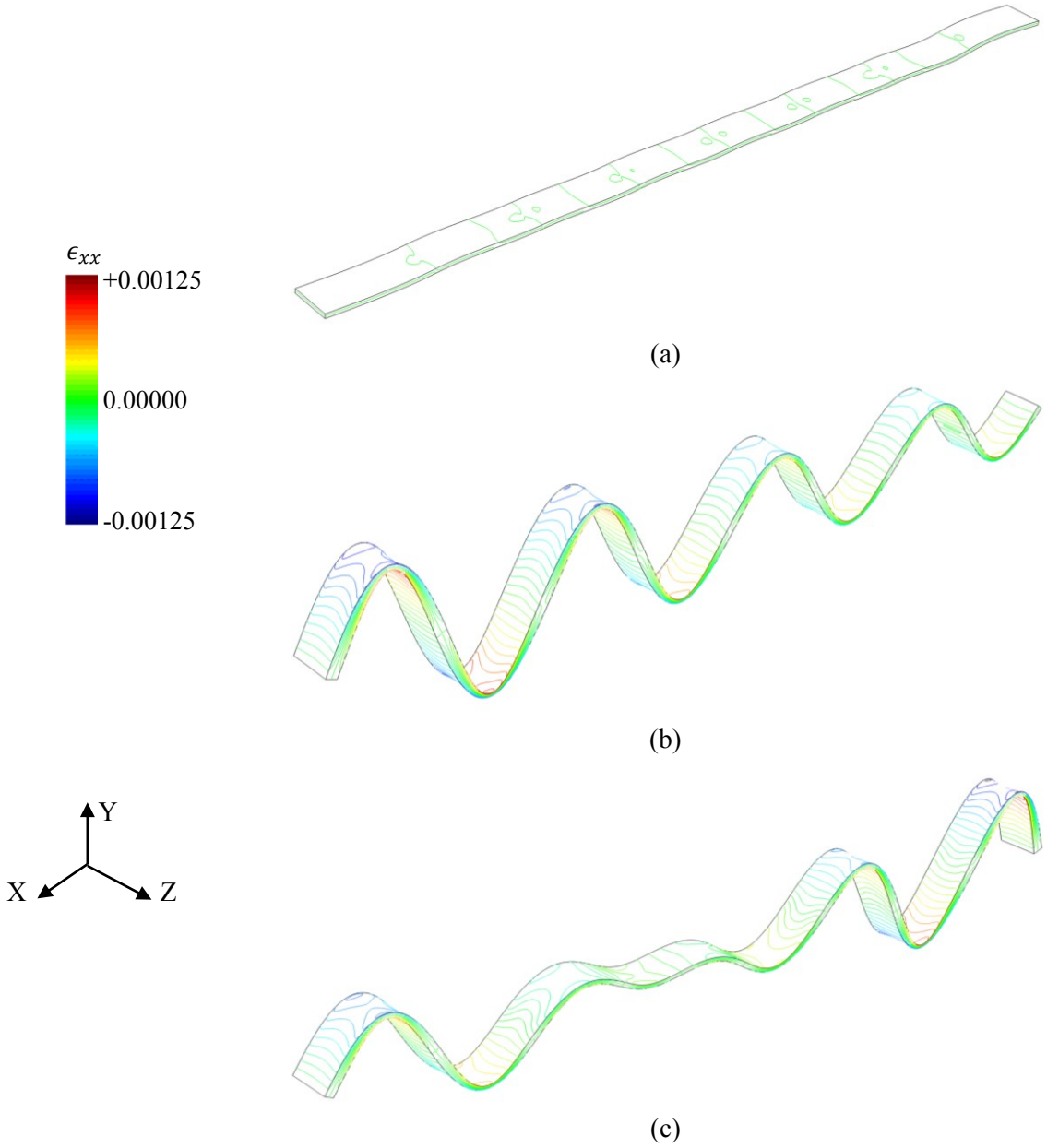

Figure 4.33: Strain contours plot of solid element deck structure along x-direction for longitudinal direction mode shapes (SC_1): (a) 1st mode shape; (b) 2nd mode shape; and (c) 3rd mode shape.

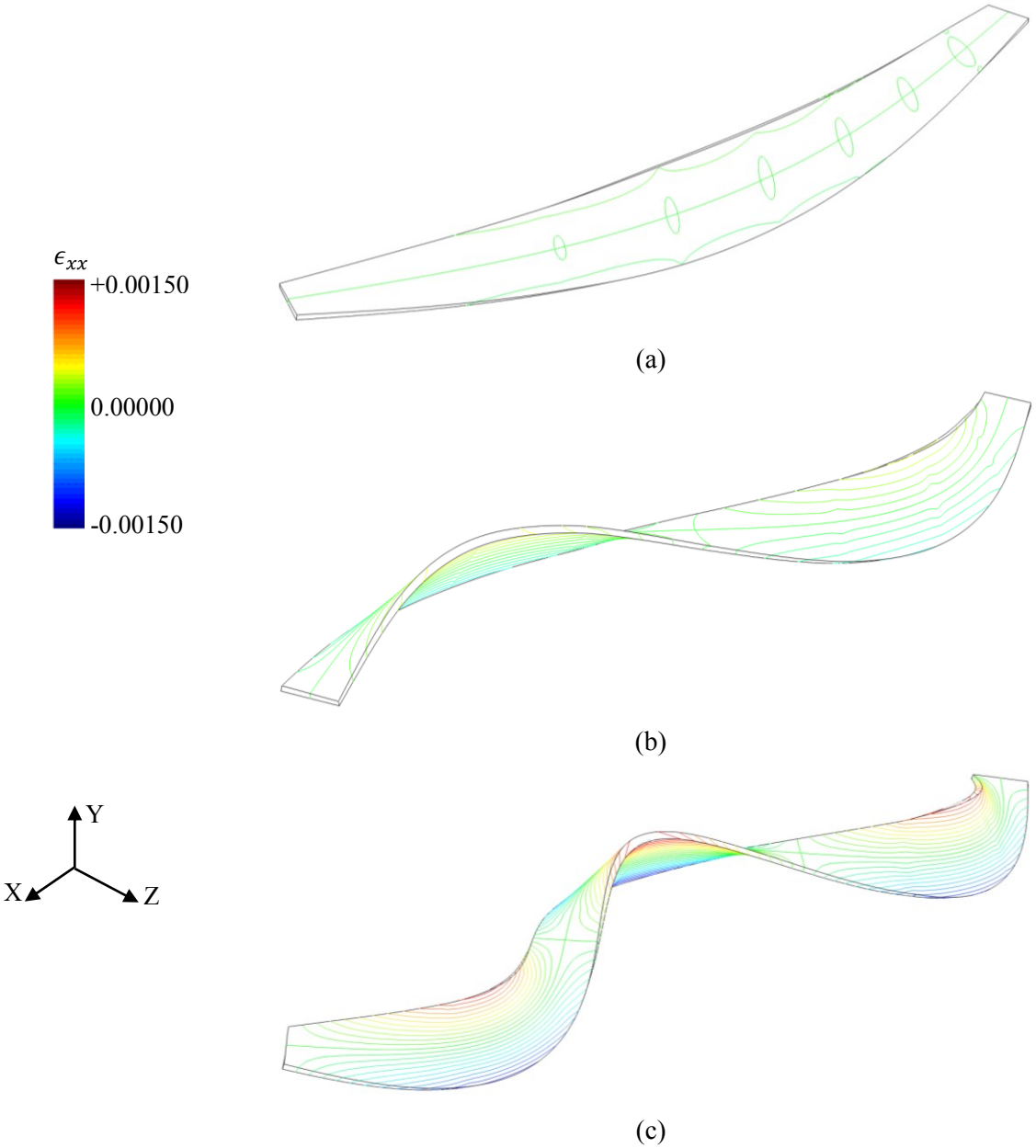

Figure 4.34: Strain contours plot of solid element deck structure along x-direction for transverse direction mode shapes (SC_1): (a) 1st mode shape; (b) 2nd mode shape; and (c) 3rd mode shape.

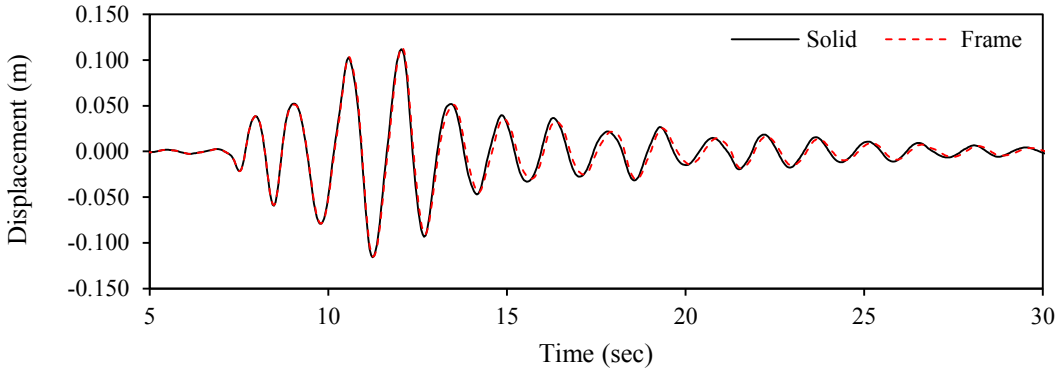

(a)

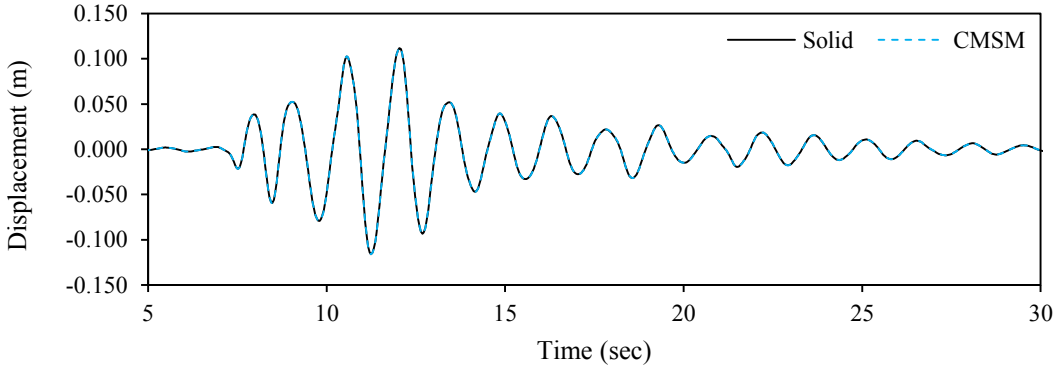

(b)

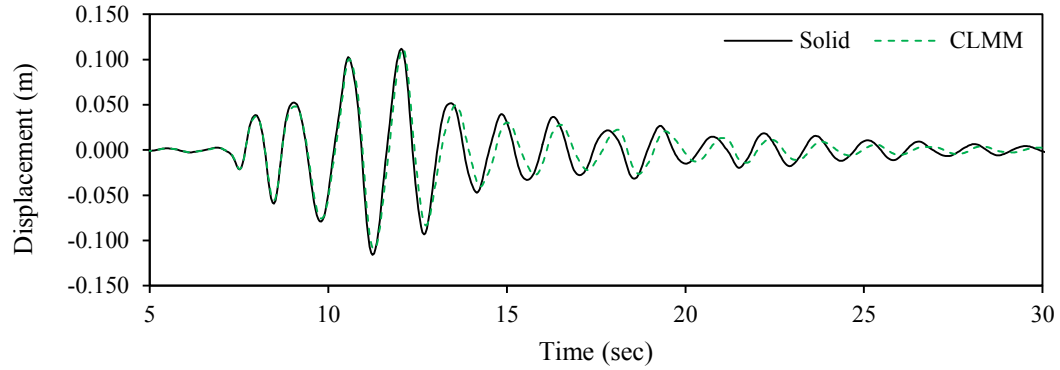

(c)

Figure 4.35: Displacement results of deck structure (SC_2): (a) solid and frame element models; (b) solid element model and CMSM; and (c) solid element model and CLMM.

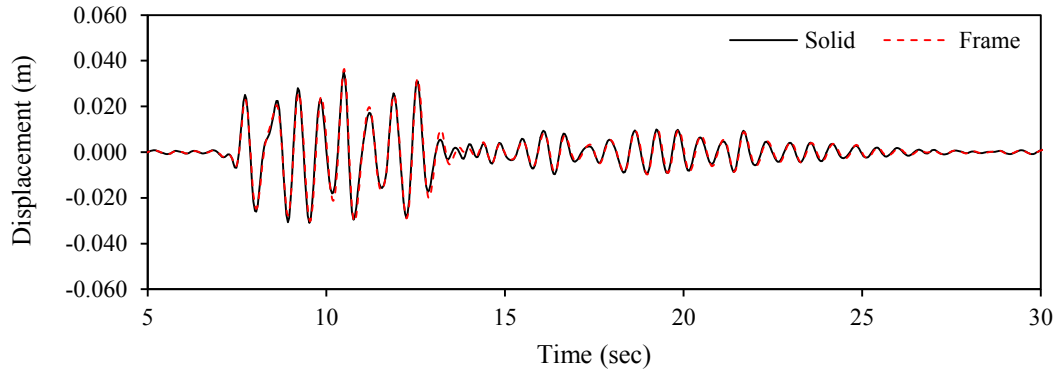

(a)

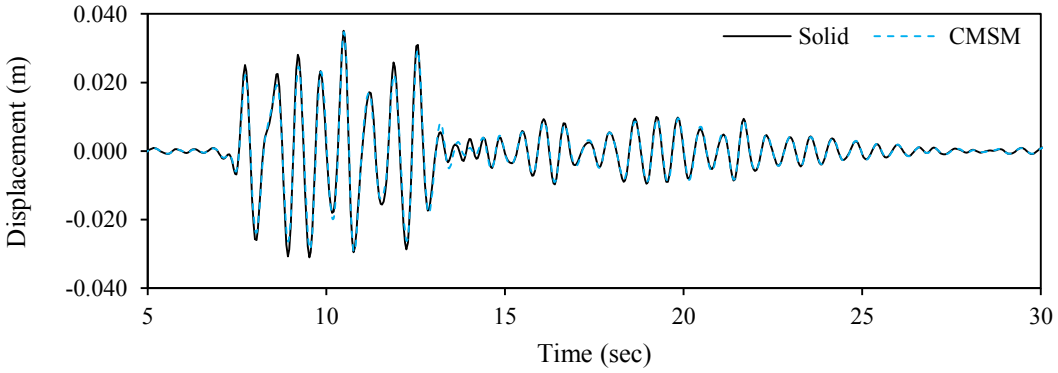

(b)

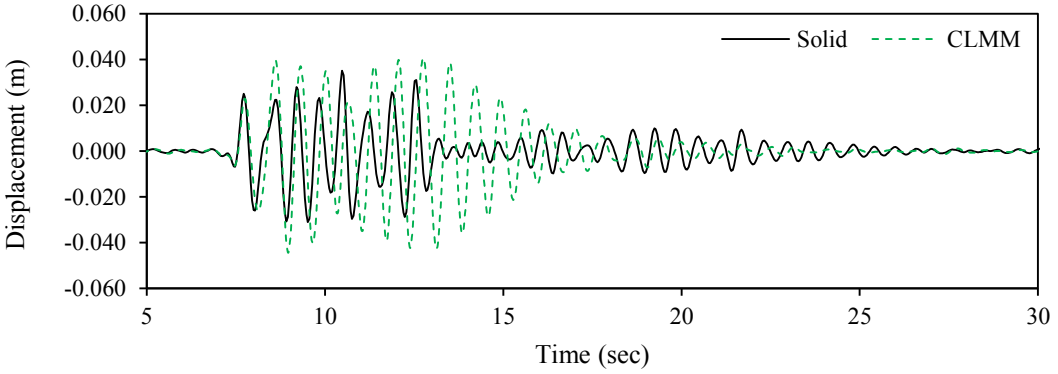

(c)

Figure 4.36: Displacement results of deck structure (CC_3): (a) solid and frame element models; (b) solid element model and CMSM; and (c) solid element model and CLMM.

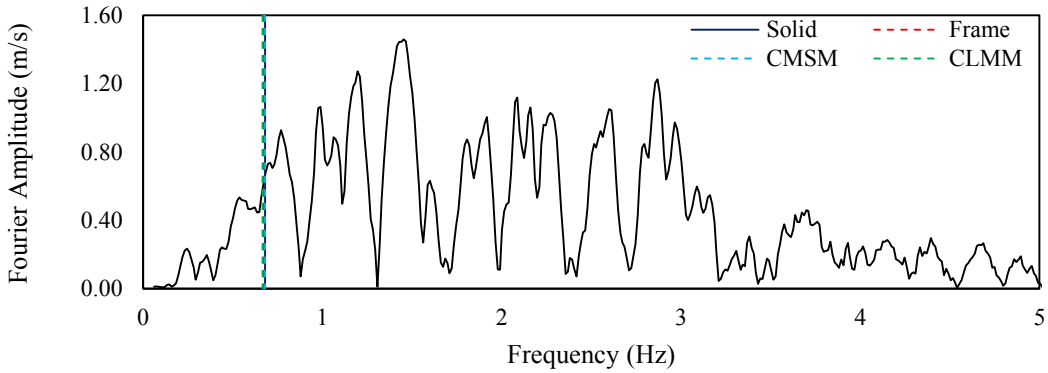

(a)

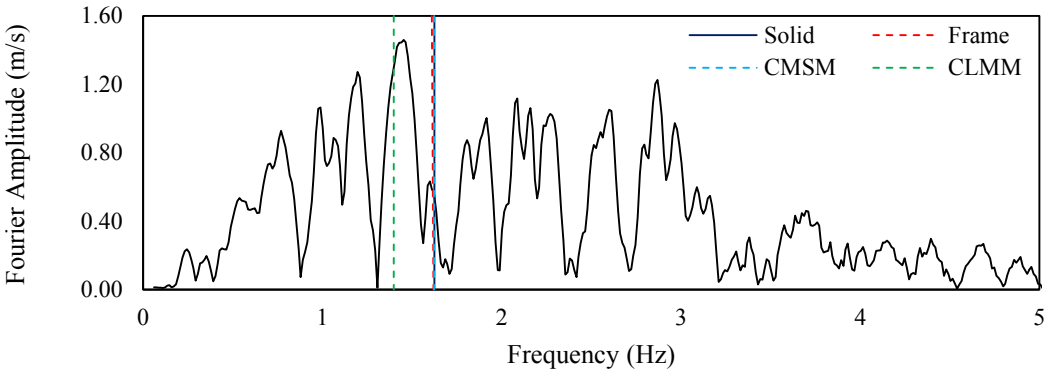

(b)

Figure 4.37: Input ground motion in frequency domain with natural frequencies of solid element model (1st mode along longitudinal direction of bridge), frame element model (1st mode along longitudinal direction of bridge), CMSM and CLMM: (a) SC_2; and (b) CC_3.

Table 4.27: Relative difference for maximum displacement between solid and other models along longitudinal direction.

Case ID	Difference / (%)		
	CLMM	CMSM	Frame
SC_1	5.945	1.027	1.708
SC_2	0.204	1.145	1.792
SC_3	14.797	1.403	4.234
CC_1	5.059	2.230	4.365
CC_2	4.457	1.313	2.770
CC_3	16.049	1.953	3.875

4.5.2 Part of freeway bridge structure in Tokyo metropolitan

4.5.2.1 Problem setting

A junction part which is selected from a freeway road network in the Tokyo metropolitan area is used for the quality assurance of a solid element model that is constructed in an automated manner; see Fig 4.38 for the selected part. A frame model consisting of beam elements is also constructed in an automated manner. The solid element model and the frame model, which are described in CAD format, are shown in Fig. 4.39; see Appendix E for the automated construction process. Figure 4.40 presents the selected junction part for frequency analysis; the solid element model is shown in Fig. 4.40(a), the frame model with the cross-section information, Fig 4.40(b), and the FEM frame element model, Fig. 4.40(c).

Tie connection is used for the connection between the pier and the deck in this problem. This is the simplest connection; a more sophisticated connection could be used if more detailed information is available for the connection. Fixed conditions are assigned at the base of each pier and free conditions are used at the both ends of the deck structure. Table 4.19 shows the material properties of the both pier and deck structures. Linearly isotropic elasticity is assumed.

This study is limited to the quality assurance of the automated solid element model due to the complexity of the target structure; the complexity is easily seen in the difference in the elevation of the each part of the deck structure. This study further narrows down by considering only the first mode shape in the longitudinal direction of the junction part, due to plate-like behaviors of the deck structure in the transverse direction and a possibility of surface contact between the parallel deck structure in the both transverse and longitudinal directions except the first mode shape in the longitudinal direction.

4.5.2.2 Results and discussion

Figures 4.41(a) and (b) show the displacement distribution of the frame and solid element models, respectively, for the first mode in the longitudinal direction of the junction part. There is a 14.855% difference in the frequency between the frame model and the solid element model, which cannot be neglected. The reason of this difference is understood in view of Fig. 4.42, which displays the axial displacement component of both the frame model (Fig. 4.42(a)) and the solid element model (Fig. 4.42(b)). The axial displacement distribution is different near the connecting part, due to the inconsistency of the treatment of the connection between the deck structure and the pier for the frame model and the solid element model.

Figure 4.43 shows behavior of the connection between the deck structure and the pier structure for the solid element and frame models. Distributed connection condition (or continuity of displacement and traction across the interface of the connection) is used for the solid element model, while the single point connection condition (or continuity of cross sectional displacement/angle and force/moment) is used for the frame model. The distributed connection condition of the solid element model increases the stiffness of the junction, which induces higher natural frequency than the frame model.

The quality assurance of the automated solid element model for a complicated structure as a freeway junction part is conducted by using the complete consistency that corresponds to the automated frame model. There is an inconsistency issue in the current

automated frame model due to improper treatment of the connection and the boundary condition which need to be addressed in the future. In addition, we have to introduce a more sophisticated structure element, such as plate or shell element, for the automation process in order to resolve the other issue that is related to the mode in the transverse direction.

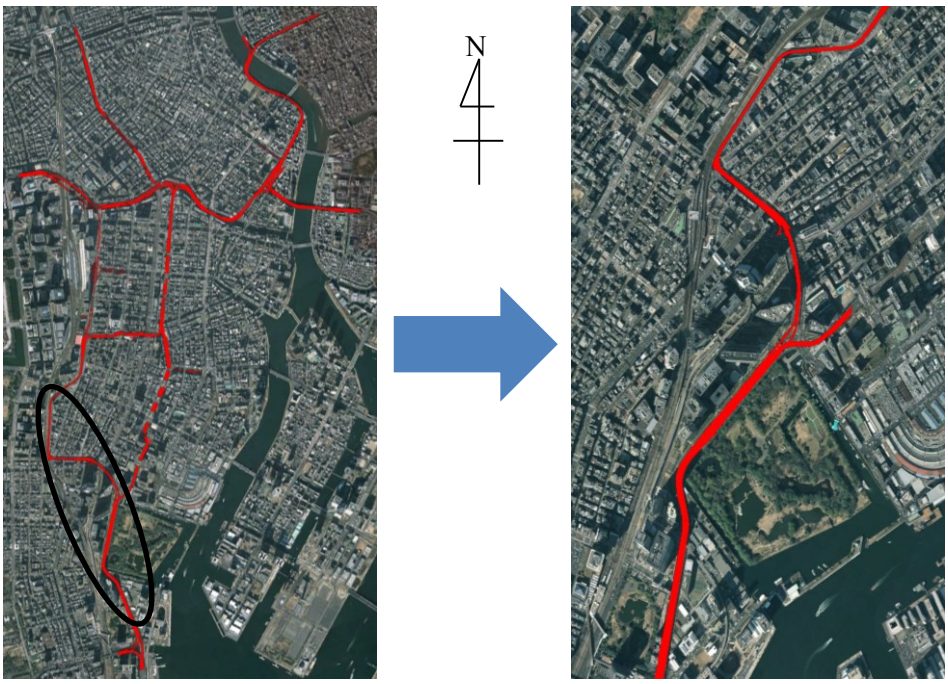

(a) (b)

Figure 4.38: Automated CAD model construction: (a) freeway network near imperial palace in Tokyo (Japan); and (b) selected part for demonstration.

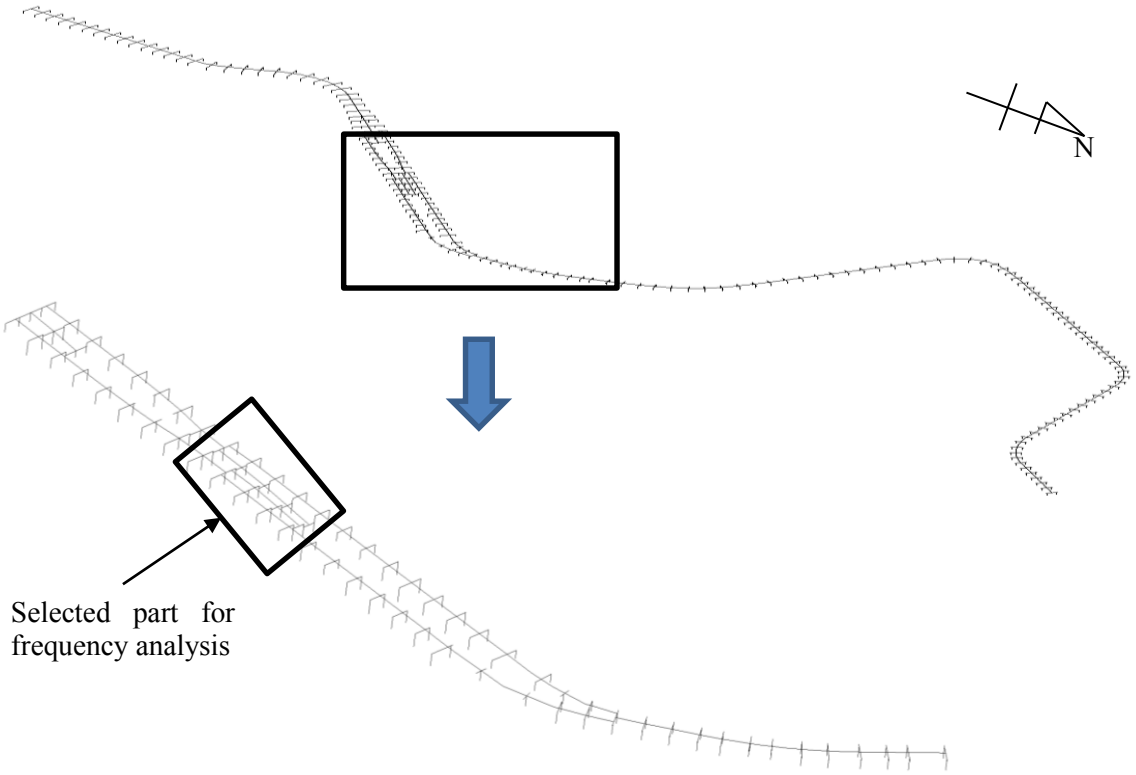

(a)

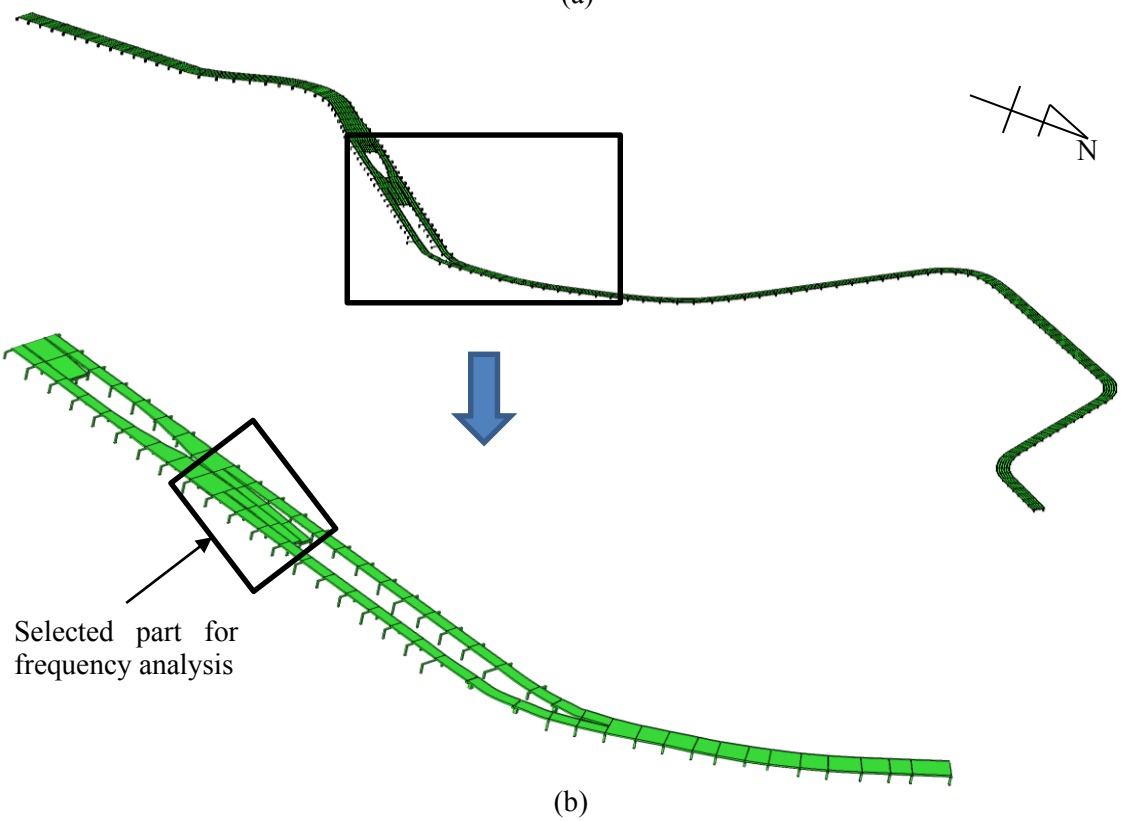

(b)

Figure 4.39: Constructed CAD models for selected freeway part: (a) solid CAD model; and (b) frame CAD model.

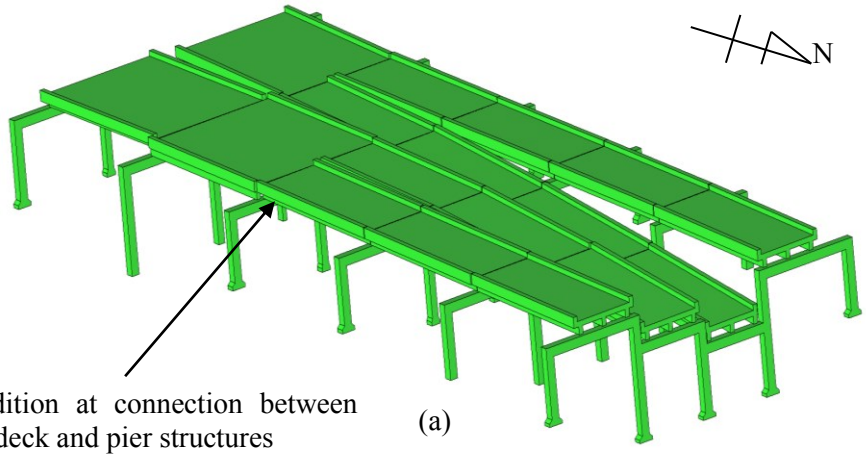

Tie condition at connection between freeway deck and pier structures

(a)

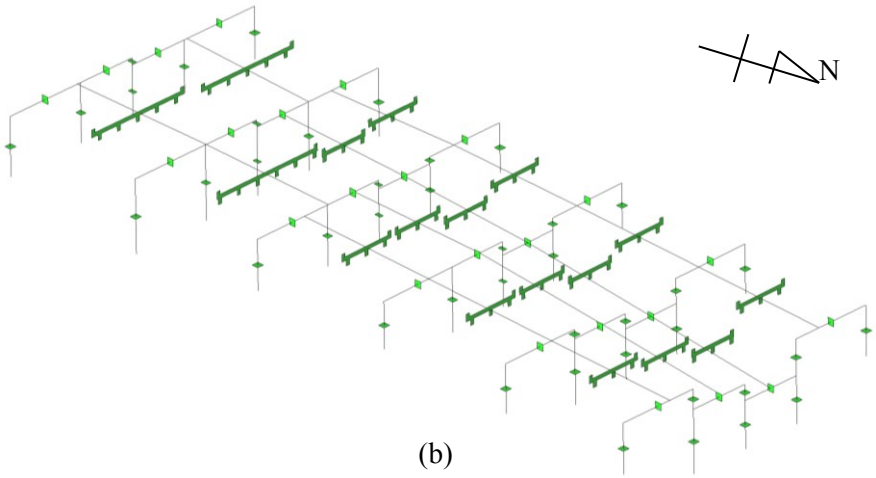

(b)

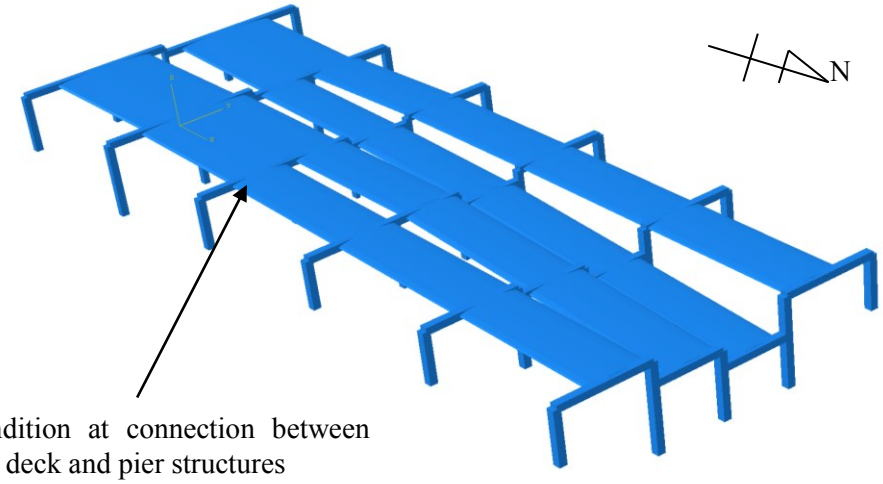

Tie condition at connection between freeway deck and pier structures

(c)

Figure 4.40: Selected part for frequency analysis: (a) solid CAD model; (b) frame CAD model with assigned cross-sections; and (c) developed FEM frame model.

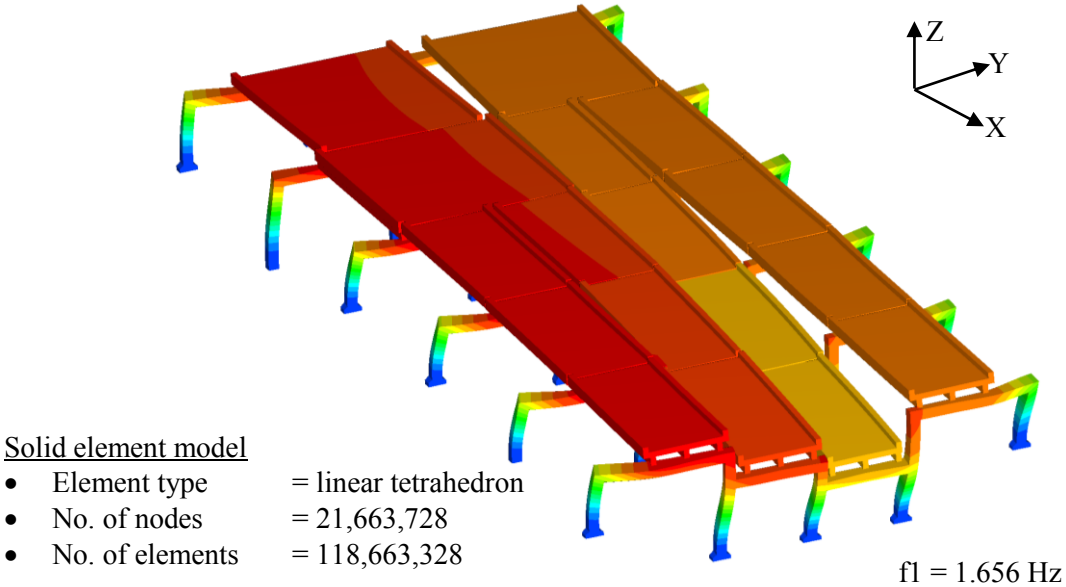

Solid element model

- Element type = linear tetrahedron
- No. of nodes = 21,663,728
- No. of elements = 118,663,328

f1 = 1.656 Hz

(a)

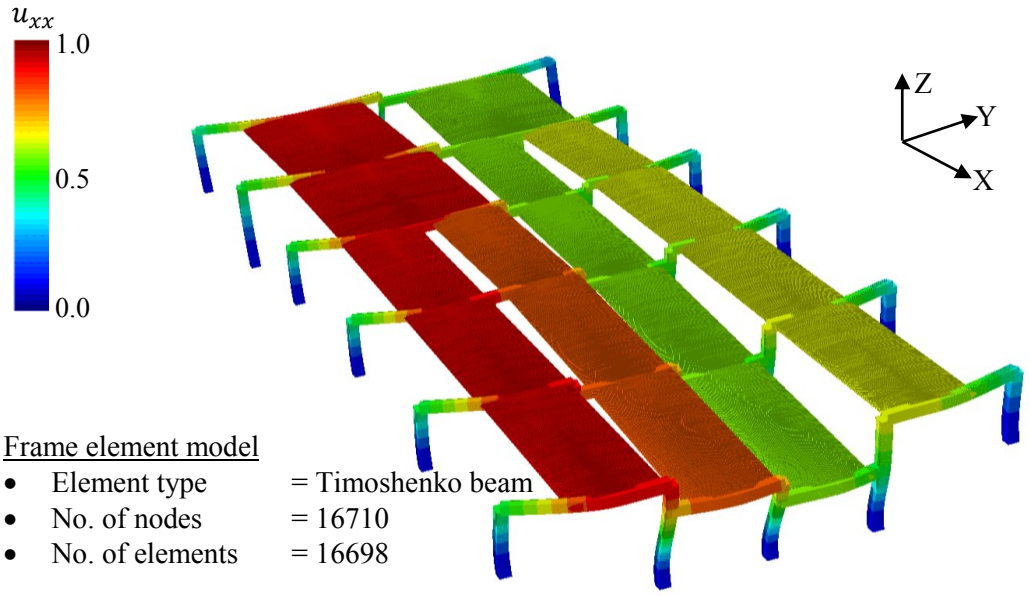

Frame element model

- Element type = Timoshenko beam
- No. of nodes = 16710
- No. of elements = 16698

f1 = 1.410 Hz

(b)

Figure 4.41: First mode shape along longitudinal direction of selected freeway junction part: (a) solid element model; and (b) frame element model.

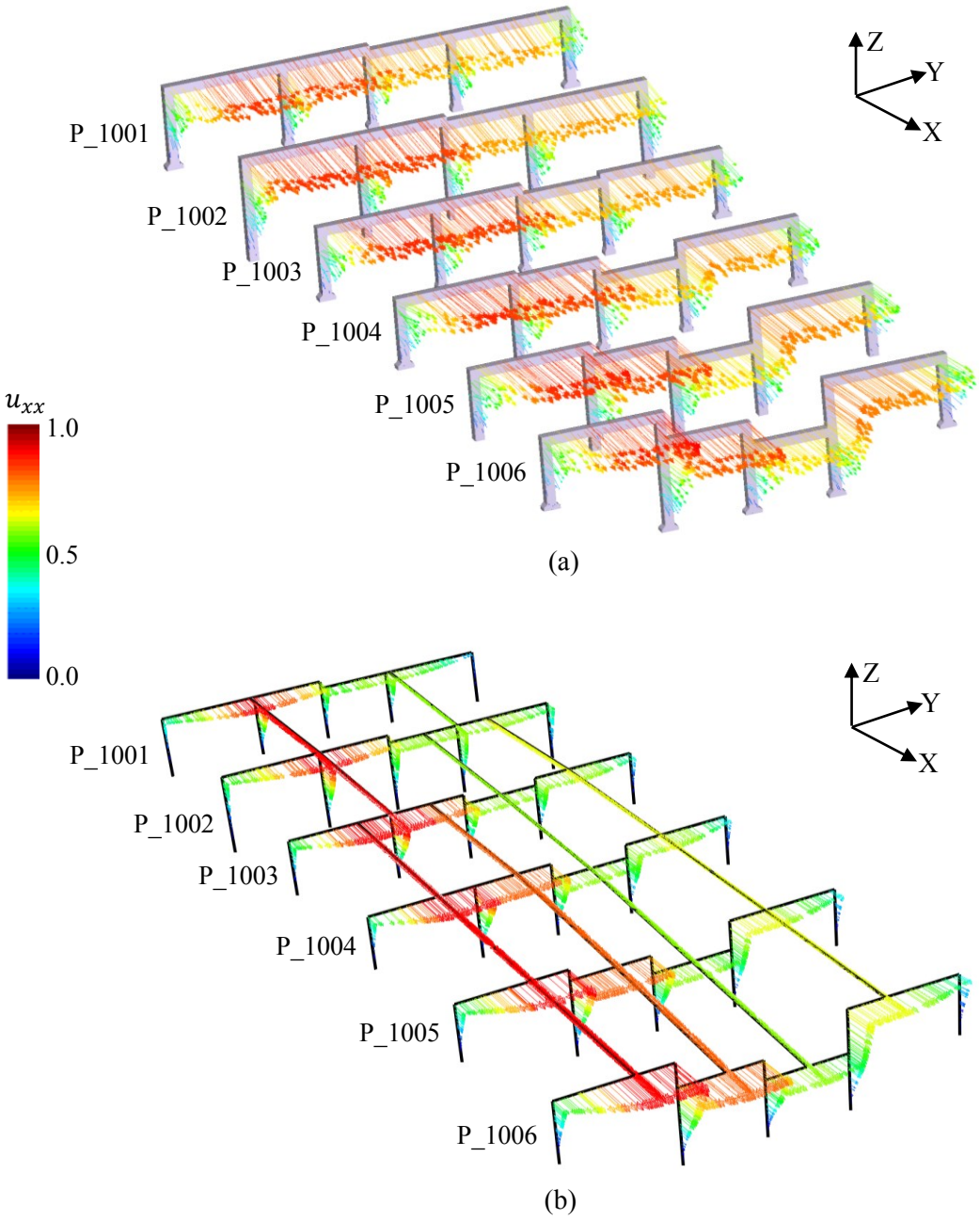

Figure 4.42: Displacement vector component along x-direction for pier structures of selected freeway junction part (1st mode shape along longitudinal direction): (a) solid element model; and (b) frame element model.

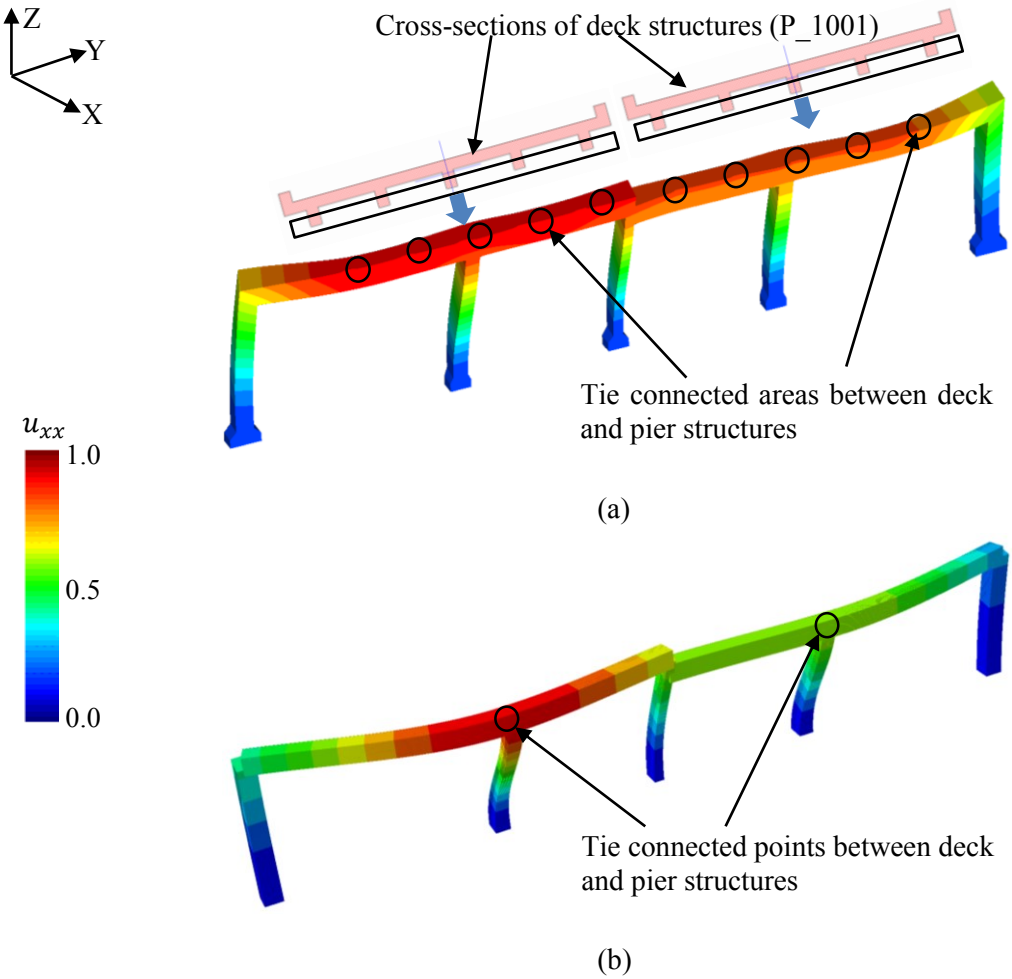

Figure 4.43: Tie condition behavior between deck and pier structures (P_1001): (a) solid element model; and (b) frame element model.

Chapter 5

Possible Improvements for Developed Tools

5.1 Use of modal analysis for consistent lumped mass modeling (CLMM)

Approximate displacement functions which can be used to construct a consistent lumped mass model (CLMM) are found by using a modal analysis [42, 43, 44]. Modal analysis means solving the following eigenvalue problem of w:

$$\begin{cases} \omega^2 Aw + (EIw'')'' = 0 & 0 < x < L, \\ (w, w') = (0,0) & x = 0, \\ (w, w'') = (1,0) & x = L. \end{cases} \tag{5.1}$$

Here, ω is the natural frequency. As is seen, this model is for the translation. Another modal analysis is made for the rotation, i.e.,

$$\begin{cases} \omega^2 Ah + (EIh'')'' = 0 & 0 < x < L, \\ (h, h') = (0,0) & x = 0, \\ (h, h'') = (1,0) & x = L. \end{cases} \tag{5.2}$$

The same symbols, w and h, are used as those at quasi-static state; see Eqs. (3.6) and (3.10).

For each eigenvalue of ω, the corresponding eigenfunction for w or h is determined. The approximate displacement function is expressed in terms of the corresponding eigenfunctions as

$$\mathrm{u}_3(x,t) = \sum_{\alpha} U^{\alpha}(t) w^{\alpha}(x) + \sum_{\beta} \Theta^{\beta}(t) h^{\beta}(x), \tag{5.3}$$

where w^{α} and h^{β} are the α-th and β-th eigenfunctions for w and h.

Substitution of u_3 with corresponding $u_1 = -zu_3'$ into the modified Lagrangian results in another lumped mass model. For simplicity, replacing the symbol $\{\Theta^{\beta}, h^{\alpha}\}$ with $\{U^{N+\beta}, w^{N+\beta}\}$ with N being the number of the modes used, we rewrite Eq. (5.3) as

$$u_3(x,t) = \sum_{\alpha} U^{\alpha}(t) w^{\alpha}(x), \tag{5.4}$$

and calculate the modified Lagrangian, as

$$\mathcal{L} = \sum \frac{1}{2} M_{\alpha\alpha} \left(\dot{U}^{\alpha}(t)\right)^2 - \frac{1}{2} K_{\alpha\alpha} (U^{\alpha}(t))^2 + \sum \frac{1}{2} M_{\alpha\beta} \dot{U}^{\alpha}(t) \dot{U}^{\beta}(t) - \frac{1}{2} K_{\alpha\beta} U^{\alpha}(t) U^{\beta}(t), \tag{5.5}$$

where

$$\{M_{\alpha\beta}, K_{\alpha\beta}\} = \int \left\{ \rho \left(A w^{\alpha} w^{\beta} + I (w^{\alpha})' \left(w^{\beta}\right)' \right), EI (w^{\alpha})'' \left(w^{\beta}\right)'' \right\} \, \mathrm{d}x. \tag{5.6}$$

Note that the integration of $w^{\alpha}w^{\beta}$, $(w^{\alpha})'\left(w^{\beta}\right)'$ and $(w^{\alpha})''\left(w^{\beta}\right)''$ does not vanish for $\alpha \neq \beta$, and hence coupling of different U^{α} 's always happens.

5.2 Meta-modeling based pre-conditioning for conjugate gradient method (CG method)

Meta-modeling could be used as new pre-conditioning of a conjugate gradient (CG) method [47, 48, 49, 51, 52] of solid element analysis; most of the pre-conditionings are based on mathematics, and we have not found any studies which seek to apply physics based meta-modeling for pre-conditioning. The basic idea of this pre-conditioning is the use of a solid element solution converted from a beam element solution as an initial solution of the CG method.

To explain the above idea clearly, we denote by $[u^s]$ and $[u^c]$ the beam element solution and the converted solid element solution, respectively. Since $[u^s]$ is regarded as an approximate solution of the continuum mechanics problem, it is expected that $[u^c]$ which is converted from $[u^s]$ will serve as a good initial solution of the CG method.

As for the pre-conditioning, it is desirable to have the residual force, $[r^c]$, which corresponds to $[u^c]$. However, it is not easy to find $[r^c]$, since $[u^s]$ is the exact solution of the beam problem and the corresponding residual force vanishes. $[r^c]$ must be computed by using $[u^c]$. Note that even though $[u^s]$ is exact, there is no guarantee that the converted $[u^c]$ is exact, as well.

It is of interest to seek a method of smartly computing $[r^c]$ when $[u^s]$ is not the exact solution and accompanies residual force, denoted by $[r^s]$. We start to consider a differential equation as a linear transformation of a function, $\mathbf{k}[\mathbf{u}] = \mathbf{r}(\mathbf{x})$ for $\mathbf{x}$ in V with $\mathbf{k}[\mathbf{u}] = \boldsymbol{\nabla} \cdot (\mathbf{c}: \boldsymbol{\nabla}\mathbf{u})$. Denoting a basis function by φ^{γ}, we can discretize this operator

$$\int \varphi^{\gamma}(\mathbf{x})\, \mathbf{k}[\mathbf{u}](\mathbf{x})\, \mathrm{d}v = \int \varphi^{\gamma}(\mathbf{x})\, \mathbf{r}(\mathbf{x})\, \mathrm{d}v$$

from which a discretized form of the linear transformation is derived, as

$$[k][u] = [r];$$

depending on the choice of φ^{γ}, the above discretized form corresponds to a solid element analysis or a beam element analysis.

In the solid element analysis, $\mathbf{u}$ is discretized in terms of the basic functions $\{\eta^{\beta}\}$ as $\mathbf{u} = \sum \mathbf{u}^{\beta}\eta^{\beta}$ with $\mathbf{u}^{\beta}$ being components of $[u^c]$. When $\mathbf{r}$ is discretized in a similar form, as $\mathbf{r} = \sum \mathbf{r}^{\beta}\eta^{\beta}$, then, $[r^c]$ is given as a product of certain coefficients (which are computed by integrating η^{β}) and components of $\mathbf{r}^{\beta}$. Note that $[r^c]$ is not given by $\mathbf{r}^{\beta}$ since the basis functions $\{\eta^{\beta}\}$ are not orthonormal.

Even though it is not mathematically rigorous, we may approximately find $\mathbf{r}$ from $[r]$, considering that $\mathbf{r}$ physically corresponds to a body force; it is a standard practice to a given distribute body force to nodal force or $[r]$. Once a function $\mathbf{r}$ is found, discretizing it

in terms of the basis functions is not a difficult task. However, we have to emphasize that this procedure is an approximation and not a rigorous conversion.

Chapter 6

Concluding Remarks

This dissertation presents an application of a meta-modeling theory to a bridge structure, in order to realize seismic structural response analysis that uses a set of consistent models. Such seismic structural response analysis can be used as a more rational estimation method of possible earthquake disaster for an urban area as compared to the current method that is based on fragility or vulnerability curve. Considering the quality and quantity of data that are available for a bridge structure, we develop a methodology based on the meta-modeling theory for the automated model construction. Gradually increasing the fidelity of an automated model, we are able to assure the model quality, since model validation is easier for a simpler model with a fewer parameters and a simpler model is used as reference in validating a more complicated model.

Following are the three main achievements of this study: 1) the rigorous conversion from a solution of a solid element model to a solution of a beam element model or vice versa; 2) the construction of a simple analysis model which shares the fundamental dynamic properties with a solid element model; and 3) the development of modules that automatically decodes and interprets a set of digital data of a structure and constructs a set of consistent analysis models for seismic structural analysis.

It is shown that the solution conversion method, which is based on the meta-modeling theory, can be used as an alternative of an ordinary method of computing cross sectional forces of a solid element method, which integrates stress acting on a cross section, with laborious determination of the value of stress on the cross section. Further investigation is needed to ensure the potential usefulness of the solution conversion method. The solution conversion method should be applied to a two-dimensional structure such as plate and shell in the future. The solution conversion method may provide a possibility of improving the CG method, as it provides a beam element solution as an accurate initial solution of a solid element analysis. From the viewpoint of computational mechanics, the use of a structure element solution as pre-conditioning of the solver of the solid element analysis seems interesting as well as important. While there are numerous mathematical studies about pre-conditioning, as far as the author has studied, little research achievement is found to develop physics-based pre-conditioning, i.e., the use of a solution of an approximated problem; see Sec. 5.2.

Simple models such as CLMM and CMSM are developed in this study. It is shown that both CLMM and CMSM are successfully constructed for different types of multi and single -span bridge structures. It is also shown that the constructed CMSM is consistent in the sense that it has the same natural frequencies of the first few modes and is able to compute dynamic response of displacement as well as force. This is due to the fact that the CMSM is constructed by applying purely mathematical approximations to the Lagrangian of continuum mechanics. It does not lose any physical meaning of an original continuum mechanics model but does solve the mathematical problem of the continuum mechanics model approximately. Current CLMM needs to be improved by introducing a deformable deck structure in its formulation, which will give complete consistency with the first mode

of the frame model of a bridge structure of arbitrary configuration. There is a possibility of constructing a more accurate CMSM by extending the number of the mass points. Also, there is a possibility of extending CMSM and CLMM to non-linear structure. At least, it is straightforward to apply the meta-modeling theory to incremental response of a non-linear elasto-plastic structure.

The developed module of the automated model construction is able to use two sets of digital data (Auto CAD and GIS) of a target bridge structure and to generate a solid element model, a frame model, a CMSM or a CLMM. The module is tested with a set of multi-span bridge and a part of a freeway network in Tokyo metropolitan area successfully. The quality of these models of distinct fidelity is assured by comparing the fundamental properties and the synthesized response. These results highlight two necessary improvements required for the module: 1) need of consistency in connection and boundary condition treatment for frame element model; and 2) need of other structure element models such as plate and shell for this module. Those necessary improvements need to be implemented to this automated model construction module in future.

References

[1] H. Dobashi, T. Hatsuku, T. Ichimura, M. Hori, T. Yamada, N. Ohbo, M. Moriguchi, and H. Itami, "Full 3D Seismic Response Analysis of Underground Ramp Tunnel Structure Using Large-Scale Numerical Computation," in *The 14th World Conference on Earthquake Engineering,* Beijing, China, 2008.

[2] H. Dobashi, Y. Terashima, M. Hori, T. Ichimura, N. Ohbo, T. Yamada, and T. Obara, "Seismic Performance Analysis of Underground Ramp Tunnel Structure Using 3-D Massive Numerical Computation," in *III ECCOMAS Thematic Conference on Computational Methods in Structural Dynamics and Earthquake Engineering*, Corfu, Greece, 2011.

[3] R. L. Boroschek, M. O. Moroni, and M. Sarrazin, "Dynamic characteristics of a long span seismic isolated bridge," *Engineering Structures*, vol. 25, no. 12, pp. 1479–1490, Oct. 2003.

[4] T. S. Paraskeva, A. J. Kappos, and A. G. Sextos, "Extension of modal pushover analysis to seismic assessment of bridges," *Earthquake Engineering and Structural Dynamics*, vol. 35, no. 10, pp. 1269–1293, 2006.

[5] T. K. Makarios and T. N. Salonikios, "Use of New Equivalent Nonlinear SDF System of Planar Multi-Storey R/C Frames in Static Pushover Procedure," in *The 14th World Conference on Earthquake Engineering*, Beijing, China, 2008.

[6] Y. Shao, S. Aval, and A. Mirmiran, "Fiber-element model for cyclic analysis of concrete-filled fiber reinforced polymer tubes," *Journal of structural engineering*, pp. 292–303, 2005.

[7] S. Alali, L. Jianzhong, and G. Guanzhong, "Double deck bridge behavior and failure mechanism under seismic motions using nonlinear analyzes," *Earthquake Engineering & Engineering Vibration*, vol. 12, no. 3, pp. 447–461, 2013.

[8] S. H. Yeom, G. H. Koo, and J. H. Lee, "Development of Simple Modal Analysis Model for KALIMER-600 Reactor Building," Daejeon, Korea, 2006.

[9] M. K. Bose, R. S. Soni, S. C. Mahajan, and A. Kakodkar, "Strain Energy Concept for Developing Lumped Mass Stick Model of Complex Structures," in *11th World Conference on Earthquake Engineering*, 1996.

[10] H. Lee, H. Roh, J. Youn, and J. S. Lee, "Frequency Adaptive Lumped-Mass Stick Model and Its Application to Nuclear Containment Structure," in *15th World Conference on Earthquake Engineering*, Lisbon, Portugal, 2012.

[11] M. Hori, L. Maggededaera, T. Ichimura, and S. Tanaka, "Meta-Modeling for Constructing Model Consistent with Continuum Mechanics," *Journal of Structural Mechanics and Earthquake Engineering*, vol. 9, no. 4, pp. 269–275, 2014.

[12] M. Hori, S. Tanaka, L. Wijerathne, T. Ichimura, and J. A. S. C. Jayasinghe, "Meta-Modeling for Consistent Seismic Response Analysis," in *5th ECCOMAS Thematic Conference on Computational Methods in Structural Dynamics and Earthquake Engineering*, Crete Island, Greece, 2015.

[13] J. A. S. C. Jayasinghe, S. Tanaka, L. Wijerathne, M. Hori, and T. Ichimura, "Rigorous Conversion of Solid and Beam Element Solutions Based on Meta-Modeling," *Journal of JSCE (Applied Mechanics)*, vol. 70, no. 2, pp. 223–233, 2014.

[14] J. A. S. C. Jayasinghe, S. Tanaka, L. Wijerathne, M. Hori, and T. Ichimura, "Automated Construction of Consistent Lumped Mass Model for Road Network," *Journal of JSCE (Structural and Earthquake Engineering)*, vol. 71, 2015.

[15] J. A. S. C. Jayasinghe, S. Tanaka, L. Wijerathne, M. Hori, and T. Ichimura, "Conversion Between Solid and Beam Element Solutions of Finite Element Method Based on Meta-Modeling," in *ICCBEI, 2nd International Conference*, Tokyo, Japan, 2015.

[16] R. L. Taylor and O. C. Zienkiewicz, *The Finite Element Method for Solid and Structural Mechanics*, 6th ed., Amsterdam: Butterworth-Heinemann, 2005.

[17] O. Gonzalez and A. M. Stuart, *A first course in continuum mechanics*. Cambridge: Cambridge University Press, 2008.

[18] J. H. Heinbockel, "Introduction to Tensor Calculus and Continum Mechanics," Department of mathematics and statistics, Old Dominion university, 1996.

[19] J. N. Reddy, *An introdution to continuum mechanics*. Cambridge: Cambridge University Press, 2008.

[20] J. F. Doyle, *Wave Propagation in structures* (Mechanical engineering series), 2nd ed., New York: Springer, 1997.

[21] E. T. Kruszewski, "Effects of Transverse Shear and Rotary Inertiaon the Natural Frequency of a Uniform Beam." National Advisory Committee for Aeronautics, Washington, 1949.

[22] S. P. Timoshenko, "On the transverse vibrations of bars of uniform cross-section," *Philosophical Magazine Series 6*, vol. 43, no. 253, pp. 125–131, 1922.

[23] T. C. Huang, "The Effect of Rotatory Inertia and of Shear Deformation on the Frequency and Normal Mode Equations of Uniform Beams With Simple End Conditions," *Journal of Applied Mechanics*, vol. 28, no. 4, p. 579, 1961.

[24] G.-Q. Li and J.-J. Li, "A tapered Timoshenko–Euler beam element for analysis of steel portal frames," *Journal of Constructional Steel Research*, vol. 58, no. 12, pp. 1531–1544, Dec. 2002.

[25] S. M.Han, H. Benaroya, and T. Wei, “Dynamics of Transversely Vibrating Beams Using Four Engineering Theories,” *Journal of Sound and Vibration*, vol. 225, no. 5, pp. 935–988, 1999.

[26] A. Özütok and A. Akin, “The solution of Euler-Bernoulli beams using variational derivative method,” *Scientific Research and Essays*, vol. 5, pp. 1019–1024, 2010.

[27] R. W. Traill-nash and A. R. Collar, “The effects of shear flexibility and rotatory inertia on the bending vibrations of beams,” *Quarterly Journal of Mechanics and Applied Mathematics*, vol. 6, no. 2, pp. 186–222, 1953.

[28] N. M. Auciello and M. Lippiello, “Vibration analysis of rotating non-uniform Rayleigh beams using ‘ CDM ’ method,” in *Global Virtual Conference*, 2013, pp. 528–533.

[29] R. D. Mindlin, “Influence of Rotatory Inertia and Shear on Flexural Motions of Isotropic, Elastic Plates,” *Journal of Applied Mechanics-Transactions of the Asme*, vol. 18, pp. 31–38, 1951.

[30] E. Reissner and M. Stein, “Torsion and transverse bending of cantilever plates.” National Advisory Committee for Aeronautics, Washington, 1951.

[31] J. N. Reddy, *Theory and Analysis of Elastic Plates and Shells*, 2nd ed., New York: Taylor and Francis, 2006.

[32] S. P. Timoshenko and S. Woinowsky-Krieger, *Theory of Plates and Shells*. New York: McGraw-Hill, 1959.

[33] K. D. Hjelmstad, *Fundamentals of Structural Mechanics*, 2nd ed., New York: Springer, 2005.

[34] C. K. Wang, “Stability of rigid frames with nonuniform members,” *Journal of Structural Division*, vol. 93, pp. 275–294, 1967.

[35] H. Rao and C. Spyrakos, “Closed form series solutions of boundary value problems with variable properties,” *Computers & structures*, vol. 23, no. 2, pp. 211–215, 1986.

[36] G. M. Calvi and G. R. Kingsley, “Displacement-Based Seismic Design of Multi-Degree- of-Freedom Bridge Structures,” *Earthquake Engineering & Structural Dynamics*, vol. 24, April, pp. 1247–1266, 1995.

[37] B. C. Beggs, L. Young, and R. R. Johnson, “Response of MDOF Systems to Multiple Support Seismic Excitation,” *Journal of Engineering Mechanics*, vol. 114, no. 2, pp. 583–603, 1987.

[38] A. J. Carr, “Dynamic Analysis of Structures,” *Bulletin of The New Zealand National Society for Earthquake Engineering*, vol. 27, no. 2, 1994.

[39] J. A. P. Norman, D. W. Virden, A. Crewe, D. J. Wagg, and R. Severn, “Understanding the dynamic of multi-degree-of-freedom structures subject to

multiple support earthquake excitation," in *13th World Conference on Earthquake Engineering*, Vancouver, B.C., Canada, 2004.

[40] "ADVENTURECluster Visual 4.5 User's Manual," Allied Engineering Corporation, 2013.

[41] "ADVENTURECluster Builder 4.3 取扱説明書," Allied Engineering Corporation, 2012.

[42] A. K. Chopra, *Dynamics of Structures (Theory and Applications to Earthquake Engineering)*, 3rd ed., New Jersey: Prentice Hall, 1995.

[43] J. He and Z.-F. Fu, *Modal Analysis*. Boston: Butterworth-Heinemann, 2001.

[44] R. W. Clough and J. Penzien, *Dynamics of structures*, 2nd ed., New York: McGraw-Hill, 2000.

[45] J. Cottrell, T. J. Hughes, and Y. Bazilevs, *Isogeometric analysis*, 1st ed., New York: Wiley, 2009.

[46] M. G. Sfakianakis, "Biaxial bending with axial force of reinforced, composite and repaired concrete sections of arbitrary shape by fiber model and computer graphics," *Advances in Engineering Software*, vol. 33, no. 4, pp. 227–242, 2002.

[47] W. L. Briggs, "Multigrid Tutorial," Center for Applied Scientific Computing, Lawrence Livermore National Laboratory, 2000.

[48] E. Caraba, "Preconditioned Conjugate Gradient Algorithm," Louisiana State University, 2008.

[49] J. R. Shewchuk, "An introduction to the conjugate gradient method without the agonizing pain," Natural Sciences and Engineering Research Council of Canada, 1994. [Online]. Available: http://www.eletrica.ufpr.br/artuzi/te804/arquivos/cg.pdf.

[50] H. Song, "Preconditioning Techniques Analysis for CG Method," Department of Computer Science University of California, [Online]. Available: http://www.cs.ucdavis.edu/~bai/ECS231/returnsfinal/Song.pdf.

[51] O. Tatebe, "The multigrid preconditioned conjugate gradient method," *NASA Conference Publication*, 1993.

[52] T. Jacobi and S. Gilbert "Multigrid Methods," 2006. [Online]. Available: http://ocw.mit.edu/courses/mathematics/18-086-mathematical-methods-for-engineers-ii-spring-2006/readings/am63.pdf.

[53] B. K. Jang and R. T. Chin, "Analysis of thinning algorithms using mathematical morphology," *IEEE Transactions on Pattern Analysis and Machine Intelligence*, vol. 12, no. 6, pp. 541–551, 1990.

[54] “Strong-motion Seismograph Networks (K-NET and KiK-net).” [Online]. Available: http://www.kik.bosai.go.jp/.

[55] M. J. Kowalsky, M. J. N. Priestley, and G. A. Macrae, “Displacement-Based Design of RC Bridge Columns in Seismic Regions,” *Earthquake Engineering & Structural Dynamics*, vol. 24, pp. 1623–1643, 1995.

[56] M. J. Kowalsky, “A Displacement-Based Approach for The Seismic Design of Continuous Concrete Bridges,” *Earthquake Engineering & Structural Dynamics*, vol. 31, pp. 719–747, 2002.

Appendix A

Index Form of $\mathcal{L}^*$

In terms of tensor components of a Cartesian coordinate system, (x_i for $i = 1, 2, 3$), the $\mathcal{L}^*$ is expressed as

$$\mathcal{L}^* = \int \frac{1}{2}\rho v_i v_i - \left(\sigma_{ij}\epsilon_{ij} - \frac{1}{2}\sigma_{ij}c^{-1}_{ijkl}\sigma_{kl}\right) \mathrm{d}v,$$

where summation convention is employed for repeated indices.

Appendix B

Definition of Approximate Function

An exact solution lies in a function space of continuum mechanics, i.e., a set of three displacement component functions for three spatial variables and one temporal variable. When a suitable subset is defined for the function space of continuum mechanics, we can find the most proper function in this subset that is closest to the exact solution. This function in the subset is regarded as an approximate solution in the sense that it belongs to the subset and is closest to the exact solution.

As an illustrative example, suppose that $\{u_1, u_2, u_3\} = \{x_1 + \epsilon x_2, \epsilon x_3, \epsilon x_2 x_3\}$ is an exact solution at quasi-static state, with $\epsilon \ll 1$. An approximate solution is $\{u_1, u_2, u_3\} = \{x_1, 0, 0\}$ as terms of the order of ϵ are dropped. This approximate function is regarded as a function in the subset of $\{u_1, u_2, u_3\} = \{U(x_1), 0, 0\}$, i.e., a subset of functions whose non-zero component is u_1 only and it depends on x_1.

Appendix C

Conventional Force Computation

For simplicity, we consider a force acting on the spring that connects the first and second masses. That is, $F(t) = K_2(U^2(t) - U^1(t))$. By definition, the spring constant K_2 is expressed in terms of $k^{*\alpha\beta}$'s, which is computed by using $\int \boldsymbol{\nabla\psi}^\gamma : \mathbf{c} : \boldsymbol{\nabla\psi}^\gamma \, dv$. This integration is the volume integration of the square of the mode gradient over V (or the entire structure). More explicitly, denoting $\boldsymbol{\nabla\psi}^\gamma$ by $\mathbf{w}^\gamma$, we can rewrite the volume integration as

$$\int \boldsymbol{\nabla\psi}^\gamma : \mathbf{c} : \boldsymbol{\nabla\psi}^\gamma \, dv = \int \mathbf{w}^\gamma : \boldsymbol{\sigma}^\gamma \, dv,$$

where $\boldsymbol{\sigma}^\gamma = \mathbf{c} : \boldsymbol{\nabla\psi}^\gamma$ is the stress field that is associated with the γ-th mode, $\boldsymbol{\psi}^\gamma$. The volume integration is interpreted as the weighted average of this stress; the weight is the gradient of the mode.

Appendix D

Conjugate Gradient (CG) Algorithm

Algorithm 1. This algorithm is detailed below for solving $\mathbf{Ax} = \mathbf{b}$ where $\mathbf{A}$ is a real, symmetric, positive-definite matrix. The input vector (initial guess) $\mathbf{x}_0$ is constructed from equivalent beam system and λ is expected relative residual value of iteration.

$\mathbf{r}_0 \coloneqq \mathbf{b} - \mathbf{A}, \qquad \mathbf{p}_0 \coloneqq \mathbf{r}_0, \qquad k \coloneqq 0.$

For $k \coloneqq 1, \ldots \ldots, n-1$ (n is maximum number of iterations)

$$\alpha_k \coloneqq \frac{\mathbf{r}_k^T \mathbf{r}_k}{\mathbf{p}_k^T \mathbf{A} \mathbf{p}_k}$$

$$\mathbf{x}_{k+1} \coloneqq \mathbf{x}_k + \alpha_k \mathbf{p}_k$$

$$\mathbf{r}_{k+1} \coloneqq \mathbf{r}_k - \alpha_k \mathbf{A} \mathbf{p}_k$$

if $||\mathbf{r}_{k+1}||_2 / ||\mathbf{b}||_2 > \lambda$ then exit loop

$$\beta_k \coloneqq \frac{\mathbf{r}_{k+1}^T \mathbf{r}_{k+1}}{\mathbf{r}_k^T \mathbf{r}_k}$$

$$\mathbf{p}_{k+1} \coloneqq \mathbf{r}_k + \beta_k \mathbf{p}_k$$

the result is $\mathbf{x}_{k+1}$.

Appendix E

Automated Construction of Solid Element Model and Frame Model for Bridge Structure

The automated construction of a solid element model and a frame model is regarded as data conversion from a given set of digital data of a target bridge structure to a suitable analysis model of seismic structural response analysis. A key issue is that model could be a solid element model or a frame model. We develop modules for the automated construction, which is able to use AutoCAD data and GIS data and to construct a digital file which is used as input of data of the seismic structural response analysis.

The processes of the automated construction are divided into the following three sub processes:

I. Estimate global parameters of a target bridge structure;
II. Estimate local parameters of components of the target structure; and
III. Construct frame and solid models using the estimated global and local parameters.

Note that the AutoCAD data consist of numerous files, each of which includes information about configuration and material properties of a structural component. GIS data are used to allocate the structure components in a unified manner, so that the components form a structure. Global and local parameters are thus introduced to relate information of the AutoCAD data to the whole structure that is specified by the GIS data.

E.1 Estimation of global parameters

Estimation of the global parameters from the corrected AutoCAD data are briefly explained in Figs. e.1 and e.2. The global parameters include the following three parameters:

I. Pier location information with elevation information in the global coordinate;
II. Freeway centerline information in the global coordinate; and
III. Deck connectivity information for the full freeway network.

E.2 Estimation of local parameters

The local parameters estimation process is briefly explained in Fig. e.3. Estimated are the following three local parameters:

I. Closed polygon information for each pier and deck structures in the local coordinate;
II. Beam cross-sectional properties with geometric data for pier and deck structures in the local coordinate; and
III. Node-connectivity data of frame model for pier structure.

E.3 Estimation of local parameters

The estimated global and local parameters of a target bridge structure which is a part of a freeway network is arranged systematically, in order to construct a frame model and a solid element model. Digital files of these models are made in CAD format; see Figs. e.4 and e.5.

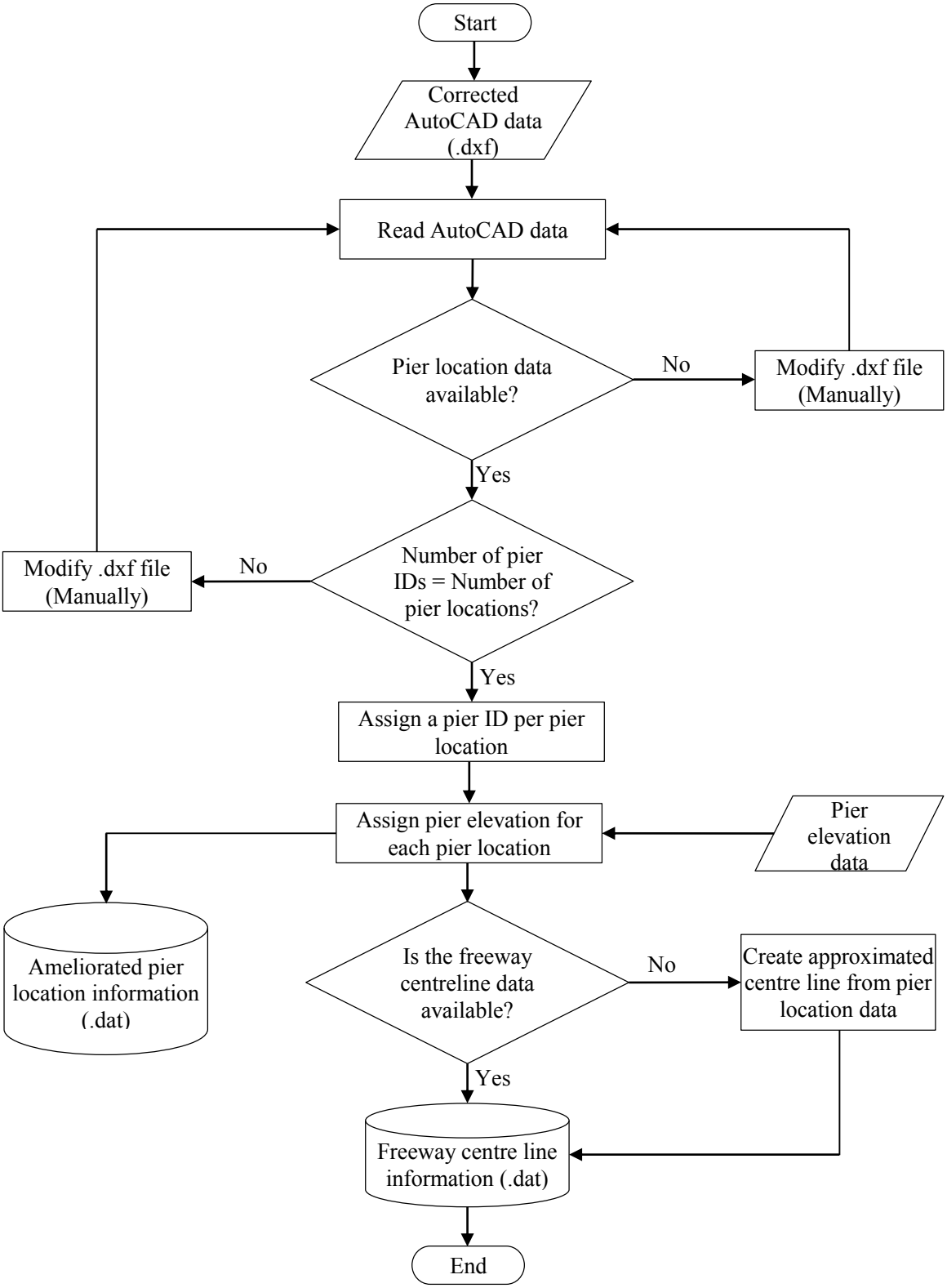

Figure e.1: Estimation of freeway global parameters: pier location information and centre line information of freeway network.

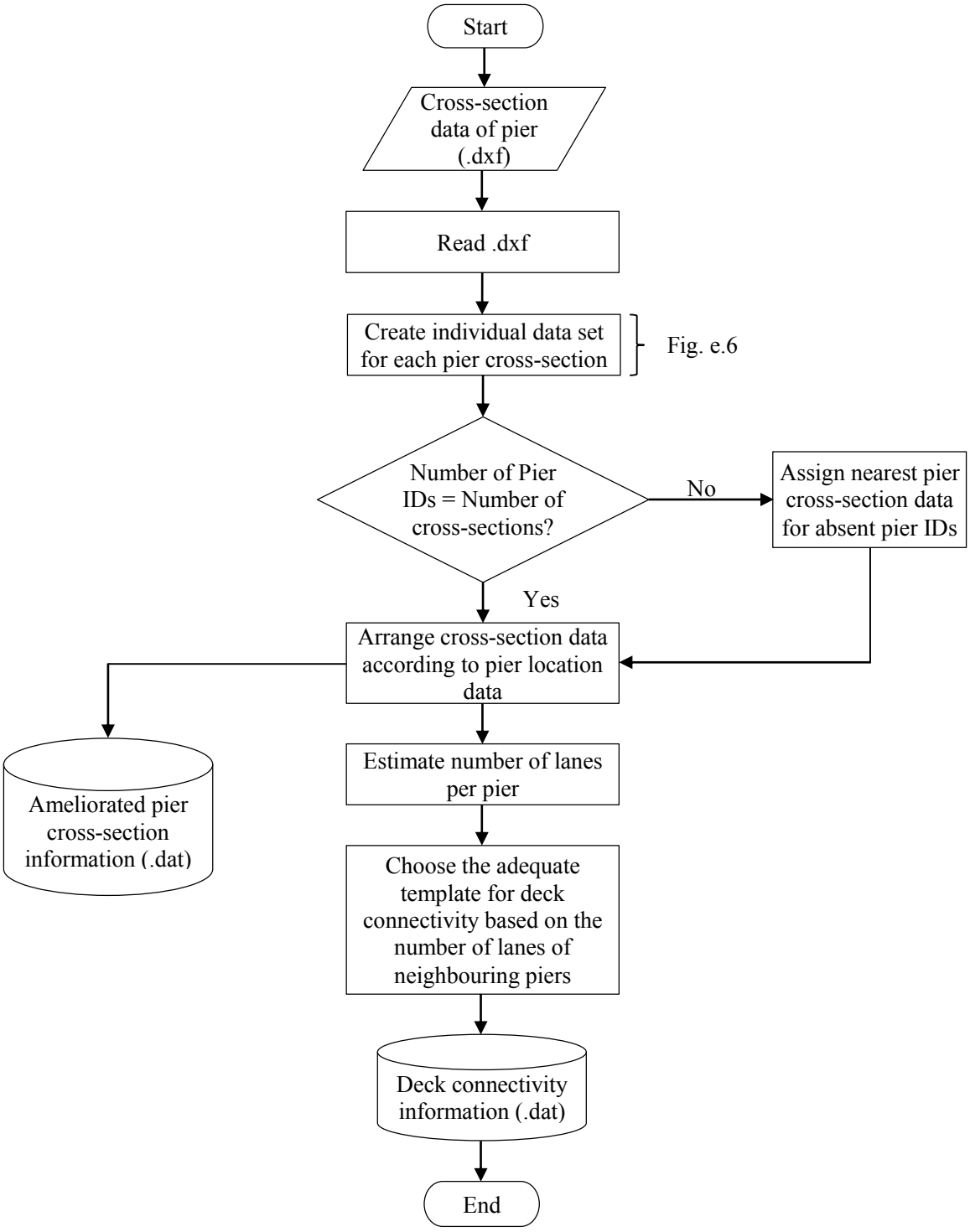

Figure e.2: Estimation of freeway global parameter: deck connectivity information of freeway network.

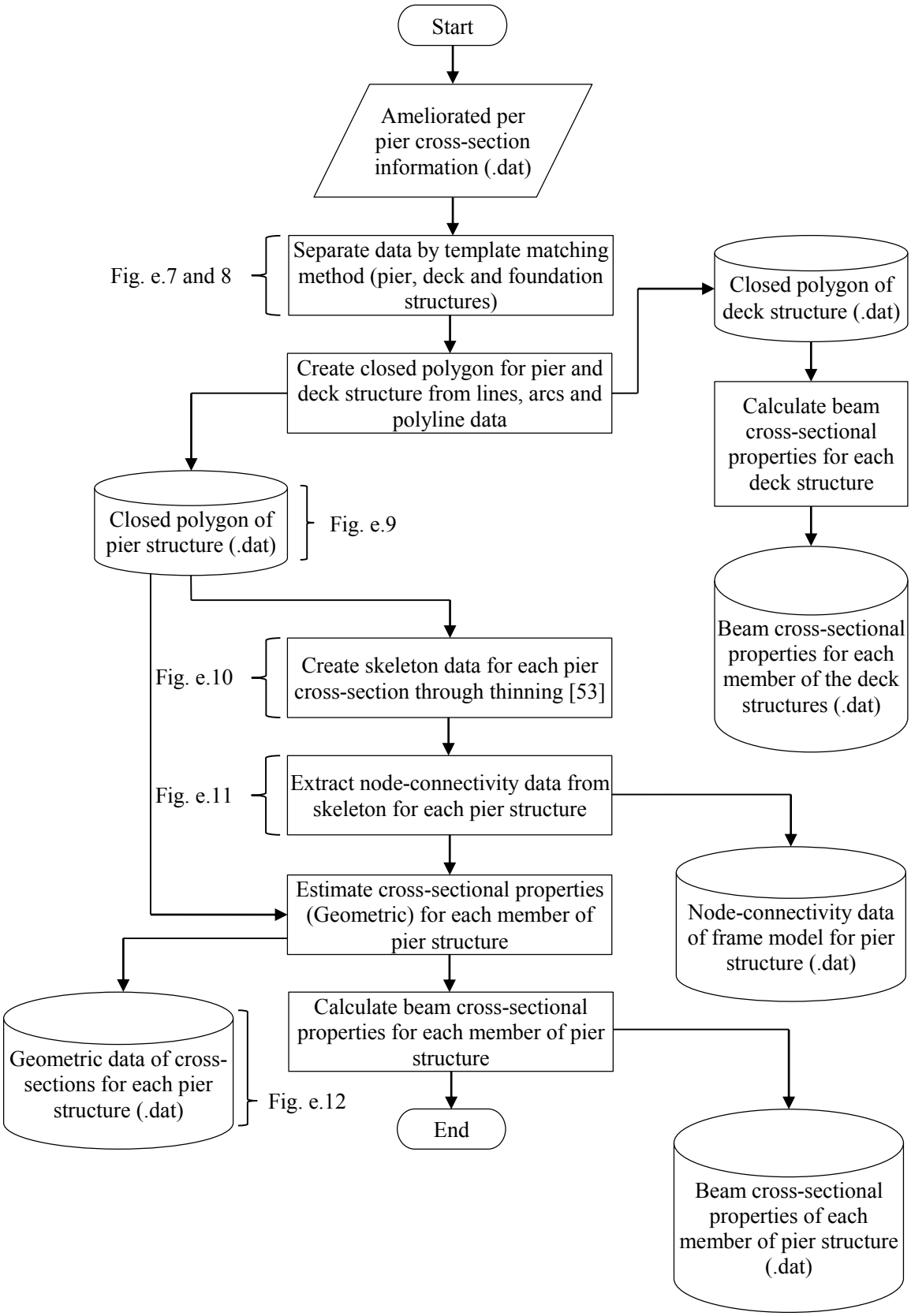

Figure e.3: Estimation of freeway local parameters.

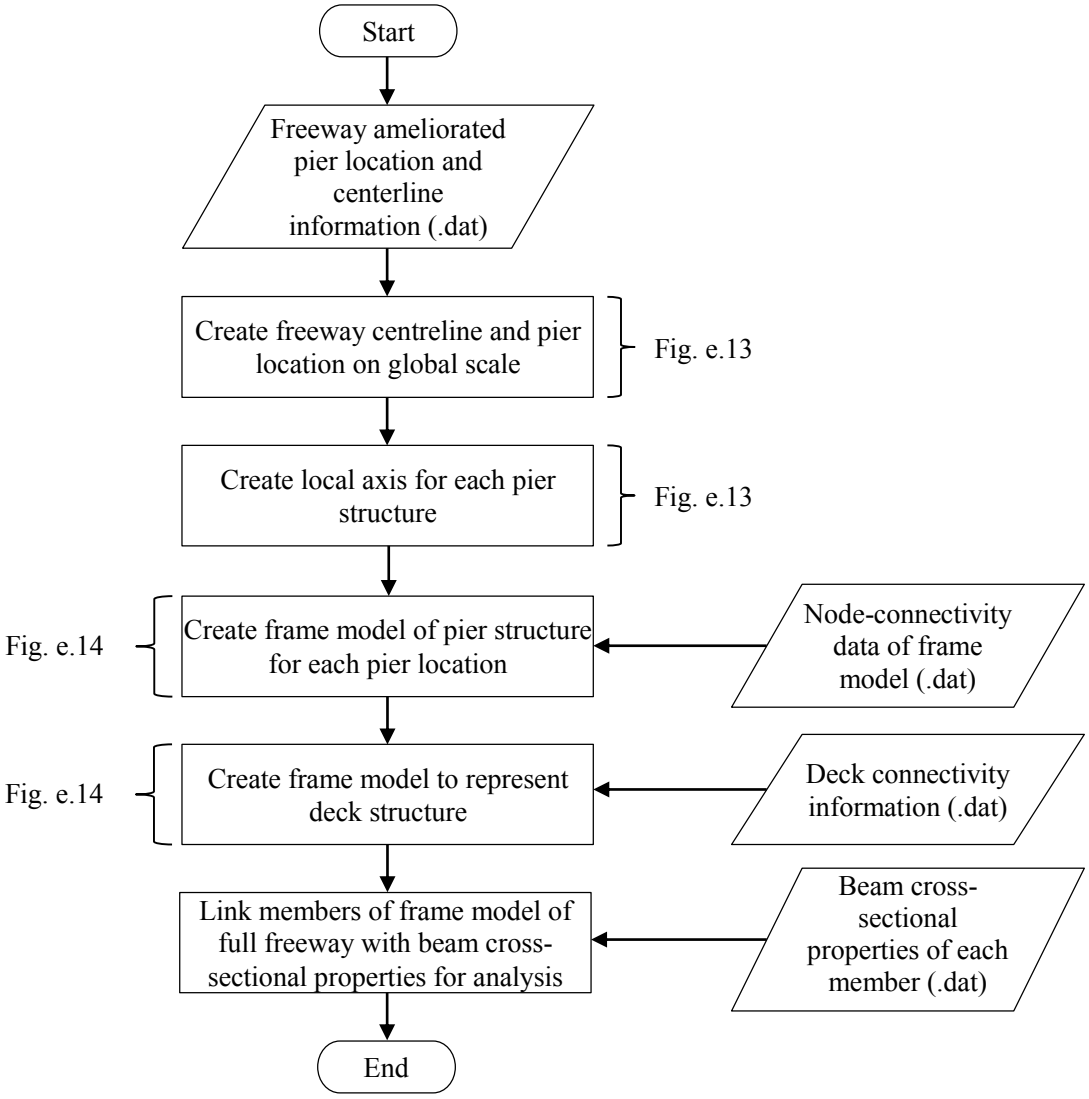

Figure e.4: Construction of frame CAD model for target freeway network.

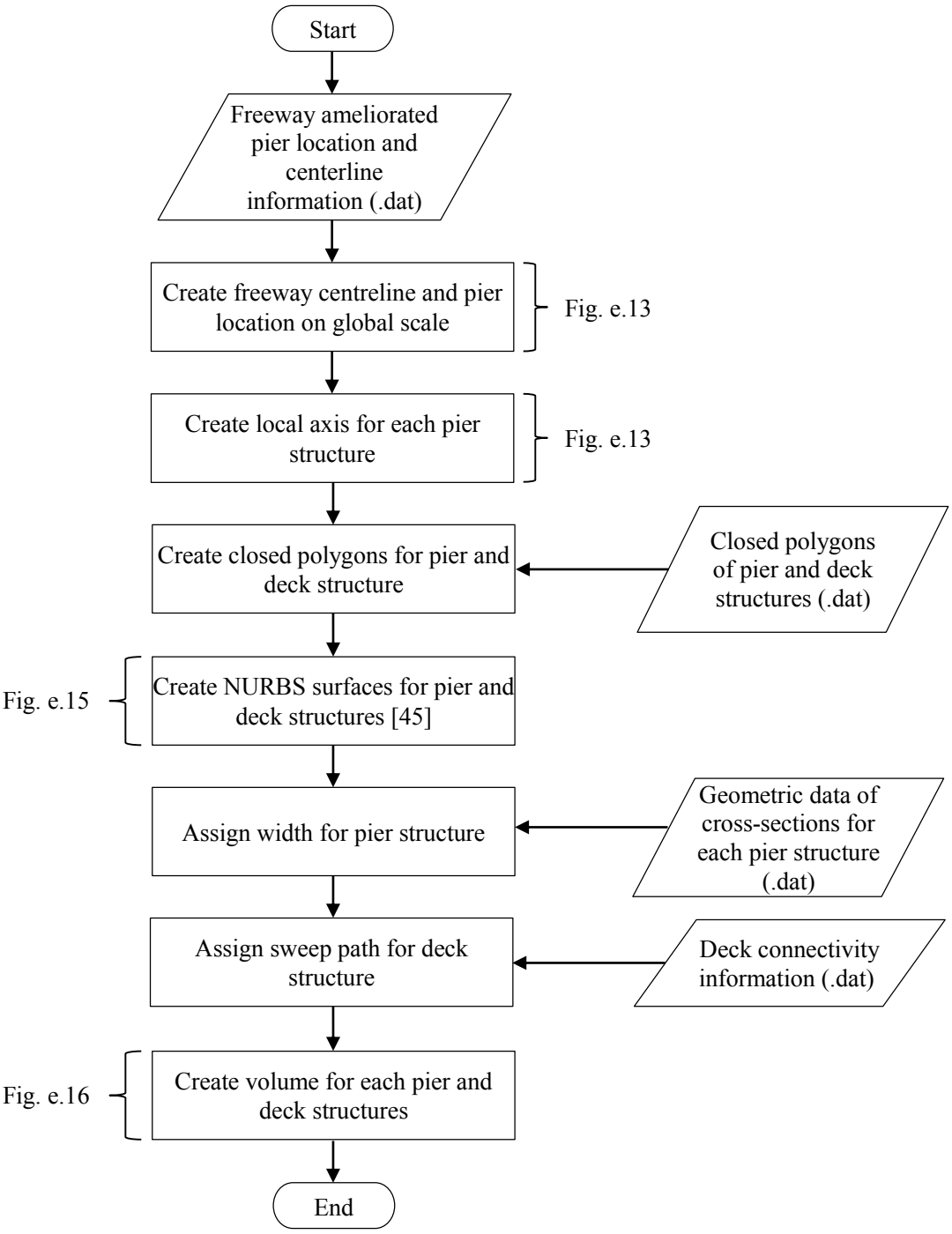

Figure e.5: Construction of solid CAD model for target freeway network.

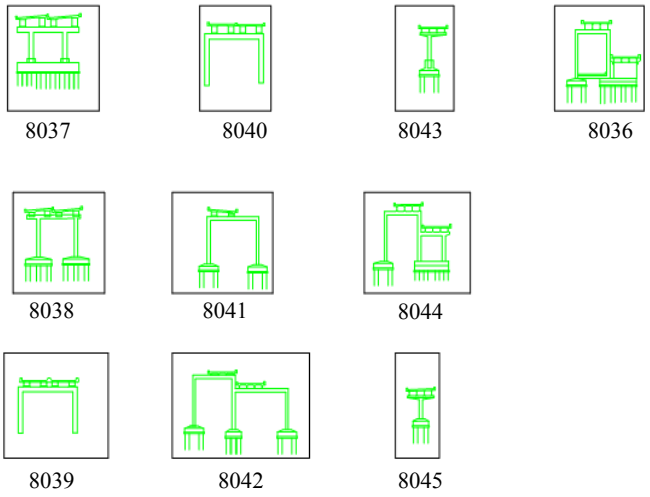

Figure e.6: Construction of individual data set for each pier cross-section.

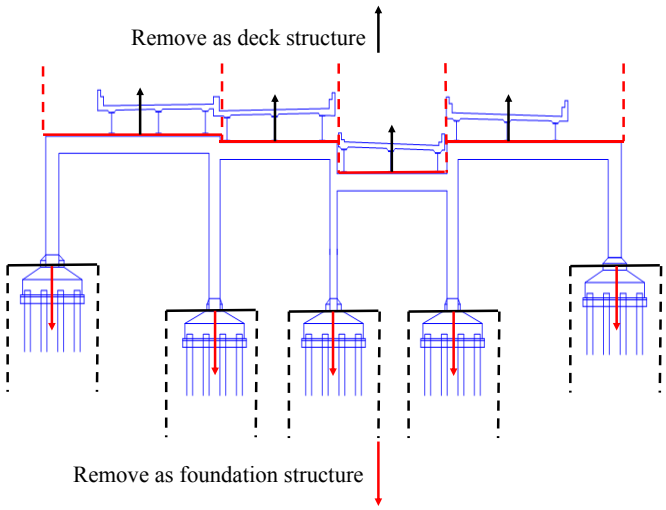

Figure e.7: Separation of geometric data by template matching method.

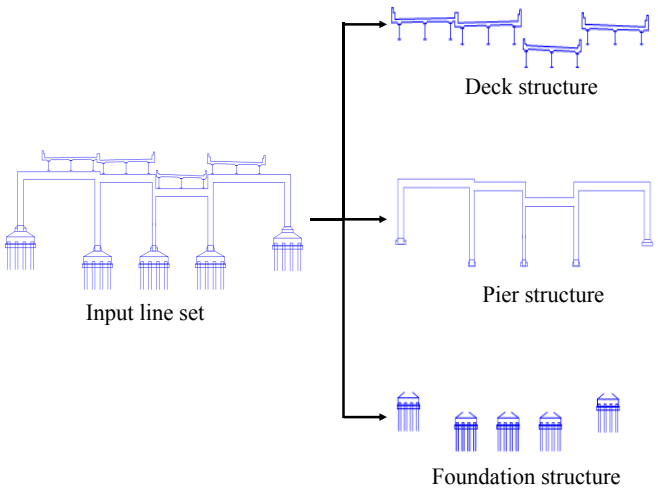

Figure e.8: Example for separation of geometric data by template matching method.

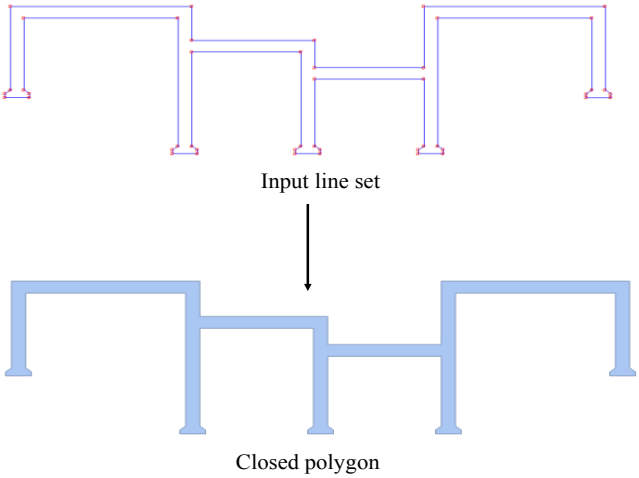

Figure e.9: Developed closed polygon for separated pier structure.

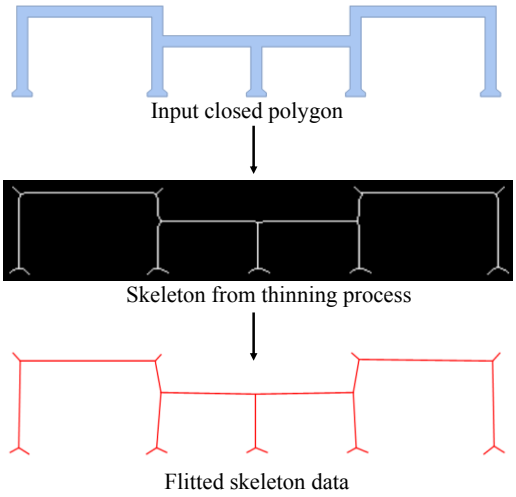

Figure e.10: Thinning process for frame model construction.

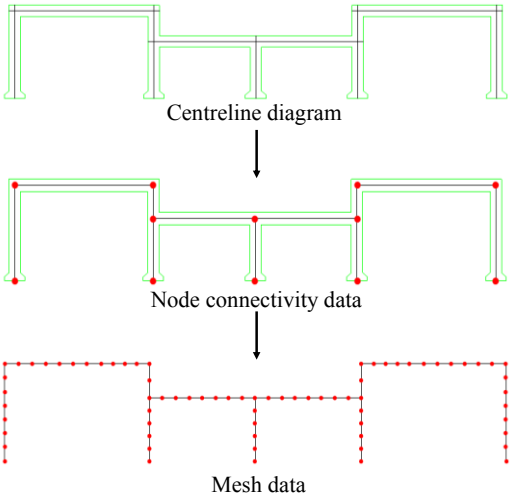

Figure e.11: Construction of node-connectivity data for frame model.

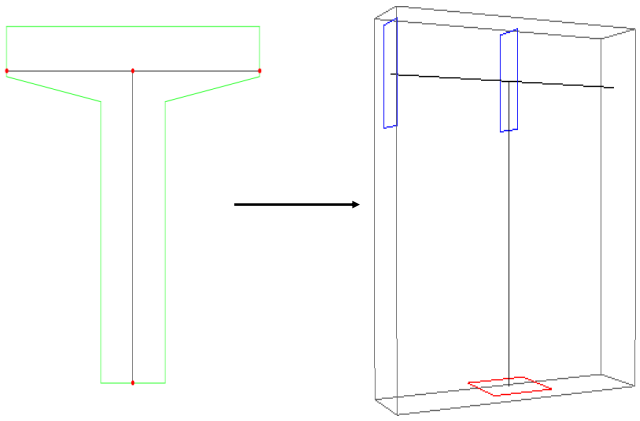

Figure e.12: Estimation of geometric data of cross-sections for pier structure.

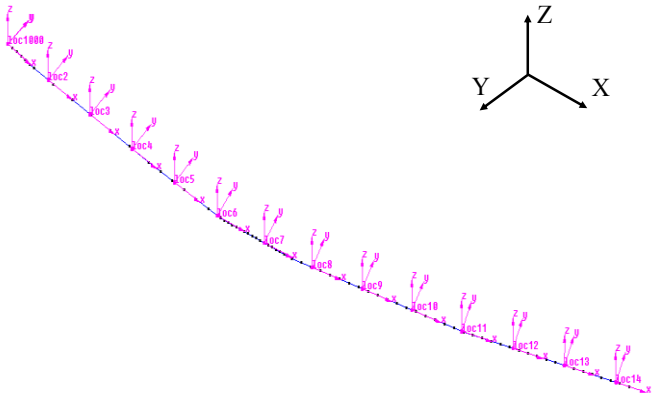

Figure e.13: Construction of freeway's centreline, pier locations and local axis for each pier location.

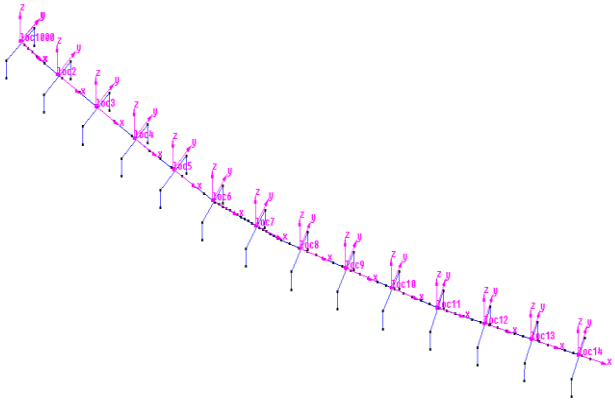

Figure e.14: Construction of frame model.

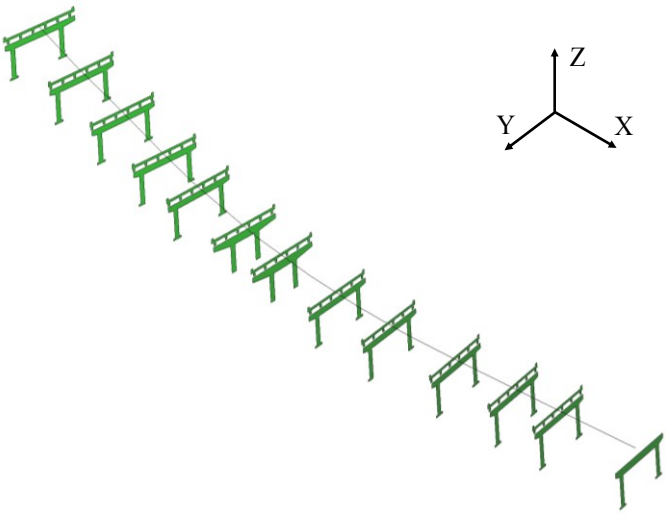

Figure e.15: Construction of NURBS surfaces for each pier and deck structure.

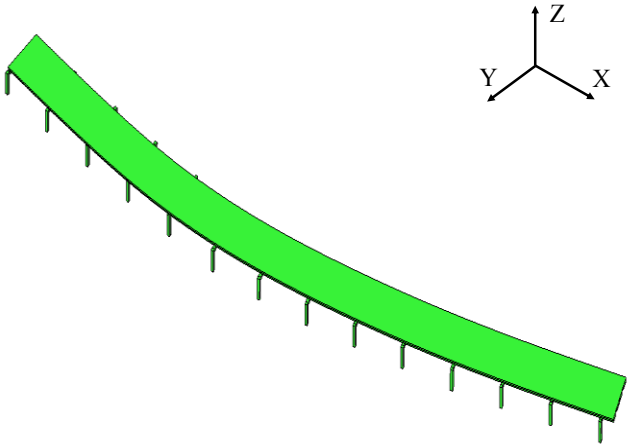

Figure e.16: Construction of volume for each member.